REPORT DOCUMENTATION PAGE	Form Approved OMB NO. 0704-0188

1. REPORT DATE (DD-MM-YYYY)	2. REPORT TYPE	3. DATES COVERED (From - To)
04-10-2009	Final Report	1-Apr-2005 - 30-Apr-2009

4. TITLE AND SUBTITLE	5a. CONTRACT NUMBER
Final Report	W911NF-05-1-0184
	5b. GRANT NUMBER
	5c. PROGRAM ELEMENT NUMBER
	611102

6. AUTHORS	5d. PROJECT NUMBER
Donna A. Chen	
	5e. TASK NUMBER
	5f. WORK UNIT NUMBER

7. PERFORMING ORGANIZATION NAMES AND ADDRESSES	8. PERFORMING ORGANIZATION REPORT NUMBER
University of South Carolina Office of Sponsored Programs & Research James F. Byrnes International Center Columbia, SC 29208 -	

9. SPONSORING/MONITORING AGENCY NAME(S) AND ADDRESS(ES)	10. SPONSOR/MONITOR'S ACRONYM(S)
U.S. Army Research Office P.O. Box 12211 Research Triangle Park, NC 27709-2211	ARO
	11. SPONSOR/MONITOR'S REPORT NUMBER(S)
	46269-CH.1

12. DISTRIBUTION AVAILIBILITY STATEMENT

Approved for public release; Distribution Unlimited

13. SUPPLEMENTARY NOTES

The views, opinions and/or findings contained in this report are those of the author(s) and should not contrued as an official Department of the Army position, policy or decision, unless so designated by other documentation.

14. ABSTRACT

Over the course of this grant, three main projects were conducted in to gain a better understanding of the decomposition of sulfur and phosphorus-based chemical warfare agents. The first project involved studies of the thermally-activated decomposition of dimethyl methylphosphonate (DMMP) on bimetallic Au-Pt clusters; one of the main problems with transition metal catalysts is that phosphorus is difficult to remove from the surface and poisons that catalyst for further reaction. Thus, the primary objective of this work was to understand whether the

15. SUBJECT TERMS

DMMP, organophosphorus agent, chemical warfare agent, decomposition, catalysis

16. SECURITY CLASSIFICATION OF:			17. LIMITATION OF ABSTRACT	15. NUMBER OF PAGES	19a. NAME OF RESPONSIBLE PERSON
a. REPORT	b. ABSTRACT	c. THIS PAGE	SAR		Donna Chen
U	U	U			19b. TELEPHONE NUMBER
					803-777-1050

Army Research Office Final Report
Grant W911NF-05-1-0184
"In Situ Studies of the Decomposition of Simulated Chemical Warfare Agents on Nanoparticle Catalysts"
PI: Donna A. Chen

Overview

Over the course of this grant, three main projects were conducted in to better understanding the decomposition of sulfur and phosphorus-based chemical warfare agents. The first project involved studies of the thermally-activated decomposition of dimethyl methylphosphonate (DMMP) on bimetallic Au-Pt clusters; one of the main problems with transition metal catalysts is that phosphorus is difficult to remove from the surface and poisons that catalyst for further reaction. Thus, the primary objective of this work was to understand whether the addition of a relatively unreactive metal like Au to a metal like Pt, which is active for DMMP decomposition, could enhance the ability to remove phosphorus from the surface. For the second project, the decomposition of methanethiol on Ni clusters as model systems for understanding destruction of sulfur-containing molecules as simulants for mustard gas. The third project deals with studies of DMMP decomposition on crystalline ceria thin films with various levels of reduction. The reaction mechanism for DMMP chemistry on ceria has been studied in detail. Although ceria retains activity for DMMP decompositon after multiple adsorption-reaction cycles, the surface is still poisoned by PO_x.

Decomposition of DMMP on Au-Pt Clusters
Characterization of Au-Pt Clusters
Scanning Tunneling Microscopy Studies

In order to understand the effects of Pt on the sintering of Au-Pt clusters, pure Au clusters on $TiO_2(110)$ were initially studied by STM after deposition at room temperature and subsequent annealing to various temperatures (Figures 1a-d). The deposition of 0.10 ML of Au results in average cluster sizes of 42 ± 7Å in diameter and 11 ± 2 Å in height. Although the apparent diameters are known to be overestimated due to tip convolution effects, these values are reported here because changes in the measured diameters still correspond to real differences in cluster size. The majority of Au clusters are located at step edges due to the high mobility of Au on the $TiO_2(110)$ surface. Apparently, Au atoms are not easily trapped at defects on the titania surface, such as oxygen vacancies, and are therefore able to reach the step edges, which are the most favorable binding sites for Au. After the surface is heated to 500 K, there is little difference in the average size of the Au clusters (data not shown). However, heating to 600 K produces larger clusters, and at 800 K, the continued growth of large clusters is observed as well as the appearance of small Au clusters less than 30 Å in diameter and 5 Å in height. At 1000 K, the average size of the large clusters increases to 69 ± 7 Å in diameter and 16 ± 2 Å in height while the smaller Au clusters remain. Notably, the onset of Au desorption from the TiO_2 surface occurs at ~900 K.

The STM images in Figure 2 correspond to Au-Pt bimetallic clusters with the same total metal coverage (0.10 ML) as for the pure Au images in Figure 1. The STM image for 0.024 ML of Pt deposited at room temperature (Figure 2a) shows that small Pt clusters (28 ± 3 Å in diameter, 5 ± 1 Å in height) are found on terraces with no preference for nucleation at step edges. This difference in nucleation behavior between Au and Pt can be explained by slower diffusion of Pt on the TiO_2 surface. When 0.074 ML of Au is deposited on the Pt clusters (Figure 2b), the cluster density does not increase, but the average cluster size increases to 41 Å in diameter and 8 Å in height, suggesting that Pt clusters act as seed nuclei for the incoming Au atoms to form bimetallic Au-Pt particles. This surface is referred to as Pt25%+Au since Pt deposition was followed by Au, with Pt accounting for 25% of the total metal coverage.

A recent theoretical study has reported that Pt binds more strongly to oxygen vacancy defects than Au, resulting in higher diffusion rates for Au on TiO_2.[1] Ab initio pseudopotential total energy calculations show that Pt binds more strongly to TiO_2 than Au by ~ 2 eV. Furthermore, oxygen vacancies act as nucleation sites for both metals, but the migration barrier for Pt leaving an oxygen vacancy is higher than that for Au. These results help explain the greater mobility of Au relative to Pt on vacuum-annealed TiO_2(110), which is known to have 7-10% oxygen vacancies.[2] Moreover, previous STM investigations of Au and Pt on TiO_2(110) have illustrated that Au clusters are preferentially located at steps[3-7] while Pt clusters tend to be smaller and are found on terraces with no preference for step edges.[8,9] The work reported here confirms the growth behavior observed in the earlier investigations and demonstrates that mobile Au atoms are able to migrate to the high coordination step sites; in contrast, the Pt atoms are more likely to be pinned at oxygen vacancy defects and consequently do not reach the steps. The preferential nucleation of Au at existing Pt clusters is attributed to the strong metal-metal bonding compared to metal-titania[10] and the high diffusion rate of Au on TiO_2. Au atoms are capable of diffusing to existing Pt clusters, where they become trapped through the formation of relatively strong metal-metal bonds.

When the Au-Pt clusters are annealed at elevated temperatures, the clusters exhibit less sintering than observed with pure Au (Figures 2c-e). Although annealing at 600 K and 800 K induces cluster growth, smaller clusters appear on the surface as well. At 1000 K, the average size of the larger clusters is clearly smaller than if they were pure Au (51±5 Å in diameter and 11±2 Å in height versus 69±7 Å and 16±2 Å, respectively).

Histograms of cluster heights for the pure Au and Au-Pt clusters both before and after annealing are shown in Figure 3. Cluster heights are used as a measure of overall cluster size since the values for the diameter are known to be overestimated in the STM images. All histograms represent measurements from 80 clusters, except for the experiment involving Au annealed at 1000 K, in which only 52 clusters were imaged. At room temperature, the 0.10 ML Au clusters range from ~5-15 Å in height with the maximum in the distribution centered at 10 Å. When Au clusters are annealed at 1000 K, a bimodal distribution is formed, with smaller clusters around 3 Å and larger clusters around 15 Å in height. The 0.024 ML of Pt clusters exhibit smaller sizes than the Au clusters at room temperature, and this is consistent with the lower mobility of Pt as well as the lower Pt coverage. The Pt height distribution is centered around 2.5 Å, whereas there are few pure Au clusters below 5 Å in height. Subsequent deposition of 0.072 ML of Au on the 0.024 ML Pt clusters (Pt25%+Au) causes the center of the height distribution to shift toward larger values (~7 Å), as expected for nucleation of Au on the Pt seed clusters. Finally, annealing the Au-Pt clusters at 1000 K produces a bimodal distribution as in the case of pure Au. However, height distributions of the small and large clusters are much closer together for Au-Pt than for pure Au. The large Au-Pt clusters have heights centered around 11 Å and are considerably smaller than the large Au clusters, but the height distributions for the small clusters are comparable for Au-Pt and Au. The presence of small clusters <5 Å in height can be explained by the trapping of metal atoms at defects like oxygen vacancies; small clusters of only a few atoms may be strongly bound to oxygen vacancies, preventing surface diffusion and participation in the sintering process.

When the order of deposition is reversed, and 0.024 ML of Pt is deposited onto 0.072 ML of Au (Au+Pt25%), bimetallic clusters are not formed at room temperature. The STM images in Figure 4 show that relatively large clusters of pure Au are preferentially nucleated at the step edges for the initial 0.072 ML Au deposition. Subsequent deposition of Pt gives rise to the

coexistence of larger Au clusters at step edges (42 Å in diameter, 11 Å high) and smaller Pt clusters that nucleate on the terraces (28 Å in diameter, 5 Å high). There is no evidence for the formation of bimetallic Au-Pt clusters until after the surface is annealed. After annealing at 600 K and 800 K, larger clusters are formed, and at 1000 K, the average size of the large clusters is 50±6 Å in diameter and 11±2 Å in height. This is very similar to the average size of the annealed Au-Pt clusters produced from the reverse order of deposition, suggesting that the mixing of Au and Pt occurs upon annealing at 1000 K. The Au+Pt25% surface also exhibits a bimodal cluster size distribution after annealing, similar to pure Au and Pt25%+Au.

In order to understand how the Pt composition affects sintering in the bimetallic Au-Pt clusters, Au was nucleated at Pt clusters with compositions corresponding to 10% and 50% Pt at a total metal coverage of 0.10 ML. The plot in Figure 5 represents the average cluster height of the large particles in the bimodal distribution after annealing at 1000 K as a function of Pt composition. The average cluster height from the STM images is used as a measure of cluster sintering, with smaller clusters indicating a lower rate of sintering; at least 15 clusters were measured for each Pt composition. Between 10% and 50% Pt, the average height decreases almost linearly with increasing Pt composition, but between 0 and 10% there is a more precipitous drop in cluster height.

The decrease in rate of sintering with increasing Pt content can be explained in terms of metal-metal bond strengths. For many metal clusters on TiO_2, such as Cu, Ni, and Rh, STM experiments have shown that the rate-limiting step in the sintering process is the detachment of atoms from existing clusters, rather than diffusion on the surface.[11,12] Therefore, the rate of sintering should scale with the metal-metal bond strengths. Since Au-Au bonds (2.04 eV) are much weaker than Pt-Pt bonds (3.29 eV),[1] it is not surprising that pure Pt clusters sinter less readily than pure Au. The presence of Au-Pt or Pt-Pt bonds at the perimeter of the bimetallic clusters should suppress cluster sintering, given that the Au-Pt bond strength (2.30 eV) is still higher than that for Au-Au.[1] The values cited here for metal-metal bond strengths are from the theoretical studies by Iddir *et al.* Although experimental values are not known for Au-Pt bond strengths, Au-Au and Pt-Pt bond strengths calculated in this study[1] agree with experimental data for the relative bond strengths, based on heats of sublimation for the pure metals.

Plots of cluster density vs. annealing temperature for the Au on Pt surfaces with varying compositions confirm that Au nucleates at Pt seed clusters (Figure 6). The addition of Au to predeposited Pt clusters does *not* cause a significant increase in cluster density, which is consistent with Au nucleation at existing Pt clusters. For example, in Figure 6a, the total cluster density in the Pt25%+Au experiment actually decreases slightly when Au is added, and the same holds true for the Pt50%+Au experiment. This behavior is attributed to cluster coalescence that occurs when a growing Au-Pt cluster merges with its neighbor; coalescence is most often observed when the initial cluster density is high, and Pt seed clusters are nucleated in close proximity to each other. However, there is a very small increase in the number of clusters after Au deposition when Au is deposited on a low coverage of Pt clusters, as in the case of 0.01 ML of Pt followed by 0.09 ML of Au (Pt10%+Au). Since there are not many Pt seed clusters on the surface at this coverage, it is possible for a small fraction of Au atoms to form pure Au clusters at step edges rather than nucleating at existing Pt clusters.

As the surfaces are annealed at 600 K and 800 K, there is little change in the total cluster densities for any of the Au-Pt compositions even though significant cluster growth is observed in STM images, particularly at 800 K. The nearly constant cluster densities up to 800 K can be explained by examining the trends in the densities of the small (<5 Å in height) and large clusters

in the bimodal distribution that develop after annealing (Figure 6b,c). During the sintering process, the growth of some clusters is offset by the disappearance of others, and this behavior is reflected in the decrease in cluster densities of the large particles, which constitute the majority of clusters on the surface at room temperature. However, the reduction in number of large clusters is offset by an increase in the number of small clusters upon annealing so that the total number of clusters is almost unchanged. Above 900 K, the decrease in cluster densities is partially attributed to the desorption of Au from the surface. It is also likely that small Au clusters gain sufficient energy to escape from surface defects, contributing to the disappearance of the small clusters at temperatures between 800 and 1000 K.

Low Energy Ion Scattering Studies
<u>Surface Composition</u>

LEIS experiments were carried out to determine the composition of the first monolayer on the cluster surfaces. Unfortunately, the similar masses of Pt and Au result in only a small energy separation between the Pt and Au peaks in the LEIS spectra, but the relative contributions of Pt and Au to the overall signal can still be determined from peak fitting. The LEIS peak for 0.10 ML of pure Au appeared at 534 eV and was used to fit the Au contribution in the spectra of the Au-Pt clusters. In the case of Pt, the peak energies corresponding to pure Pt clusters exhibited a slight shift with coverage, and therefore the Au-Pt spectra were fit with Pt peak shapes corresponding to the appropriate Pt coverage for the bimetallic clusters. Peak fitting was carried out manually by subtracting a scaled contribution of the Au peak from the Au-Pt spectrum and fitting the resulting spectrum with a scaled contribution from the Pt peak. The sensitivity factors for Au and Pt were determined by depositing 0.3 ML of the pure metals on TiO_2, integrating the resulting LEIS peaks, and then correcting for the relative surface areas of the clusters, which were estimated from a numerical integration of the STM images.[13]

The spectra for 0.074 ML of Au deposited on 0.024 ML of Pt (Pt25%+Au) and annealed at various temperatures are shown in Figure 7a. For the pure 0.024 ML Pt seed clusters, the Pt peak appears at 531 eV. Subsequent deposition of Au results in a spectrum that is fit with Pt and Au features corresponding to a surface composition of 61% Au, which is slightly lower than the overall composition of 75% determined by the relative coverages of deposited Au and Pt . At 600 K, 800 K and 1000 K, the surface Au composition increases to ~70%, and changes in surface composition with temperature are summarized in Figure 8. There is a substantial decrease in total metal signal at 1000 K compared to room temperature, most likely due to a combination of Pt encapsulation by titania and Au desorption.

For comparison, surface compositions were investigated for 0.074 ML of Au on 0.024 ML of Pt (Au+Pt25%), which consisted of discrete clusters of Au and Pt rather than bimetallic Au-Pt particles (Figure 7b). At room temperature, the Au atoms accounted for 55% of the total surface area of the clusters. Given that the overall Au composition is 75%, the lower surface composition is attributed to the fact that the Au clusters are larger than the Pt clusters, and therefore the ratio of surface atoms/total atoms is lower for the Au clusters. After annealing at 600 K, 800 K and 1000 K, the surface composition of Au remains 55-60% (Figure 8). Despite that fact that pure metal clusters are believed to coalesce into bimetallic Au-Pt clusters after annealing, the surface composition is not significantly altered. Furthermore, the deposition of Au on Pt leads to surface compositions that are similar to the reverse order of deposition at all temperatures although the Pt on Au surfaces are always 5-10% richer in Au.

Surface compositions were also studied for Au deposited on existing Pt clusters with varying Pt coverages to produce Au-Pt bimetallic clusters with different overall compositions, at the same total coverage of 0.10 ML. From peak fitting of the LEIS spectra at room temperature (data not shown), overall compositions of 25% and 50% Au produce surface compositions of 25% and 41%, respectively. Thus, the surface compositions of the bimetallic Au-Pt clusters are close to the overall compositions, but for higher Au content, the clusters tend to be less rich in Au at the surface.

It is surprising that the surface compositions of the Au-Pt clusters are not 100% Au and instead contain a significant fraction of Pt. Based on the lower surface free energy of Au compared to Pt (1.1 J/m^2 [14,15] vs. 2.5 J/m^2 [16]) the bimetallic clusters were expected to form a core shell structure, in which Au completely covers a Pt core. Atom probe field ion microscopy studies of a bulk Au-Pt alloy containing only 4% Au have also reported that the first surface monolayer is 99% Au; although surface enrichment of Au is observed for the first 4 layers, the Au composition decreases with each layer deeper into the bulk.[17] Furthermore, Au and Pt are not miscible in the bulk at Pt concentrations higher than ~15%,[18] and therefore when Au is deposited on top of Pt clusters, no mixing of Au and Pt is anticipated.

Despite the immiscibility of Au and Pt in the bulk, there are other examples in the literature of bimetallic Au-Pt clusters, in which the Pt and Au atoms are mixed. In a very recent study by Bus *et al.,* Au-Pt clusters on SiO$_2$ and TiO$_2$ were prepared by wet impregnation using Pt$_2$Au$_4$(C≡CBu^t)$_8$ as the metal precursor.[19] In both cases, mixing of Au and Pt within the clusters was observed by Extended X-ray Absorption Fine Structure (EXAFS). The smaller 1.5 nm Au-Pt clusters on SiO$_2$ were well mixed, and the surface was enriched in Au, which is expected if the surface has the same 1:2 Pt:Au ratio as the bulk. The larger 2-3 nm Au-Pt clusters on TiO$_2$ were not completely mixed. This result is consistent with our LEIS experiments that demonstrate that for larger clusters prepared by depositing 0.375 ML of Au on 0.125 ML of Pt (Pt25%+Au), the cluster surface is pure Au,[20] in contrast to the lower coverage experiments in which the surface and overall compositions are roughly the same. Lang *et al.* also synthesized Au-Pt clusters on SiO$_2$ from K$_2$PtCl$_4$ and HAuCl$_4$ salts that were stabilized in polyamidoamine dendrimers before reduction with hydrogen to form the metallic particles.[21] For Au$_{16}$Pt$_{16}$ particles, the Pt and Au atoms were believed to be intimately mixed based on infrared studies of CO adsorption; these experiments demonstrated that the C-O stretching frequency was red shifted by 20 cm^{-1} for CO on Pt in Au-Pt particles compared to the frequency observed on pure Pt particles, indicating that Pt atoms were surrounded by Au. In addition, there was evidence that adsorption of CO caused Pt diffusion to the cluster surface due to the strong Pt-CO bonding, suggesting that Pt atoms are mobile within the clusters between room temperature and 413 K. In another study, Au-Pt particles were prepared from water-in-microemulsions, and alloying was confirmed by X-ray diffraction experiments.[22] Furthermore, X-ray diffraction studies showed that alloyed Au-Pt particles were produced by a two-phase synthesis method involving AuCl$_4^-$ and PtCl$_6^{-2}$ and an organic capping agent, followed by reduction with NaBH$_4$.[23]

The enhanced mobility of atoms within nanosized bimetallic clusters has also been observed in other systems. For Pt-Rh clusters on TiO$_2$(110), mixing of Pt and Rh within clusters occured at room temperature even though there was insufficient energy for interdiffusion of Rh into bulk Pt surfaces.[9,24,25] In addition, Monte Carlo simulations of a 1000-atom Au(50%)-Pt(50%) clusters on graphite illustrated that Au and Pt atoms mix at room temperature. However, this mixing was not perfect on the atomic level, and small islands of pure metal were formed in each cluster layer.[26]

Similarly, the mobility of atoms within nanoclusters have been reported to be higher than within bulk metals; the nanoclusters have a large fraction of total atoms at the surface, where their coordination numbers and binding energies are lower than in the bulk. It is well established from both experimental and theoretical work that metal nanoclusters melt at lower temperatures than the bulk materials, and the melting temperature decreases with diminishing cluster size.[27-32] For example, scanning electron diffraction experiments on Au clusters 20-50 Å in size showed that melting temperatures can be as much as 300 K lower for the nanoclusters than for the bulk.[30] For 8 nm Pt clusters, TEM studies demonstrated significant diffusion and restructuring of facets at 770 K even though the melting temperature of bulk Pt is 2040 K.[33] Molecular dynamics simulations for Au clusters of different sizes reported that the melting temperature decreases with decreasing cluster size, and clusters of 146 and 459 atoms had melting temperatures of 625 K and 760 K, respectively, compared to 1090 K for the bulk.[34] Another molecular dynamics study of Ni particles of less than 500 atoms exhibited cluster-molecular behavior that was different from bulk melting; specifically, the melting temperature of Ni clusters was 980 K compared to 1760 K for the bulk.[35] Since the Au-Pt clusters studied here range from 100 atoms at room temperature to 200 atoms at 1000 K for the Pt25%+Au surface, it is not surprising that the Au-Pt clusters exhibit melting behavior different from the bulk.[36]

Encapsulation

Plots of the LEIS signal contribution from Pt as a function of annealing temperature demonstrate that encapsulation by titania is inhibited by the presence of Au at the cluster surfaces (Figure 9a). Pt signals are normalized against the largest value, which occurs at room temperature for all surfaces. For the 0.10 ML pure Pt clusters heated to 600 K, the Pt LEIS signal drops to ~40% of the value at room temperature, indicating that extensive encapsulation occurs at this temperature. The Pt signal continues to decrease after further heating, reaching 10% and 4% of the room temperature value at 800 and 1000 K, respectively. Since Pt does not desorb from the surface at 1000 K, any loss in Pt signal is attributed solely to encapsulation by titania or sintering. Given that previous studies of the sintering of Pt clusters on $TiO_2(110)$ show that there is much less cluster growth upon annealing for Pt compared to other metals like Ni, Rh and Cu,[9] there should not be substantial loss of signal from sintering. For the bimetallic clusters prepared by nucleating Au at Pt clusters, the decrease in Pt LEIS signal is lower at all temperatures for the clusters with higher Au content. For instance, after heating to 1000 K, the Pt25%+Au clusters have lost 62% of the Pt signal at room temperature compared to 80% for the Pt50%+Au clusters and 96% for the pure Pt clusters.

Changes in the Au signal as a function of annealing temperature for pure Au clusters and Au-Pt clusters are shown in Figure 9b. In each temperature series, Au signals are normalized against the highest value, which is the signal at room temperature for the pure Au clusters and at 600 K for the Au-Pt clusters. In the case of 0.10 ML Au clusters, there is a 24% decrease in signal area due to loss of surface area from sintering between room temperature and 800 K, but at 1000 K, the 90% drop in signal compared to the clusters at room temperature is attributed to both sintering and Au desorption. Notably, the decrease in Au signal cannot be to ascribed to encapsulation, which does not occur for Au clusters on titania. The Au-Pt clusters were prepared by deposition of Au on Pt, and for both the Pt25%+Au and Pt50%+Au clusters, annealing at 600 K causes a 30-40% *increase* in Au signal. Since the signal from the pure Au clusters decreases at 600 K, the rise in Au signal for Au-Pt is explained by diffusion of Au to the cluster surface. Both Au-Pt surfaces at room temperature are slightly deficient in Au compared to the overall

composition, and annealing at 600 K brings the surface composition closer to the overall: the Pt25%+Au clusters are 70% Au, while the Pt50%+Au clusters are 55% Au. For both the Au-Pt cluster compositions annealed at 800 K, the Au signal is reduced to ~75% of the value at 600 K, and this is similar to the intensity initially observed at room temperature. At 1000 K, the normalized signal intensity is lowest for the pure Au. Given that the reduction in Au signal is attributed to either Au sintering or Au desorption, the clusters containing Pt should exhibit a smaller loss of Au signal since Au-Pt bonds are stronger than Au-Au. Likewise, it would also be expected that the decrease in Au signal is greater at 1000 K for the 25%Pt+Au clusters compared to the 50%Pt+Au, but the reduction in Au signal is nearly identical for these two Au-Pt surfaces. However, this result is considered to be within experimental error, which was determined by calculating standard deviation from multiple experiments. Error was the greatest for the Au signals at 1000 K (15-20%) because the desorption of Au occurs around 900 K, and consequently small differences in annealing time or the temperature ramp could result in a significant change in the amount of Au left on the surface. At all of the other temperatures and for the Pt signal at 1000 K, the error in the normalized LEIS signals was 3-12%.

Given that Pt exists at the surface of the Au-Pt clusters, it is not surprising that cluster encapsulation by reduced titania occurs after annealing, as in the case of pure Pt clusters. The driving force for this strong metal support interaction (SMSI) effect is the lower surface free energy of titania (0.3-0.7 J/m^2 [37,38]) compared to Pt (2.5 J/m^2 [16]). Although Au (1.1J/m^2 [14,15]) also has a higher surface free energy than titania, the inertness of Au and its inability to reduce TiO_2 preclude SMSI effects for Au clusters on TiO_2(110).[39] The extent to which Pt is covered by titania decreases with increasing Au content in the bimetallic clusters, and this suggests that the presence of Au at the surface inhibits migration of titania onto Pt at the cluster surface. Furthermore, there is no evidence that titania covers Au atoms at the cluster surface since changes in the Au LEIS signal with heating follow what is observed for pure Au clusters. It is therefore possible to control the degree of encapsulation of the Au-Pt clusters by changing the Au composition at the surface, with higher Au content resulting in less extensive encapsulation of Pt.

X-ray Photoelectron Spectroscopy Studies

The extent of reduction in the encapsulating layer of titania was investigated by XPS for the Au-Pt clusters and compared with SMSI for pure Pt on TiO_2, which is a system that has been well-studied.[40-42] To enhance surface sensitivity, grazing angle experiments were carried out with a 70° angle between the surface normal and the detector. Figure 10 shows the Ti(2p) region for 0.024 ML of Pt+0.074 ML Au (Pt+Au25%) deposited at room temperature and then heated to 600 K and 800 K for one minute. The data at room temperature exhibits an identical peak shape to the Ti(2p) spectrum collected without any metal on the surface, indicating that no additional reduction of the TiO_2 surface is induced by Au or Pt at room temperature. Annealing at 600 K causes a small increase in the signal intensity at 456.8 eV, which is attributed to a mixture of Ti^{+2} and Ti^{+3},[9,43] and there is no further change in the spectrum after heating to 800 K.

For comparison, data was collected for 0.024 ML of pure Pt clusters, which are known to be encapsulated by reduced titania with Ti^{+2} and Ti^{+3} oxidation states.[9,40,42] In the case of pure Pt clusters, the Ti(2p) spectra look identical to those of the Au-Pt clusters; there is a slight increase in the low binding energy shoulder at 600 K and no addtional change at 800 K. Thus, the relatively minor increase in the Ti(2p) low binding energy shoulder for the annealed Au-Pt clusters is attributed to the small total surface area for Pt at these low metal coverages, rather

than the inability of Au-Pt to reduce titania. Even at grazing angle detection, most of the signal is still from the TiO_2 substrate rather than the encapsulating layer. The Au-Pt clusters reduce titania to the same extent as pure Pt clusters, and this is consistent with idea that the Au-Pt clusters have surface Pt that becomes encapsulated by titania upon heating.

Summary

STM experiments show that bimetallic Au-Pt clusters are grown by depositing Au on existing Pt clusters since the mobile Au atoms will nucleate exclusively at these Pt seed clusters. In contrast, the deposition of Au followed by Pt leads to pure clusters of Pt and Au instead of nucleation of Pt at Au seed clusters. The rate of sintering for the clusters decreases with increasing Pt composition due to the formation of stronger Pt-Pt and Au-Pt bonds compared to Au-Au. The surface and overall compositions of the Au-Pt clusters are roughly the same, demonstrating that Au and Pt atoms can intermix at room temperature. These results are contrary to predictions from bulk thermodynamics, which suggest that the cluster surfaces should be almost pure Au. For the Au-Pt clusters, the extent of encapsulation from SMSI effects is controlled by the Pt composition; reduced titania covers the Pt regions at the cluster surface, but the presence of Au inhibits migration of titania onto the surface of the clusters.
Au50

DMMP decomposition on TiO_2

In order to understand chemistry on the TiO_2-supported clusters, TPD studies of DMMP reaction were conducted on $TiO_2(110)$ itself (Figure 11), and these results were in agreement with previous studies of DMMP on titania.[13,44] The main gaseous product is methyl radical (15 amu), which desorbs in a peak at 650 K, and the 15 amu signal shown in Figure 11 was corrected for the cracking contribution from methane and DMMP. Other gaseous products are H_2 (2 amu) evolved in a broad peak over the 400-750 K temperature range, and methane (16 amu) with a desorption peak at ~630 K. Trace amounts of methanol (31, 32 amu) are detected in a broad peak extending between 400 and 650 K. Molecular DMMP (94 amu) desorption is observed in a peak centered at 440 K; although the parent mass of DMMP is 124 amu, 94 amu was chosen to represent DMMP desorption because of its higher intensity. No masses were detected below 800 K other than those corresponding to fragmentation of the reported products. Specifically, H_2O, CO, CO_2 and any phosphorus-containing species other than DMMP were not observed.

The ability of the titania surface to sustain activity over multiple cycles of adsorption and reaction was evaluated by running five successive TPD experiments on the same surface (Figure 12). For each cycle, DMMP was adsorbed at room temperature followed by heating to 800 K in front of the mass spectrometer, and the product yields were determined from the integrated peak areas of the masses in the TPD spectra. Both methyl and methane yields drop significantly after the first adsorption-reaction cycle, presumably due to poisoning of the active sites by the byproducts of DMMP decomposition. Between the second and fifth cycles, the reduction in product yields is more gradual. While the methane production reaches zero for the fifth cycle, the methyl yield decreases more gradually and is still 16% of the initial yield after the fifth cycle, indicating that the titania surface has sustained activity for the decomposition of DMMP to methyl. As expected the desorption of unreacted DMMP increases over the five reaction cycles due to the decrease in activity for DMMP decomposition after successive adsorption and reaction.

Heating TiO_2 in UHV to 965 K restores activity for methyl and H_2 production from DMMP decomposition to the level of the clean TiO_2 surface although the methane yield decreases by 28% compared to the clean surface values. A small 31 amu peak from the desorption of phosphorus is detected at ~960 K in TPD experiments in which the temperature was increased to 1000 K; however, 47 and 79 amu signal from a PO_x species or 33 and 34 amu signal from PH_x are not observed. A small amount of phosphorus is still detected by AES: the P(LVV) signal decreases by 80% between TPD to 800 K and further heating to 965 K. Carbon is also removed from the TiO_2 surface, as demonstrated by the appearance of small CO_2 (44 amu) and methyl (15 amu) peaks at ~950 K.

Oxidation of TiO_2 at 700 K and under a flow of O_2 for 1 hour ($2.7x10^{12}$ L) results in the complete disappearance of the P(2p) signal. Under milder oxidation conditions in UHV ($1x10^{-7}$ Torr, 5 min), phosphorus removal does not occur below 700 K. After oxidation at 800 K in UHV, the phosphorus Auger signal decreases by 90%. DMMP decomposition on this surface results in methyl production identical to that on the clean TiO_2 surface, while methane and H_2 yields are 64% and 39%, respectively, of the clean surface values. The C(1s) XPS signal is also reduced to a level barely above the noise following oxidation at 800 K and $1x10^{-7}$ Torr, indicating that carbon is removed from the surface by oxidation.

DMMP decomposition on Pt, Au and Au-Pt clusters on TiO_2

Scanning tunneling microscopy studies

The morphologies of the metal clusters deposited at room temperature on $TiO_2(110)$ were characterized by scanning tunneling microscopy, as shown in Figure 13. For the same coverage of 0.5 ML, the Pt surface (Figure 13a) exhibits smaller average cluster sizes and higher cluster densities compared to the Au surface (Figure 13b). This behavior is consistent with what has been previously observed for the growth of Pt and Au clusters at lower coverages [45] and is also consistent with the lower mobility of Pt atoms on the $TiO_2(110)$ surface compared to Au.[1] Based on measurements for a set of 20 clusters, the average height and diameter of the Pt clusters were 8.5 Å$\pm$2.6 Å and 41.8 $\pm$8.0 Å, respectively, compared to values of 14.9$\pm$4.0 Å and 68.6$\pm$12.4 Å for the Au clusters. Note that the average diameters reported here are measured directly from the STM line profiles, but the true cluster diameters are believed to be a factor of √5 smaller due to tip convolution effects.[45] The factor of √5 is derived from a comparison of coverages calculated from the average sizes of the clusters from the STM line profiles[46,47] with coverages measured by an independently calibrated quartz crystal microbalance.[45] Therefore, the true average diameters are estimated to be 18.7 Å and 30.7 Å for the 0.5 ML Pt and Au clusters, respectively. Cluster densities determined from the 1000Å×1000Å images were $1.12x10^{13}$ clusters/cm^2 for Pt and $5.19x10^{12}$ clusters/cm^2 for Au. The bimetallic surface in Figure 13c, which was prepared by deposition of 0.25 ML of Pt followed by 0.25 ML of Au (Pt+Au), exhibited cluster sizes that were intermediate between that of pure Pt and pure Au, with an average height of 13.6$\pm$3.0 Å, measured diameter of 55.6$\pm$7.7 Å (actual diameter 24.9 Å) and density of $7.61x10^{12}$ clusters/cm^2.

Pt Clusters

TPD experiments for DMMP on the 0.5 ML Pt clusters on $TiO_2(110)$ show that CO (28 amu) and H_2 (2 amu) are the major reaction products (Figure 14). The H_2 desorbs in two peaks at 365 K and 550 K. The rising baseline above 900 K is attributed to desorption from the sample holder or mass spectrometer shield; the increase in baseline intensity is also observed for the typical background masses 2, 18, 28, and 44 amu when heating the crystal in the absence of DMMP.

The desorption of CO occurs in a lower temperature peak at 530 K and a more intense, higher temperature feature at 1030 K. The lower temperature peak is coincident with the second H_2 desorption state and is attributed to decomposition of DMMP to produce both gaseous CO and H_2. Furthermore, the appearance of the second H_2 desorption state at 550 K indicates that not all C-H bonds are broken at 365 K. The second CO peak is assigned to recombination of atomic carbon on the Pt clusters with oxygen from the TiO_2 lattice. An isotopic labeling experiment was conducted in which the TiO_2 surface was oxidized at 500 K and 1×10^{-7} Torr with $^{18}O_2$ for 30 minutes prior to deposition of Pt and exposure to DMMP. The production of $C^{18}O$ (30 amu) at 1030 K is consistent with the oxidation of atomic carbon by lattice oxygen that has been previously reported for carbon on $TiO_2(110)$-supported Ni clusters.[13,48] Surprisingly, $C^{18}O$ was also observed at 530 K, suggesting that C-O bond scission is reversible.

Methane (16 amu) and methyl (15 amu) are detected as minor desorption products from DMMP decomposition on the 0.5 ML Pt clusters (Figure 14). Since the 660 K peak temperature for methyl desorption is identical to that on the clean TiO_2 surface, this demonstrates that methyl is formed from reaction on exposed titania rather than on the Pt surfaces. In contrast, methane desorption has a different peak shape from that on the clean TiO_2 surface, suggesting that methane production occurs at Pt sites; the onset of methane desorption is at 300 K on the Pt clusters compared to 400 K on titania. The desorption of molecular DMMP (94 amu) is also observed in a peak at 420 K. The CO and H_2 peaks increase in intensity as the Pt coverage is increased up to 2 ML, confirming that these products are from reaction on Pt. Likewise, the decrease in methyl and methane yields with Pt coverage support reaction on TiO_2.

The ability of the Pt clusters to sustain activity for DMMP reaction was evaluated by conducting five successive TPD experiments on the 0.5 ML Pt clusters (Figure 15). Hydrogen and CO are the two products characteristic of DMMP reaction on Pt, and the yields for both of these products drop to zero after the first cycle, indicating total loss of activity. The methane yield is also significantly reduced after the first cycle but does not decrease to zero even after five cycles. Methane production drops off more sharply on the 0.5 ML Pt clusters compared to the TiO_2 surface although in both cases, the yield is near zero after the first cycle. The methyl yield is initially low on the Pt clusters and decreases slightly with increasing adsorption-reaction cycles without reaching zero. As expected, the yield for molecular DMMP desorption increases with the number of adsorption-reaction cycles since the loss of active sites for DMMP decomposition results in greater desorption of unreacted DMMP.

XPS data was collected for the P(2p) and C(1s) regions after exposing the 0.5 ML Pt clusters to DMMP at room temperature and heating to various temperatures (Figure 16). At room temperature, the P(2p) centered at 134.8 eV is consistent with the presence of molecular DMMP on the surface.[13,44,49] After heating to 400 K, the P(2p) shifts to 134.0 eV. This implies that P-C bonds are broken at this temperature and is in agreement with the desorption of H_2 and methane observed at 400 K in the TPD experiments. Some P-O bonds must remain intact since the 134.0 eV binding energy is in the range for a PO_x species.[13,44] The decrease in P(2p) intensity is also in agreement with molecular DMMP desorption at 400 K. Between 400 K and 600 K, there is little change in the P(2p) spectrum, but at 800 K, a lower binding energy phosphorus peak appears at 129.5 eV and is attributed to atomic phosphorus on Pt, based on the 128.5-129 eV binding energies observed for phosphorus on other transition metals like Rh [50,51] and Cu.[52] After heating to 1000 K, the 134.0 eV species disappears, indicating that all P-O bonds are broken. The decrease in total P(2p) signal intensity suggests that phosphorus migrates into the Pt surface since no phosphorus-containing products are observed in the TPD experiments.

At room temperature, the C(1s) region exhibits a broad peak centered around 287.3 eV (Figure 16b). Based on previous studies of DMMP on titania surfaces as well as Cu and Ni clusters, this spectrum is characteristic of molecular DMMP on the surface. The spectrum can be fit with peaks at 286.3 eV and 287.8 eV attributed to the methyl and methoxy carbons,[13,44] respectively, in molecular DMMP, as well as a contribution at 284.6 eV assigned to a CH_x intermediate.[53,54] The fact that the 286.3 eV and 287.8 eV peaks have an area ratio closer to 1:1: rather than the 1:2 ratio expected for intact DMMP implies that $P-OCH_3$ bond scission occurs at room temperature. The same behavior was observed for DMMP on Ni clusters at room temperature while the ratio was closer to 2:1 on the less active supported Cu clusters and approximately 2:1 on $TiO_2(110)$ itself.[13,44,49] After heating to 400 K, the lower binding energy contribution from the decomposition species increases at the expense of the higher binding energy peaks, indicating additional C-P bond scission. At 500 K, the contribution of the higher binding energy species continues to decrease, and the overall reduction in carbon signal is consistent with the production of gaseous CO at this temperature. Between 500 K and 600 K, the contribution of 286.3 eV and 287.8 eV peaks is further reduced, and there is little additional change in the spectra after heating to 800 K. At this temperature, the carbon peak is centered at 284.5 eV, which is a binding energy that is too high for atomic carbon on Pt,[54] and is more consistent with CH_x on Pt[54] or titania.[49,53] After heating to 1000 K, almost all of the carbon signal disappears, which confirms the removal of surface carbon via oxidation with lattice oxygen to produce gaseous CO, as observed in the TPD experiments.

Although the phosphorus signal is reduced almost to zero by heating to 1000 K, significant changes in the surface morphology occur under these conditions. It has been well-established that Pt clusters undergo strong metal support interactions upon heating the clusters on titania, resulting in encapsulation of the Pt clusters by reduced titania.[9,40-42] Low energy ion scattering signals for the 0.5 ML Pt clusters as a function of heating to 1000 K are shown in Figure 17, where the Pt signal has been normalized to the highest value at room temperature. Below 600 K, the loss in Pt signal is less than 10%, but after heating to 800 K, 82% of the signal is lost. The Pt signal at 1000 K is less than 4% of the room temperature value, indicating almost complete encapsulation of the Pt clusters by titania. The Pt LEIS signal is also shown for the 0.5 ML clusters exposed to DMMP at room temperature and heated to 600 K, 800 K and 1000 K. Below 600 K, the presence of molecular DMMP on the surface reduces the Pt signal almost to zero, and even at 600 K, the intensity is only 23% of the room temperature Pt signal in the absence of DMMP. Additional heating of this surface to 800 K decreases the Pt signal by only 5%, and the absolute signal at 1000 K for DMMP on Pt is actually larger than for pure Pt in the absence of DMMP decomposition. Therefore, the DMMP decomposition species on the Pt surface such as phosphorus and carbon could inhibit the migration of titania onto the surface of the Pt clusters and prevent complete encapsulation.

Oxidation of the Pt clusters at 600 K (1×10^{-7} Torr, 5 min) after DMMP decomposition causes the intensity of the P(2p) peak to diminish to a level just above the noise (Figure 16a), but the Pt(4f) signal also decreases by 84%, suggesting that oxidation promotes the growth of titania over the Pt clusters. For Ni[55] and Pd[56,57] clusters on $TiO_2(110)$, dissociation of O_2 on the metal surfaces has been shown to promote the growth of titania over the metal clusters. There is evidence for phosphorus diffusion in and out of the bulk upon heating the Pt clusters since the P/Pt Auger ratios increase and then decrease during annealing at 700 K in O_2. Similar changes in the surface phosphorus concentration with annealing have been observed on Pt(111).[58,59] When the 0.5 ML Pt clusters are oxidized in a flow of O_2 at 550 K following exposure to DMMP and

heating to 800 K, the P(2p) signal decreases by 86%. However, the integrated Pt(4f) intensity is reduced by only 18%, indicating that encapsulation is less extensive under these conditions. Indeed, the studies in the literature report that Pt encapsulation on TiO_2 is only observed in a reducing environment (H_2, vacuum) but not under oxidizing conditions.[40,60-62] Therefore, it is possible that the encapsulation effects and subsequent loss of Pt activity would not be observed if the surfaces were treated under an atmosphere of O_2. Higher oxidation temperatures caused a substantial drop in Pt signal without changing the phosphorus signal appreciably, but this loss in Pt surface area could also be attributed to sintering.

Comparison with DMMP reaction on Pt(111)

The decomposition of DMMP on Pt(111) has been investigated in detail with a combination of secondary ion mass spectroscopy, high resolution electron energy loss spectroscopy, TPD, and AES.[63] In these studies, DMMP is reported to bind via the oxygen lone pair on the phosphoryl oxygen, and decomposition occurs above 300 K to form CO and H_2 as the gaseous products. Between 300 and 400 K, $PO-CH_3$ bond scission occurs, producing H_2 from subsequent decomposition of the methoxy species. Although some $P-OCH_3$ bond scission also occurs, the majority of the P-O bonds are intact at 400 K. Between 400 and 500 K, $P-CH_3$ bonds are broken, and surface PO as well as a PO_x species are observed above 550 K. The lack of CO_2 production suggests that there is no atomic oxygen on the Pt surface at temperatures below that of CO desorption. Catalytic decomposition of DMMP on Pt(111) is limited by the ability to remove phosphorus from the surface. After heating DMMP to 800 K, exposure to $1x10^{-7}$ Torr O_2 at 800 K did not induce desorption of PO_x but instead increased the phosphorus concentration at the surface due to migration out of the bulk.

On the TiO_2-supported 0.5 ML Pt clusters, the details of the reaction mechanism for DMMP decomposition are not known, but chemistry is qualitatively the same as on Pt(111) at temperatures below that of Pt encapsulation by TiO_x. For example, CO and H_2 are the major gaseous decomposition products from DMMP reaction on the Pt clusters, while methyl is associated with reaction on the titania support. The C(1s) XPS data for DMMP on the Pt clusters shows that DMMP decomposition occurs even at room temperature. Although all of the intermediate species cannot be conclusively identified, the XPS data is consistent with $P-OCH_3$ and $PO-CH_3$ bond scission occurring before $P-CH_3$ bond breaking since the integrated C(1s) intensities corresponding to the methoxy (287.8 eV) and methyl (286.3 eV) groups in DMMP are significantly less than 2:1, respectively. The high temperature CO peak from oxidation of atomic carbon has *greater* intensity than the low temperature peak, suggesting that C-O bond breaking occurs in the methoxy groups. Based on the 1:2 ratio of methyl to methoxy carbons in DMMP, the high to low temperature peak ratio should be no greater than 1:2 in the absence of C-O bond scission. Since methanol on Pt(111) is known to decompose via a methoxy intermediate that undergoes dehydrogenation to produce CO and H_2 without C-O bond breaking,[64] it is likely that $PO-CH_3$ bond breaking is also more facile than $P-OCH_3$ bond breaking on the Pt clusters.

There are two major differences between DMMP decomposition chemistry on TiO_2-supported Pt clusters and on Pt(111). First, atomic carbon can be removed from the clusters by oxidation to CO via the participation of lattice oxygen; oxidation of surface carbon by lattice oxygen has also been observed on TiO_2-supported Ni clusters.[13,48] Second, encapsulation of the Pt clusters by TiO_x due to SMSI is extensive after heating above 600 K, with complete encapsulation at 800 K. The high activity for DMMP decomposition is lost in this process, and the encapsulated clusters exhibit activity similar to that of titania. Phosphorus is removed from

the surface after oxidation at 800 K, but a simultaneous decrease in Pt signal also occurs due to encapsulation of the clusters. Notably, removal of surface carbon by lattice oxygen also requires temperatures that induce complete encapsulation of the Pt clusters.

Au and Au-Pt clusters

TPD experiments for DMMP reaction on the 0.5 ML Au clusters show that Au is less active than Pt for DMMP decomposition. Although the same products are observed as for reaction on Pt, the intensities are much lower on Au (Figure 18a). CO (28 amu) is the main decomposition product from reaction on the Au clusters, and a peak at 465 K is detected as well as a high temperature feature at 890 K, which is attributed to recombination of atomic carbon and lattice oxygen. A small H_2 signal (2 amu) is observed around 600 K, but methyl and methane are the main hydrogen-containing products, indicating that C-H bond scission is less favored on Au compared to Pt clusters. The similarity in methyl peak shape on the Au clusters and on titania suggests that methyl production is from reaction on exposed titania. In contrast, methane production occurs at lower temperature than on titania, and the peak shape for methyl desorption is similar to that for reaction on the Pt clusters. The desorption of DMMP (94 amu) occurs in a peak centered at ~420 K, as observed on the TiO_2 surface and the 0.5 ML Pt clusters.

TPD data for DMMP reaction on both the 0.25 ML Pt+0.25 ML Au clusters illustrate that the activity on the bimetallic Au-Pt clusters is intermediate between that of pure Au and pure Pt (Figure 18b). Specifically, the intensities of CO and H_2 peaks are greater than on pure Au but smaller than on Pt although the peak temperatures are the same for all three surfaces. As expected, the methyl signal from reaction on the titania support is decreased compared to the pure Au clusters, given that the Au-Pt clusters cover more of the titania surface. Notably, methane production on the Au-Pt clusters is higher than on either pure Pt or pure Au. DMMP desorption from the bimetallic surface occurs in a peak at 420 K.

DMMP decomposition was also carried out on Au-Pt bimetallic clusters with Au compositions ranging from 25-90%. The yields for H_2, methyl, methane and low temperature (465-530 K) CO desorption are shown in Figure 19 as a function of bimetallic composition. On all of the bimetallic Au-Pt surfaces, no products other than CO, H_2, methane and methyl were detected, indicating that Au-Pt sites did not exhibit synergistic activity that resulted in new reaction pathways. Both H_2 and CO production decrease with increasing Au composition although the H_2 signal drops off more rapidly than CO. These results suggest that decomposition to H_2 and CO are associated with reaction at Pt sites. The more rapid decrease in H_2 production supports the idea that substantial CO formation also occurs at Au sites whereas almost no H_2 is produced on Au. The slight increase in methyl yield with increasing Au composition is consistent with the methyl formation from reaction on exposed titania. Due to the higher mobility of Au atoms on TiO_2 compared to Pt, larger clusters are formed with increasing Au content, and this results in a higher fraction of exposed titania. For comparison, note that the methyl signal is 73% of that on TiO_2 for the 0.5 ML Au clusters and 35% for the Pt clusters.

Methane production on all of the bimetallic surfaces is greater than that on pure Pt, pure Au or clean TiO_2, suggesting there is greater selectivity for methane formation at Au-Pt sites. The greater production of methane is the only evidence that the Au-Pt sites have activity that is different from that of pure Au and pure Pt. The higher methane yields on the bimetallic clusters also suggest that hydrogenation of methyl is favored over dehydrogenation at Au-Pt sites compared to pure Pt, where C-H bond scission readily occurs.[64] On pure Au, the low methane production may be attributed to lower probability of forming a CH_3 intermediate that can be

hydrogenated to methane due to reduced P-CH$_3$ bond scission in DMMP or O-CH$_3$ bond scission in a surface methoxy intermediate. The decrease in CO and H$_2$ product yields on Au-Pt compared to Pt suggests that P-OCH$_3$ bond breaking is also inhibited since this is believed to be the first step in DMMP decomposition on Pt to produce CO;[63] the diminished activity for P-OCH$_3$ bond breaking is also observed on the pure Au clusters.

XPS data for the C(1s) and P(2p) regions were collected after exposing DMMP to the 0.5 ML Au and 0.25 ML Pt+0.25 ML Au clusters and heating to various temperatures. The data for the C(1s) regions are not shown here because on both surfaces, the spectra are qualitatively the same as on the Pt clusters (Figure 16b). Specifically, the spectrum at room temperature can be fit with peaks from methyl and methoxy carbons in DMMP at 286.3 eV and 287.8 eV, and a peak from a lower binding energy decomposition species at 284.8 eV. Heating above room temperature causes the C(1s) peak to shift to lower binding energy as more C-P and C-O bonds are broken. Furthermore, the total carbon signal decreases with increasing annealing temperature due to the desorption of carbon-containing products such as CO, methyl and methane. At 1000 K, the carbon signal is barely detectable above the noise on all of the cluster surfaces.

The main differences in the P(2p) regions for DMMP on the pure Pt, pure Au and Au-Pt clusters are illustrated in Figure 20, which shows the spectra acquired after heating to 800 K. On the 0.5 ML Pt clusters, the 134 eV peak assigned to PO$_x$ is observed at 800 K as well as at lower annealing temperatures. However, another peak at 129.5 eV is detected with roughly equal intensity and is ascribed to atomic phosphorus on Pt. There is a small signal contribution at 129.5 eV even at 600 K, but a distinct peak is not observed until 800 K. For the 0.5 ML Au clusters, the 134.0 eV peak is the dominant feature in the spectrum although a smaller contribution from atomic phosphorus on Au is also observed, suggesting that P-O bond scission is less facile on Au compared to on Pt. As on the Pt clusters, the PO$_x$ and atomic phosphorus peaks exhibit equal intensities on the Au-Pt clusters. The rising baseline observed in the P(2p) spectrum for Au and Pt+Au is due to signal from the intense Au(4f$_{7/2}$) peak at lower binding energy. On the Pt and Pt+Au clusters, the disappearance of the 134.0 eV peak after heating to 1000 K demonstrates that all P-O bonds are broken at this temperature. On the Au clusters, the phosphorus signal completely disappears at 1000 K.

A comparison of the integrated P(2p) intensities as a function of annealing temperature is shown in Figure 21 for the Pt, Au and Au-Pt clusters. At all temperatures, the phosphorus signal is highest on the pure Pt clusters, and this can be explained by the greater activity of Pt for DMMP adsorption and decomposition. Similarly, the phosphorus signal is slightly higher on the bimetallic Au-Pt clusters compared to pure Au. All three cluster surfaces exhibit a drop in P(2p) signal between room temperature and 600 K due to the desorption of molecular DMMP over this temperature range. Between 600 K and 800 K, there is no appreciable change in signal for any of the surfaces, but at 1000 K, the phosphorus signal decreases in all cases. For the pure Au clusters, the phosphorus signal drops to zero at 1000 K. This is consistent with phosphorus desorption (31 amu) at ~900 K observed in the TPD experiments and the desorption of Au at the same temperature; in contrast, neither Pt nor phosphorus on Pt desorbs from the surface below 1100 K. For the Pt and Au-Pt clusters at 1000 K, the P(2p) signal decreases to 60 and 34%, respectively, of the intensities at 600 K. Since the desorption of phosphorus-containing products is not detected above 600 K on pure Pt clusters, the loss of surface phosphorus on Pt is attributed to migration into the bulk. However, phosphorus desorption at 31 amu is also observed on Au-Pt clusters.

The presence of Au inhibits P-O bond scission, which is facile on Pt after heating to 800 K. A previous report of DMMP on Pt(111) suggested that PO_x is more easily removed from the surface during oxidation than atomic phosphorus because the diffusion of phosphorus into the bulk should be inhibited in the PO_x species;[63] this hypothesis is consistent with the more facile removal of phosphorus from Au compared to Pt surfaces since the P-O bonds are mostly intact for the former. While phosphorus does not desorb from the Pt clusters, it does desorb from the Au clusters as well as Au(50%)-Pt bimetallic clusters. This is either because intact P-O bonds promote phosphorus desorption although no PO_x species could be detected in the TPD experiments, or because phosphorus is removed during the desorption of Au itself at ~900 K, whereas Pt does not desorb from titania. Oxidation of phosphorus on Au-Pt at 600 K also resulted in a ~40% drop in the both the phosphorus and platinum Auger signals, again suggesting that the loss in intensity is due to encapsulation of the clusters rather than removal of phosphorus by oxidation.

Conclusions for DMMP on TiO$_2$, Pt and Au-Pt

Despite the higher activity of the Pt and Au-Pt clusters for DMMP decomposition, the $TiO_2(110)$ support exhibits more promising catalytic activity because of its ability to sustain activity over multiple cycles of adsorption and reaction. On the titania surface, C-H bond scission is less facile than on Pt, but C-O bond scission occurs readily. Furthermore, phosphorus can be removed from TiO_2 by heating to 965 K in UHV or 800 K in O_2, restoring activity for DMMP decomposition. The Pt clusters have higher initial activity for DMMP reaction compared to TiO_2, but activity is suppressed after a single adsorption-reaction cycle due to encapsulation of the Pt clusters by reduced titania upon heating, as well as poisoning of active sites by phosphorus-containing byproducts. Phosphorus removal from the Pt clusters by high temperature oxidation is complicated by the fact that heating in O_2 accelerates the encapsulation of the Pt clusters, and the encapsulated clusters exhibit activity characteristic of TiO_2, not Pt. The addition of Au to the Pt clusters diminishes the overall activity while allowing phosphorus to desorb from the surface at 900 K. However, significant cluster sintering, Au desorption and encapsulation of the Au-Pt clusters occur at 900 K, and therefore the morphologies of the clusters are dramatically changed after phosphorus removal. The activity of the Au-Pt bimetallic clusters is intermediate between that of pure Pt and pure Au in terms of DMMP decomposition to CO and H_2. The production of new products from synergistic chemistry is not observed, but hydrogenation of methyl to methane is promoted at Au-Pt sites.

Decomposition of Methanethiol on Supported Ni clusters
Scanning Tunneling Microscopy Studies

STM images of the various Ni surfaces studied here are shown in Figure 22 as a function of coverage and annealing temperature. We report only height as a measure of cluster size because the diameters of the clusters are known to be overestimated by a factor of ~2 due to tip convolution effects, and furthermore the clusters formed at higher coverage do not have regular shapes with distinct diameters. The deposition of 1 ML of Ni at room temperature produces clusters with an average height of 16±2 Å. When the coverage is increased to 2.5 ML, the average cluster height increases to 18±2 Å, and there is also a significant increase in the width of the features, which have no longer have distinct circular footprints due to cluster coalescence that produces more irregular shapes. At 5 ML, the average feature height further increases to 20±3

Å, and the clusters are much more irregular in both the size and shape due to extensive cluster coalescence; this surface begins to resemble a Ni film rather than individual clusters. When the 1 ML Ni clusters are heated to 850 K, an increase in average cluster height to 20±3 Å is accompanied by a decrease in cluster density. Heating the 2.5 ML Ni clusters to 850 K does not preserve the identity of individual clusters. Instead, large features with heights of 27±4 Å coexist with smaller, partially coalesced clusters so that the surface has the appearance of large particles supported on a rough film. After heating the 5 ML Ni clusters to 850 K, there is a substantial increase in both the height (43±8 Å) and width of the clusters. However, smaller partially coalesced clusters again observed, giving the surface a more film-like appearance.

Temperature programmed desorption

The reaction of methanethiol was initially carried out on titania and oxidized titania in order to understand potential reactivity on the support surface itself. On both the oxidized (Figure 23, bottom) and unoxidized (data not shown) surfaces, very little methanethiol reaction occurs since no sulfur was observed in the Auger spectrum, and only trace amounts of 16 amu (methane) were produced in the TPD spectrum. Methane desorbs in a broad peak that is centered at 400 K and extends from 200-600 K; this signal represents 5% of the 16 amu signal detected from reaction on 5 ML of Ni. No other products, including H_2(2 amu), H_2O(18 amu) and CO (28 amu) were detected in these experiments. On the both surfaces, the desorption of condensed methanethiol (47 amu) is observed at 121 K, and two other physisorption states are observed at 250 K and 360 K. The oxidized surface is slightly less active for methanethiol reaction since the integrated intensity of the methane peak is ~10% smaller than on the unoxidized surface, and therefore all TPD and XPS experiments were carried out on the oxidized titania so that reaction on the support would be minimized.

As a Function of Ni Coverage

Methanethiol reaction was then studied on Ni clusters with coverages ranging from 0-5 ML. Reaction on the Ni surfaces produced methane (16 amu) and hydrogen (H_2) as the major gaseous products, while methanethiol desorption (47 amu) was also detected (Figure 23). All masses between 1-100 amu were monitored, and no additional products were detected below 700 K, the temperature above which no further decomposition of methanethiol occurs. The production of methane and methanethiol were confirmed by comparing the ratios of the 15:16 signal for methane and the 47:48 signal for methanethiol in the TPD experiments with the cracking patterns for the respective desorption species. The addition of a small amount of Ni (0.1 ML) to the TiO_2 surface substantially increases methane production, which is observed in a broad peak centered at 320 K. Although oxidation did not completely suppress the activity of titania, the deposition of a small amount of Ni decreased the activity so that the trace methane desorption at 400 K is no longer detected; this behavior indicates that the nucleation sites for Ni are the same as the actives sites on TiO_2 for methanethiol reaction. At 0.5 ML of Ni, the methane production shifts to lower temperature, and a more distinct peak appears at 285 K. As the Ni coverage is increased up to 5 ML, the intensity of the methane desorption peak increases, and the initially broad desorption peak becomes sharper, suggesting that methane production on the Ni surface is dominated by reaction at a single type of site.

Hydrogen production from methanethiol decomposition is first observed at 0.1 ML of Ni as a small peak at 260 K. The intensity of this peak increases as the coverage is increased to 0.25 ML and remains approximately the same at 0.5 ML. Between 1 ML and 5 ML, the hydrogen peak

intensity continues to increase with Ni coverage and shifts to higher temperature, appearing at 300 K for the 5 ML coverage. Furthermore, a broad, higher temperature desorption shoulder initially appears for the 2.5 ML coverage and becomes more pronounced at 5 ML, indicating that different types of surface sites contribute to the production of hydrogen. At submonolayer coverages, the onset of H_2 desorption is shifted to lower temperature by 25 K compared to desorption from the 1 ML Ni clusters. However, between 1 ML and 5 ML, the continued shift to higher desorption temperatures is from broadening of the peak to higher temperatures rather than a change in the onset temperature.

Only small differences in the desorption of physisorbed methanethiol (47 amu) are observed as a function of Ni coverage (Figure 23). For all coverages, the multilayer desorption peak appears between 115 and 120 K and grows with increasing methanethiol exposure. The first physisorption peak occurs at 240 K, while a second, smaller peak is found at ~360 K. In general, the intensity of the 360 K peak decreases with increasing Ni coverage, and this behavior is consistent with weaker binding of methanethiol to TiO_2 compared to Ni, as well as the higher activity of the Ni surfaces.

A plot of normalized product yields as a function of Ni coverage is shown in Figure 24. Both the 2 and 16 amu signals are normalized to the highest intensity, which is observed for reaction on the 5 ML Ni clusters. Since hydrodesulfurization of methanethiol produces only methane while nonselective decomposition produces only H_2, the methane and H_2 signals can be used to determine the relative contributions of the two reaction pathways. For both products, there is a sharp and nearly linear increase in product yields as the coverage is increased to 0.5 ML, but between 0.5 and 1.0 ML, the product yields are similar. The initial rise in production for both hydrogen and methane is consistent with methanethiol reaction on the Ni clusters, which increase in Ni surface area with increasing coverage; between 0.5 and 1.0 ML the Ni surface area should still increase with coverage, but apparently the number of active sites does not increase significantly. Above 1 ML, the product yields increase again almost linearly with increasing Ni coverage, presumably due to an increase in both Ni surface area and active sites. Methane and hydrogen production follow the same general trends with Ni coverage although the more rapid rise in methane production at coverages below 1 ML suggests that hydrodesulfurization is slightly favored on the smaller clusters compared to the more film-like 5 ML coverage. This may be due the fact that the Ni film has more defect sites that favor nonselective decomposition.

As a function of annealing

Methanethiol reaction was also investigated on the 5 ML Ni clusters heated to 700 K, 750 K, 800 K and 850 K to create different surface morphologies with larger clusters formed at higher temperatures (Figure 25). After heating to 700 K, the intensity of the methane peak from methanethiol reaction is reduced compared to the unheated 5 ML surface, and the peak temperature is shifts from 286 K to 293 K. Heating to 750 K further decreases methane production and results in desorption from two states: a shoulder at 270 K and a peak at 297 K. Heating to 800 K decreases the methane production to nearly zero, but the same two desorption states at 270 and 297 K are still discernable, and heating to 850 K continues to decrease the methane signal. In terms of hydrogen production, the same peak positions and peak shapes are observed on the surfaces after heating to 700 and 750 K, but the desorption intensity is decreased compared that on the unheated surface. On the surface heated to 800 K, the hydrogen signal is barely detectable, and no hydrogen is produced on the surface heated to 850 K. For methanethiol desorption on the Ni surfaces, the temperature for multilayer desorption is unchanged as

expected. However, amount of methanethiol that desorbs around 240 K is much larger on the surfaces heated to 700 K and above, indicating that there is less reaction and more desorption from physisorbed states on the surfaces heated to high temperatures.

Changes in product yields and total reactivity with annealing temperature are summarized in Figure 26. The S(LMM):Ti(LMM) Auger ratio after TPD of methanethiol to 930 K is used as a measure of total reaction since no sulfur-containing products other than methanethiol itself desorbs from the surface. Auger ratios and product yields are normalized to the highest value at 500 K. The methane and hydrogen yields both decrease with annealing temperature at approximately the same rate, demonstrating that reaction selectivity does not change as the surfaces are annealed. The main effect of annealing is to decrease the activity of the Ni clusters so that there is more than an 80% drop in activity after annealing to 800 K and almost no activity after annealing to 850 K. The decrease in total reaction with annealing temperature follows the same trend as the product yields, confirming that methane and hydrogen production represent the only two reaction pathways. At 700 K, the total reaction is 65% of the initial value, and at 800 and 850 K the total reaction drops to 10% of the initial value.

At temperatures above 700 K, CO desorption is observed in TPD experiments for methanethiol reaction on Ni coverages of 2.5 ML and higher. The production of CO does not indicate another reaction pathway but instead is from the oxidation of atomic carbon, which is a byproduct of nonselective decomposition. When the TiO_2 surface is oxidized with $^{18}O_2$, methanethiol reaction on the Ni clusters produces isotopically labeled $C^{18}O$ (30 amu) as shown in Figure 27. Thus, CO must be produced from the recombination of lattice oxygen from titania with atomic carbon, which is deposited on the Ni clusters during nonselective decomposition of methanethiol. On the 2.5 ML clusters, the CO peak appears around 850 K, and as the coverage is increased to 5 ML, this desorption peak grows larger with the main intensity shifting to 885 K. The absence of CO desorption from the 0.1-1 ML Ni clusters is attributed to the lower absolute coverage of surface carbon, given that the amount of total reaction and nonselective decomposition is lower on the Ni surfaces with smaller metal coverages. Notably, the desorption of CO itself from the 2.5 ML Ni surface occurs at 470 K and 760 K, indicating that CO production from the decomposition of methanethiol occurs at higher temperatures than simple recombination of atomic oxygen and carbon.

In contrast to the decrease in methane and hydrogen production observed upon annealing the 5 ML Ni clusters, the production of CO is initially increased after heating to 700 K, and the peak temperature is ~80 K lower compared to that on Ni clusters flashed to 500 K (Figure 27). Additional heating to 750 K results in somewhat reduced intensity although the desorption temperature remains approximately the same, and after heating to 800 K, the CO peak has a much smaller intensity and shifts to 828 K (data not shown). The absence CO signal detected from methanethiol reaction on the 5 ML Ni clusters heated to 850 K is consistent with the lack of activity on the Ni clusters annealed to high temperature. TPD experiments in which the titania surface is initially oxidized with $^{18}O_2$ before Ni deposition again demonstrate that the CO production involves oxygen from the titania lattice since $C^{18}O$ at 30 amu is observed. Notably a 28 amu signal from $C^{16}O$ is *not* detected in the TPD experiments, indicating that all of the oxygen that participates in carbon oxidation must come from the surface region.

Low energy ion scattering studies

LEIS experiments were carried out to establish the surface area of the 5 ML Ni clusters after heating, and Figure 28 shows the integrated Ni LEIS signals as a function of annealing

temperature. When the Ni clusters are flashed to 500 K, there is no appreciable change in signal, indicating the surface morphology is unchanged. However, heating to 700 K reduces the signal to 74% of the value at room temperature, and this decrease is consistent with the observed decrease in methanethiol product yields and total reactivity to 60-70% of the initial values. After heating to 750 K, the Ni signal drops to 22% of the room temperature value, and the Ni signal disappears completely after heating to 800 and 850 K. The loss of Ni surface area is attributed to encapsulation of the Ni clusters by titania after annealing, given that only titanium and oxygen are observed on the surface, the STM experiments show that large clusters still exist on the surface, and Ni does not desorb from the surface. Apparently, the titania-covered Ni clusters have some activity for methanethiol reaction after annealing to 800 and 850 K because product yields are reduced to ~10% of the room temperature value rather than decreasing to zero.

X-ray photoelectron spectroscopy studies
Conventional XPS

Grazing angle XPS experiments were conducted in order to investigate the nature of the encapsulating layer of titania on the annealed 5 ML Ni clusters (Figure 29). Spectra were acquired at a detection angle 50º off normal to enhance the surface sensitivity so that the oxidation states of the encapsulating titania layer could be distinguished from the much greater signal from bulk titania. The Ti(2p) region for the 5 ML Ni clusters at room temperature and heated to 500 K shows that there is no reduction of titania after heating to 500 K. The peak shapes and peaks positions are the same at these two temperatures, and the Ti($2p_{3/2}$) binding energy at 459.3 eV corresponds to Ti^{+4}.[9,43] When the clusters are heated to 700 K, a low binding energy shoulder appears and is attributed to a combination of Ti^{+3} and Ti^{+2} oxidation states, which have binding energies of 457.7 and 456.2 eV, respectively.[9,43] After heating to 750 K, there is an overall increase in signal intensity due to Ni sintering and also migration of titania on top of the Ni clusters. In addition, the relative intensity of the high binding energy shoulder increases with respect to the Ti^{+4} peak due to further reduction of titania. At the higher annealing temperatures of 800 and 850 K, there is no additional change in the intensity of the high binding energy shoulder, but the Ti^{+4} peak continues to increase in intensity, presumably due to sintering of the Ni clusters that exposes more of the unreduced support surface. The Ni($2p_{3/2}$) region was also collected (data not shown), and the absence of a shift in the Ni binding energy indicates that Ni is not oxidized.

High resolution XPS
On TiO_2(110)

High resolution XPS studies were carried out at NSLS in order to characterize the sulfur-containing intermediates on the surface as a function of exposure time and temperature. Figure 30 shows the S(2p) region for methanethiol adsorbed at 100 K on the TiO_2 for three methanethiol exposures at 100 K and after heating to 250 K and 400 K. A curve fit of the spectrum using S($2p_{3/2}$):S($2p_{1/2}$) doublets with an energy separation of 1.2 eV and relative intensity ratio of 2:1 indicates that at the lowest exposure of 0.2 L, two sulfur-containing species are detected with S($2p_{3/2}$) binding energies of 162.6 eV and 164.7 eV. The 164.7 eV feature is attributed to condensed methanethiol on the surface, and the intensity of this peak increases without bound at higher exposures. The 162.6 eV feature is tentatively assigned to sulfur in methyl thiolate. The total signal intensity increases with increasing exposure, but methyl thiolate accounts for 25% of

the total sulfur species until the surface becomes saturated at 0.5 L. At higher exposures, only the intensity of the thiol peak increases as more methanethiol is condensed on the surface.

After heating the saturated surface to 250 K, the overall integrated intensity drops by 75%, and the contribution of the methyl thiolate decreases to the total sulfur signal decreased to 50%. The loss of sulfur signal is attributed to the desorption of methanethiol, which occurs at 115 K for the multilayer and 250 K for the higher temperature desorption state. The intensity of the 164.7 eV peak from methanethiol at 250 K is attributed to a chemisorbed or physisorbed state since it exists above the temperature of condensed methanethiol desorption. The 162.6 eV peak assigned to methyl thiolate at 100 K is slightly by 0.2 eV to higher energy at 250 K, but there is no evidence that this feature is a different surface species. After heating to 400 K, only a trace sulfur signal remains on the surface, indicating that methyl thiolate most likely recombines with surface hydrogen to form methanethiol, and this is consistent with methanethiol desorption in the TPD above 250 K. The absence of sulfur signal at 400 K also demonstrates that the 162.6 eV peak cannot be assigned to atomic sulfur. If atomic sulfur is formed at 100 K, it should remain on the surface at 400 K, given that no sulfur-containing products other than methanethiol desorb from the surface.

On Ni clusters

The S(2p) region for different exposures of methanethiol adsorbed onto 5 ML Ni clusters at 100 K is shown in Figure 31a. At the lowest exposure of 0.2 L only one sulfur species is observed on the surface with a $S(2p_{3/2})$ binding energy of 162.4 eV, and this species is assigned to atomic sulfur, based on the binding energies of atomic sulfur on single-crystal Ni surfaces.[65] At 0.4 L, a second species appears at 163.6 eV, accounting for 70% of the total sulfur species, and is attributed to methyl thiolate, which is also observed at approximately this binding energy on single crystal Ni surfaces.[65] Methanethiol at 164.4 eV first appears at a slightly higher exposure of 0.5 L, and this binding energy is identical to that observed for methanethiol on $TiO_2(110)$; the relative contributions of atomic sulfur, methyl thiolate and methanethiol are 38%, 43% and 19%, respectively. At an exposure of 1.7 L, intensities for all three sulfur-containing species increase with small increase in the relative contribution of methanethiol to 26%. At 3.5 L, methanethiol becomes the dominant feature in the S(2p) spectrum, accounting for 60% of the total sulfur species with methyl thiolate at 23% and atomic sulfur at 17%. For exposures above 3.5 L, only the intensity of the methanethiol peaks increase, demonstrating that the surface has been saturated. The binding energy of the methanethiol species at 3.5 L appears at 162.3 eV, which is slightly shifted to lower energies compared to the lower exposures, and the methanethiol binding energies for exposures between 1.7 and 3.5 L are also shifted to lower energies, which can be explained by slightly different binding energies for condensed methanethiol and methanethiol bound directly to the surface. The presence of atomic sulfur at 100 K demonstrates that the Ni clusters must be more active than single crystal Ni surfaces, which do not decompose methanethiol to atomic sulfur at 100 K.[65] Furthermore, it is known that the binding energy of the atomic sulfur peak is sensitive to the structure of the Ni surface. Atomic sulfur appears at 161.5 eV on Ni(111) whereas the binding energy on Ni(110) is considerably lower at 162.6 eV[65,66] Therefore, the 162.4 eV binding energy observed in these experiments is consistent with the (110) structure for the surfaces of the Ni clusters.

Figure 31b shows the S(2p) region for a 3.5 L exposure of methanethiol on the 5 ML Ni clusters after heating to various temperatures. At 200 K, the only two sulfur-containing surface species are methyl thiolate at 163.6 eV and atomic sulfur at 162.4 eV, which account for 30%

and 70% of the total sulfur signal, respectively. No methanethiol is observed, and this implies that methyl thiolate and surface hydrogen must recombine to form methanethiol, given that methanethiol desorption is detected at temperatures above 200 K in the TPD experiments. Between 250 and 400 K, only methyl thiolate and atomic sulfur are observed, and methyl thiolate is converted to atomic sulfur as the surface temperature is increased: atomic sulfur comprises 41% of the sulfur-containing species at 250 K and 70% at 400 K. Since all of the methane and hydrogen desorption from the surface occurs below 600 K, only atomic sulfur should remain on the surface at 600 K. The 600 K spectrum shows atomic sulfur as the major surface species, but there is also a high binding energy shoulder which can be fit with a S(2p) doublet from methyl thiolate. However, it is unlikely that methyl thiolate exists on the Ni cluster at this temperature, based on the TPD data and on previous XPS studies of methanethiol reaction on single-crystal Ni surfaces.[65,66] The high binding energy is more likely to be a result of a shakeup feature from final state effects, given that this feature has been observed for atomic sulfur on other metal surfaces, such as Mo and Co.[67] Notably, the intensity of the high binding energy shoulder in the spectrum at 400 K is too large to be completely attributed to the shakeup feature, and therefore methyl thiolate should still exist on the surface at 400 K although some of the high binding energy contribution might be from shakeup effects.

Figures 32a-d compare the S(2p) regions for methanethiol on different Ni coverages and the 5 ML coverage heated to different temperatures after methanethiol adsorption at 100 K. Exposures were 2 L for all of the surfaces except the Ni clusters annealed to 800 K, which were subjected to a lower exposure of 0.5 L; due to the relative inactivity of this surface, exposures above 0.5 L resulted in large quantities of condensed methanethiol on the surface. Although peak fits are not shown for all of the spectra, the binding energies corresponding to the S($2p_{3/2}$) peaks for atomic sulfur and methyl thiolate are marked in Figure 32, and the binding energy corresponding to methanethiol is designated by the S($2p_{1/2}$) peak at 165.5 eV because the S($2p_{3/2}$) peak overlaps with the methyl thiolate doublet. For the 1, 2.5, 5 ML Ni clusters, a mixture of atomic sulfur, methyl thiolate and methanethiol is detected on the surface at 100 K. For the 5 ML Ni clusters heated to 750 K, there is still evidence for thiolate, but comparatively more methanethiol is observed, suggesting a loss in activity upon annealing the Ni clusters. For the 5 ML Ni clusters heated to 800 K, methanethiol is the dominant surface species, and the spectrum resembles that of methanethiol on TiO_2(110), which is much less active than the unannealed Ni surfaces. However, there is also evidence for methanethiol reaction on Ni. The lowest binding energy peak appears at 162.3 eV, which is more consistent with the lower value for atomic sulfur on Ni rather than methyl thiolate on TiO_2. Furthermore, a S($2p_{3/2}$) peak at 163.0 eV is not observed for methanethiol on TiO_2, and this peak is tentatively assigned to methyl thiolate at a different binding site than methyl thiolate at 163.6 eV, as explained later in this section.

At 200 K, a distinct peak from methanethiol is no longer detected on the unannealed Ni clusters, which have only atomic sulfur and methyl thiolate as the surface species. In contrast, methanethiol is still observed on TiO_2 and the Ni clusters annealed to 800 K, which is consistent with at least partial encapsulation of the Ni clusters by titania after high temperature annealing. The Ni clusters annealed to 750 K are clearly more active for methanethiol reaction than the clusters annealed at 800 K, based on the larger overall signal intensity and the greater contribution of methyl thiolate and atomic sulfur to the overall signal compared to methanethiol.

At 250 K, a combination of methyl thiolate and atomic sulfur exists on all of the Ni surfaces, but there are differences in the distribution of surface species. While the S(2p) regions for the 2.5 ML and 5 ML Ni clusters have similar peak shapes, a lower fraction of methyl thiolate has

undergone conversion to atomic sulfur on the 5 ML clusters heated to 750 K. The spectrum for the Ni clusters heated to 800 K is almost unchanged between 200 K and 250 K except for a slight decrease in methanethiol contribution at 250 K. The most notable difference in the distribution of sulfur species is found on the 1 ML Ni clusters, where the contribution of low binding energy surface species is greater than on the higher Ni coverages. However, a peak fit of this spectrum shows that the prominence of the low binding energy features is not due to more complete conversion of methyl thiolate to atomic sulfur but instead is attributed to a shift in the binding energy of methyl thiolate, which is observed at 163.6 eV on the 5 ML Ni and 163.0 eV on 1 ML clusters. Previous studies of methyl thiolate on Ni surfaces have also reported different binding energies for methyl thiolate at different surface sites.[65] There is evidence for several binding sites for methyl thiolate on the 1ML Ni clusters even at 100 K. Over the 100-400 K temperature range the methyl thiolate contribution appears to shift from 163.3 eV at 100 K to 162.8 at 400 and 600 K. However, all of the spectra are also consistent with a changing distribution of methyl thiolate at two different surface sites since the data can be fit with a combination of methyl thiolate peaks at 162.8 eV and 163.6 eV, which is the binding energy observed for the 5 ML clusters.

At 400 K, conversion of methyl thiolate to atomic sulfur is nearly complete on the unannealed Ni clusters although more of a high binding energy shoulder from residual methyl thiolate is observed for the 5 ML clusters. On the annealed clusters, a greater fraction of unconverted methyl thiolate remains, and there is also evidence for a small contribution from methanethiol, which is consistent with the lower activity of the annealed surfaces. For the Ni clusters annealed to 800 K, the distribution of sulfur species is nearly unchanged from that at 250 K; since all of the methanethiol desorbs from titania by 400 K, the persistence of the sulfur signal on the annealed clusters demonstrates that the sulfur species must be adsorbed to either Ni or Ni-modified titania. There is a slight shift in the binding energy of the species attributed to atomic sulfur, which appears at 162.0 eV instead of 162.4 eV as on the unannealed Ni clusters. Between 200 and 400 K, the atomic sulfur signals at ~162.2 eV and methyl thiolate at 163.6 eV are consistent with the sulfur adsorbed to the Ni surface. However, the 164.7 eV peak attributed to methanethiol is more consistent with the higher binding energy of methanethiol on TiO_2 although methanethiol does not remain on pure TiO_2 surface at 400 K in the absence of Ni clusters.

In Figure 33, the total integrated S(2p) intensities after methanethiol exposure and heating to 600 K are used a measure of the total reaction on the surface. The S(2p) signals increase with increasing Ni coverage, following the same trend observed for the TPD product yields. Furthermore, the 40% and 85% drop in total reaction after annealing the 5 ML Ni clusters to 750 K and 800 K, respectively, are completely consistent with the decrease in TPD product yields and S:Ti Auger signals.

Conclusions

Methanethiol reaction on the titania-supported Ni clusters is similar to that on bulk Ni surfaces in that hydrodesulfurization to methane and nonselective decomposition to hydrogen and atomic carbon and sulfur are the two main reaction pathways. On the Ni clusters, it is also possible to oxidize surface carbon with oxygen from the titania support to produce CO above the temperature for complete methanethiol decomposition. Furthermore, XPS experiments show that methyl thiolate is the surface intermediate that produces both methane and atomic sulfur, as on bulk Ni surfaces. Annealing the surface to higher temperatures produces larger Ni clusters,

but strong interactions between the titania support and the Ni results in complete encapsulation of the Ni clusters by reduced titania. These encapsulated surfaces are much less active for methanethiol reaction than Ni but are more active than the titania support itself.

DMMP Chemistry on Ceria
TPD and Conventional XPS Studies
On Stoichiometeric Ceria (CeO$_2$)

The reaction of DMMP on fully oxidized ceria produces formaldehyde (30 amu, CH$_2$O) and methanol (31 amu, CH$_3$O) as the major gaseous products (Figure 34a). The main desorption peaks for both products occurs at 575 K, but small desorption features are also observed at 440 K; trace amounts of H$_2$O desorption are detected at 575 K. Furthermore, a smaller high temperature peak for formaldehyde appears at 800 K and is accompanied by H$_2$O desorption (18 amu) at the same temperature. The evolution of DMMP itself is monitored at 79 amu (PO$_3$) since this is one of the more intense large fragments of DMMP observed in the mass spectrum. DMMP evolution occurs at 180 K in a sharp peak that is attributed to multilayer desorption, but there are also smaller desorption features at 240 K and 420 K. Masses other than those corresponding to the cracking fragments of the identified products are not observed. Specifically, there is no H$_2$ (2 amu), methane (16 amu), CO$_2$ (44 amu), PO (47 amu) and PO$_2$ (63 amu) beyond the intensities expected from DMMP cracking. All of the 28 amu signal at 575 K can be accounted for by cracking of formaldehyde and methanol, demonstrating that the production of CO does not occur; however, the 28 amu signal at 800 K most likely has some contribution from CO. The assignment of the 31 amu peak to methanol is confirmed by the 31:32 amu ratio, which is the same as for pure methanol, and the assignment of 79 amu to DMMP at 420 K is supported by the 47:63:79:94:124 amu ratio for DMMP itself. Similarly, identification of the 30 amu desorption species as formaldehyde is based on the 29:30 amu ratio after both of these signals are corrected for methanol fragmentation. Given that the 30:31 amu ratio for pure methanol leaked into the chamber is roughly 1:10, approximately ~90 % of the 575 K peak at 30 amu is estimated to be from formaldehyde.

To investigate the ability of the ceria surface to sustain activity for DMMP decomposition, TPD experiments were carried out for successive cycles of adsorption and reaction on the same surface. The major reaction products, which are formaldehyde and methanol at 575 K, were monitored over seven reaction cycles (Figure 35). Product yields do not decrease substantially over the first three cycles, but there is a sharp drop off between cycles three and six, with the formaldehyde and methanol yields decreasing to 15-18% of the first cycle values. The drop in product yields is more gradual between cycles six and seven, and the fact that the yields do not decrease to zero after the seventh cycle shows that the surface sustains some activity for DMMP decomposition. The TPD data for the first and second cycles are qualitatively very similar with the main difference being a decrease in DMMP desorption at 420 K for the second cycle. Major changes in the desorption spectra occur only after three cycles of adsorption and reaction. Specifically, the formaldehyde and methanol peaks become significantly broader and shift to higher temperature in addition to losing intensity, as shown in the data for the fourth cycle (Figure 34b). Furthermore, the high temperature water and formaldehyde desorption peaks disappear, and the distinct DMMP desorption peak at 420 K is replaced with a much broader feature extending from 200-400 K. The desorption of dimethyl ether (46 amu) is also observed in the same temperature range as formaldehyde and methanol, and the identity of this product is supported by the 45:46 amu ratio, which matches that for dimethyl ether. The dimethyl ether

formation is not detected until the third adsorption-reaction cycle; its yield reaches a maximum for the fourth cycle and decreases to zero by the seventh cycle.

The ceria films were grown in isotopically labeled $^{18}O_2$ to address the role of lattice oxygen in DMMP reaction (Figure 36). TPD of DMMP on the labeled ceria surface demonstrates that the DMMP desorbed at 420 K exchanges oxygen with the ceria lattice, given that both ^{18}O-labeled (81 amu) and unlabeled DMMP (79 amu) are detected with approximately equal intensities. Furthermore, no oxygen exchange with the lattice occurs in methanol since the 33 amu ($CH_3^{18}O$) signal from the main cracking fragment of ^{18}O-labeled methanol is *not* detected at any temperature, and therefore the ^{18}O-methanol fragments do not contribute to the intensity observed at other masses. Masses 29-32 amu represent a combination of cracking fragments from unlabeled methanol as well as ^{18}O-formaldehyde and ^{16}O-formaldehyde. There is no oxygen exchange in formaldehyde and methanol produced at 420 K because the 29:30:31:32 amu ratios are identical on the labeled and unlabeled surfaces. However, oxygen exchange occurs in formaldehyde production at 580 K: the 31:29 and 32:29 amu ratios are higher on the labeled surface compared to the unlabeled due to increased contributions from masses 31 and 32 amu from the cracking fragments of ^{18}O-formaldehyde. There is only ^{18}O formaldehyde (32, 31, 30 amu) and no unlabeled formaldehyde (29 amu) produced at 780 K, indicating that all of the formaldehyde formed at this temperature undergoes oxygen exchange with the ceria. The formaldehyde produced at 780 K contains only lattice oxygen instead of oxygen from DMMP because this product arises from P-CH_3 bond breaking and combination of CH_3 with lattice oxygen, rather than from P-OCH_3 bond breaking in DMMP. Since the 30:32 amu ratio at 780 K is greater than the corresponding 28:30 amu ratio for unlabelled formaldehyde, some of the desorption at 30 amu is attributed to $C^{18}O$.

X-ray photoelectron spectra for the Ce(3d) region were collected after each of the adsorption-reaction cycles on oxidized ceria to monitor changes in the oxidation state. The spectrum for the stoichiometric surface before DMMP reaction (Figure 37a) exhibits six peaks assigned to three pairs of spin-orbit doublets. The multiple peaks associated with the $3d_{7/2}$ and $3d_{5/2}$ binding energies are due to different final state occupancies in the 3d levels.[68] There are two features that serve as good markers for gauging the level of reduction in the ceria surface: the peak at 916 eV is characteristic of Ce^{+4}, and the peak at 884 eV is characteristic of Ce^{+3} state.[68] After the first DMMP adsorption-reaction cycle, the intensity of the 916 eV decreases while the valley near 884 eV begins to fill in (Figure 37b). The decrease in the 916 eV is more pronounced after the second cycle, and a peak at 884 eV clearly appears (Figure 37c). Further evidence of Ce^{+4} reduction is found after the third and fourth cycles. The extent of reduction can be quantified by fitting the data with a linear combination of the fully oxidized and fully reduced spectra. A plot of % Ce^{+4} as a function of TPD adsorption-reaction cycle (Figure 38, circles) shows a large decrease in Ce^{+4} after first three cycles, with the Ce^{+4} content dropping from 100% to 45%. After cycles 4-7, the decrease in Ce^{+4} is more gradual and diminishes to 30% after the seventh cycle. Notably, the activity for DMMP decomposition also decreases sharply after the third cycle as the Ce^{+4} content drops below 50%, suggesting that Ce^{+4} sites may be important for decomposition activity.

On reduced ceria (CeO$_x$)

DMMP decomposition on an intentionally reduced ceria surface was studied by TPD in order to further elucidate the relationship between surface reduction and activity. The Ce(3d) region in the XPS spectrum (Figure 39a) exhibits peaks at 884 eV and 905 eV characteristic of Ce^{+3}, and

the surface is estimated to be ~65% reduced, based on curve-fitting with the spectra of the fully oxidized and fully reduced films. The TPD of DMMP on the reduced surface produces formaldehyde and methanol as the major products (Figure 40a), but the desorption temperature is 630 K, which is ~55 K higher than on stoichiometric ceria. The desorption of H_2 (2 amu) is also observed at 630 K. After correcting the 28 amu signal at ~600 K for mass fragmentation from methanol and formaldehyde, little if any of the 28 amu signal can be attributed to CO. Formaldehyde desorption is not observed at high temperature, and instead, H_2 and CO production are observed in addition to H_2O at 820-850 K. While the lower temperature methanol peak, which is shifted to 535 K, is more pronounced than on the stoichiometric surface, the formaldehyde peak at this temperature is absent. In contrast to activity on CeO_2, DMMP desorption at 420 K is not observed. Methanol and formaldehyde production decreases only slightly for the second adsorption-reaction cycle on the reduced surface, but there is a dramatic drop in activity for the third cycle (Figure 40b). The formaldehyde and methanol desorption peaks become broader, less intense and shift to high temperature. Furthermore, the water and H_2 peaks at ~630 K disappear completely although water desorption is still observed at 800-900 K. A comparison of the formaldehyde and methanol yields on stoichiometric and reduced ceria as a function of adsorption-reaction cycle is shown in Figure 35. While the initial activity CeO_x is greater than that of CeO_2, the activity for DMMP decomposition on CeO_x drops off more rapidly. XPS data for the Ce(3d) region demonstrate that there is substantial reduction of ceria after the first cycle, but spectral changes after subsequent cycles are less extensive; after the first cycle, the Ce^{+4} content drops from 65% to 45% and further decreases to ~30% after the second and third cycles.

Infrared Spectroscopy Studies
On stoichiometric ceria (CeO_2)
     Infrared spectroscopy experiments were carried out to identify surface intermediates at various stages of the thermal decomposition of DMMP on ceria (Figure 41a). At 200 K, vibrational modes characteristic of intact DMMP are observed; peak assignments are based on the spectra for gas and liquid phase DMMP[69-72](Table 1) as well as DMMP adsorbed on other oxide surfaces[71-75]. The ν (P=O) mode at 1225 cm^{-1} is significantly red-shifted from its gas phase value of 1275 cm^{-1} while the other modes are close to their gas phase values, supporting the interaction between the phosphoryl oxygen and the oxide surface. Other features observed at this temperature include the ν(C-O) in DMMP at 1070 cm^{-1}, δ_a(OCH$_3$) and ρ(OCH$_3$) at 1467 and 1188 cm^{-1}, respectively, and δ_s(PCH$_3$) and ρ(PCH$_3$) at 1311 and 922 cm^{-1}, respectively. After heating to 300 K, most notable change in spectrum is the disappearance of the P=O stretch. This is accompanied by rise in intensity at 1080 cm^{-1}, which is attributed to the ν_s(OPO) vibration in a bridging P species.[71,72,75-79] The ν_a(O-P-O) mode is expected to appear around 1189 cm^{-1}, which overlaps with the ρ(OCH$_3$) mode from adsorbed DMMP. However, at 300 K, the low intensity of this peak compared to ν_s(O-P-O) and the fact that the peak does not increase between 200 K and 300 K suggests that the ν_a(O-P-O) mode does not contribute to the 1188 cm^{-1} peak. It is more likely that the bridging O-P-O species is oriented perpendicular to the surface so that the ν_a(O-P-O) vibration is forbidden by the surface dipole selection rule.
     Between 200 and 400 K, the decrease in intensity for the δ_a(OCH$_3$) and ρ(OCH$_3$) modes indicates P-OCH$_3$ bond scission in DMMP, which produces a methyl methlyphosphonate (MMP) intermediate. In contrast, the P-CH$_3$ rock and deformation modes do not lose intensity, demonstrating that the P-CH$_3$ bonds are not broken at these temperatures. At 500 K, the 1088

cm^{-1} peak from ν_s(OPO) and 1070 cm^{-1} peak from ν(C-O) in the PO-CH$_3$ groups both lose intensity due to continued P-OCH$_3$ and O-P-O bond scission. At 700 K, the complete disappearance of the O-P-O mode demonstrates that all of the bridging phosphorus bonds are dissociated, and the loss of intensity at 1070 cm^{-1} is consistent with complete P-OCH$_3$ bond scission. The PCH$_3$ modes at 1311 and 922 cm^{-1} are still present, indicating intact P-CH$_3$ bonds. In fact, the δ_a(OCH$_3$) peak at 1311 cm^{-1} becomes sharper and more intense after heating to 500 K, and this suggests a change in structure of the surface intermediate.

These spectra are consistent with a methyl phosphonate (MP) species at 700 K and with MP being the majority intermediate at 500 K, given the loss in intensity for the δ_a(OCH$_3$) and ρ(OCH$_3$) vibrations. Other changes in the spectrum after heating to 700 K include an increase in intensity at 1045 cm^{-1} peak, and this sharp peak is ascribed to the P-O stretches in an MP intermediate based on previous studies of DMMP on metal oxides.[73,74] Work by Tripp et al. suggests that on TiO$_2$ and WO$_3$ powders, MP bound to three lattice oxygen atoms remains on the surface above 623 K; this assignment is supported by infrared spectra that exhibit peaks at 1150, 1050 and 983 cm^{-1}.[74] Based on the infrared spectra of crystalline CePO$_4$ orthophosphate, the 1150 and 1050 cm^{-1} modes are assigned to ν_a(P-O) and the 983 cm^{-1} mode is assigned to ν_s(P-O).[80] Infrared spectra for Na$_2$CH$_3$PO$_3$ in solution also shows P-O modes at 1085, 1050 and 972 cm^{-1}.[81] Furthermore, heating DMMP on magnesia, lanthana and alumina to 673-773 K results in the appearance of modes at 1190-1132 cm^{-1} and 1065-1051cm^{-1} that are attributed to ν(PO$_3$).[73] Although these peak overlap with the positions of the C-O stretching vibrations in DMMP and methoxy as well as ρ(OCH$_3$), the disappearance of the δ(OCH$_3$) and ρ(OCH$_3$) modes illustrates that DMMP and methoxy do not remain on the surface at these temperatures.[73]

At 800 K, the decrease in intensity for δ_s(PCH$_3$) at 1301 cm^{-1} shows that all almost all of the P-CH$_3$ bonds are broken. The intense peak at 1045 cm^{-1} is lost, and a peak at 1025 cm^{-1} appears, in addition to peaks at 987 and 924 cm^{-1}, which were also observed in the spectrum at 700 K. These features are assigned to the P-O stretches of PO$_x$, which is believed to be the main surface species at 800 K. It is unclear why there is a huge decrease in intensity and a shift to lower frequency for the P-O mode originally observed at 1045 cm^{-1}. However, changes in the infrared spspectrum have also been observed for CePO$_4$ crystals heated to different temperatures to induce structural transformations.[82]

The formation of MMP and MP via P-OCH$_3$ bond scission suggests that surface methoxy should also be an intermediate. Determining if surface methoxy appears in the infrared spectra is complicated by the fact that the position of the C-O stretch in methoxy intermediates is known to be sensitive to binding sites. Studies of methanol on ceria powders[69,83] and crystalline thin films[84] report C-O stretches for singly, doubly and triply bound methoxy at 1105-1108, 1058-1065 and 1015-1028 cm^{-1}, respectively,[69,83,84] with the latter two species requiring the existence of oxygen vacancies.[84] At 300 and 500 K, a shoulder at 1058 cm^{-1} appears and could be assigned to methoxy at two-fold sites; the intensity of this feature is difficult to determine since it overlaps with major peaks at 1076 and 1045 cm^{-1}. The presence of a bridging methoxy species at lower temperatures is consistent with the mix of ^{16}O- and ^{18}O- formaldehyde produced at 575 K. At 400 K, the peak at 1020 cm^{-1} could be attributed to three-fold coordinate methoxy, and this feature disappears almost completely at 500 K. Furthermore, in the spectra collected between 300-500 K, there is intensity at 1100 cm^{-1} from the ν_s(OPO) vibration, and it is impossible to rule out some contribution from methoxy at top sites. Thus, the infrared data is consistent with the presence of surface methoxy between 300 and 500 K. Surface methoxy is not expected at 600 K,

Table 1. Assignments for vibrational modes of DMMP on the stoichiometric (CeO_2) and reduced (CeO_x) surfaces at 200 K. For comparison, assignments for gas phase DMMP, liquid phase DMMP, DMMP on alumina at 200 K, DMMP on WO_3 at 300 K, and DMMP on titania at 300 K are also shown. All values are reported in cm^{-1}, and peak positions were determined from infrared spectroscopy experiments, except for the DMMP on alumina data, which is from inelastic tunneling spectroscopy measurements.

	DMMP on CeO_2	DMMP on CeO_x	Gas Phase DMMP	Liquid phase DMMP	DMMP on alumina at 200 K	DMMP on WO_3 at 300 K	DMMP on TiO_2 at 300 K
δ_a (OCH_3)	1467	1467	1467	1466	1452	1449	1459
$\delta_{a/s?}$ (PCH_3)	1311	1317	1314	1314	1308	1313	1314
ν (P=O)	1225	1230	1276	1245	----	1223	1237
ρ (OCH_3)	1188	1189	1190	1186	1177	1193	1186
ν (CO)	1068	1063	1048-73	1038-65	1048	1036-58	1037-61
ρ (PCH_3)	922	----	916	915	900	918	919

which is above the desorption temperature for the main methanol and formaldehyde desorption peaks.

On reduced ceria (CeO_x)

On the reduced ceria surface, molecular DMMP is observed at 200 K (Figure 41b), and the spectrum closely resembles that of DMMP on stoichiometric ceria. Adsorption of DMMP via the phosphoryl oxygen is demonstrated by the shift of the P=O 1230 cm^{-1} to lower frequencies while other modes are unshifted compared to gas phase DMMP. After heating to 300 K, the P=O stretch disappears, and the ν_s(OPO) peak at 1078 cm^{-1} grows in as the phosphoryl oxygen is converted to a O-P-O bridging species. The peak at 1063 cm^{-1} from ν(CO) in DMMP becomes more pronounced, and it is possible that both ν(C-O) in DMMP and surface methoxy contribute to the intensity of this peak. As on the stoichiometric surface, heating from 200-400 K causes the intensity of the δ_a(OCH_3) peak to decrease significantly, indicating P-OCH_3 bond breaking to form first MMP and later MP. At 400 K, there is very little MMP on the surface, and at 580 K, the surface intermediate appears to be exclusively MP since the δ_a(OCH_3) peak disappears. The δ_s(PCH_3) mode is more broad on CeO_x compared to CeO_2, perhaps as a result of greater surface site heterogeneity. Furthermore, this peak splits into two features at 300 K and is significantly red-shifted at the higher temperatures, suggesting perturbation of the C-P bonds, which remain intact up to 700 K. The ρ(OCH_3) peak also splits into two features at temperatures of 300 K and higher. The O-P-O mode and C-O stretch from MMP disappear completely at 580 K, and a new peak at 968 cm^{-1} becomes one of the dominant spectral features. The 968 cm^{-1} peak is ascribed to the P-O stretches in a MP intermediate coordinated to lattice oxygen, given that solid cerium phosphate samples also have an infrared band in the 925-996 cm^{-1} range.[80,82] It is unlikely that the 968 cm^{-1} peak is from the P-CH_3 rock because this mode normally appears at a lower frequency of around 922 cm^{-1} and is already absent at lower temperatures even though the δ_s(P-CH_3) peak is still visible. MP is also proposed as an intermediate in DMMP decomposition on the fully oxidized CeO_2 films, but the P-O stretches are observed at higher frequencies, perhaps suggesting that the structural form of PO_x is different on the oxidized and reduced surfaces. A small peak at 1218 cm^{-1} appears at 580 K and remains at 700 K. While this feature cannot be

definitely assigned, it is in the correct frequency range for ν(P=O).[22,69] The intense peak at 1050 cm^{-1} is assigned to ν_a(P-O), as on the stoichiometric surface. At 700 K, the P-CH$_3$ bonds remain intact, and the dominant peaks at 1050 and 968 cm^{-1} lose intensity although smaller features around 1050, 1000 and 973 cm^{-1} can still be detected. These energies are consistent with the vibrational modes of a PO$_x$ species, as discussed in the previous section.

Soft X-ray Photoelectron Spectroscopy Studies

The C(1s) region for DMMP multilayers (10 L exposure) at 100 K shows two main peaks at 288.1 eV and 286.3 eV that correspond to the methoxy and methyl carbons, respectively, in condensed DMMP (Figure 42). [13,44,51] After heating to 200 K, the peaks at 287.8 eV and 286.1 eV are again attributed to the methoxy and methyl carbons in molecular DMMP, and the 1.3:1 peak area ratio compared to the expected 2:1 ratio implies that some decomposition occurs at this temperature. A smaller peak at ~290 eV is also observed and has a binding energy that could be assigned to surface formate.[85] This may have been caused by X-ray induced damage as has previously been observed for formaldehyde and acetone on ceria.[86,87] The presence of molecular DMMP on the surface at 200 K is consistent with the TPD data that show DMMP desorption above this temperature.

At 300 K, the main surface species still appear at ~287.6 eV and 286.2 eV although the ~1:1 peak area ratio indicates more extensive DMMP decomposition. In addition, the valley between these two peaks has filled in, suggesting the presence of a new feature near 287 eV that persists after further annealing at 400 K. This additional feature near 287 eV is assigned to methoxy adsorbed on CeO$_2$, given that methoxy resulting from the decomposition of methanol on CeO$_2$ has a binding energy of 287.2 eV.[85] P-OCH$_3$ bond scission is typically observed as part of the decomposition mechanism of DMMP on metal oxide surfaces and would produce surface methoxy.[71,73,88-90]. At 600 K, the main surface species has a binding energy of ~285.7 eV, and this is the only peak observed after heating to 800 K. This binding energy is lower than any of the previously reported O-CH$_x$ species adsorbed on CeO$_2$[85-87,91] and is therefore likely related to C bound to an electropositive element such as P-CH$_x$ or Ce-CH$_x$. At 900 K, no carbon is detected on the surface.

In terms of overall signal intensity, the integrated C(1s) signal exhibits the sharpest decrease between 100 K and 200 K as condensed DMMP desorbs from the surface. The carbon signal intensity continues to drop between 400 and 600 K, and this can be explained by the desorption of carbon-containing products such has methanol, formaldehyde and molecular DMMP.

The O(1s) spectrum of the ceria film is dominated by the lattice oxygen peak at 530.3 eV, which is the only feature observed in the absence of DMMP. After DMMP adsorption at 100 K, the lattice oxygen peak is significantly attenuated, and two new peaks appear at 535 eV and 533 eV (Figure 43). Based on their relative intensities and the stoichiometry in DMMP, these peaks are assigned to the methoxy oxygens (POCH$_3$) and the phosphoryl oxygen (P=O) in DMMP, respectively; their binding energies are similar to what has been reported for multilayer DMMP on Rh(100).[51] At 200 K, the desorption of multilayer DMMP results in an increase in the intensity of the lattice O peak and a small shift to 524.8 eV for binding energy of the methoxy oxygens. The decrease in intensity between 200 K and 300 K in the peak assigned to POCH$_3$ is partly related to the desorption of DMMP but also due to P-OCH$_3$ bond scission. Some of the P-OCH$_3$ groups persist up to 400 K, which is consistent with the presence of POCH$_3$ species in the C(1s) spectra.

The O(1s) binding energies shift to lower values when the multilayer at 100 K becomes chemisorbed species at 200 K. For example, the phosphoryl O in DMMP shifts to lower binding energy from 533 eV and 532 eV. Similar shifts are generally reported for multilayer vs. chemisorbed species[87] and were also observed for the C(1s) region. As P-OCH$_3$ and P-CH$_3$ bonds are cleaved, new bonds may form between P and surface O. PO$_x$ species are presumably the only non-lattice O-containing species at 800 K and 900 K. As shown at the bottom of Figure 10, these give rise to an O(1s) peak near 532 eV. Therefore, the peak near 532 eV that is present in all spectra from 200 K to 900 K is primarily attributed to PO$_x$. Methoxy and hydroxyl on oxidized CeO$_2$ have binding energies of ~ 531.8 eV,[85] and these species may also contribute intensity to the binding energy region between the lattice O and the PO$_x$ peaks in Figure 43.

The P(2p) region is the most difficult to interpret since there are multiple phosphorus-containing species on the surface at all temperatures, and it is not possible to uniquely identify all species. However, assignments can be made that are consistent with the infrared data and XPS data from the oxygen and carbon regions. The P(2p) signal consists of a P(2p$_{3/2}$) and P(2p$_{1/2}$) peaks that are separated by 1 eV and have a relative intensity ratio of 2:1. For clarity, the position of only the P(2p$_{3/2}$) peak is noted here (Figure 44). As with the O(1s) spectra, features in the P(2p) spectra can be most easily assigned in the spectra recorded at 100 K and after annealing at 900 K. Upon adsorption at 100 K, the dominant feature in the spectrum is the peak at 134.8 eV, which is attributed to molecular DMMP and is in agreement with the binding energy of DMMP on other surfaces.[13,44,49,51] At 900 K, the P(2p) peak at 133.6 eV is ascribed to PO$_x$ species, and this binding energy is consistent with the 133.4 eV reported for CePO$_4$.[92] CePO$_4$ forms when phosphorus-containing molecules react on ceria surfaces and is known to be thermally stable.[93-96] The P(2p) doublet lineshape at 900 K is not as clear as in the spectrum of DMMP at 100 K, suggesting heterogeneity due to different species or adsorption sites.

At 200 K, the peak from molecular DMMP shifts to ~134.5 eV. The appearance of intensity near 133.5 eV reflects the decomposition of P-OCH$_3$ bonds and the formation of PO$_x$ bonds. At 300 K, most of the intensity above 135 eV disappears, and the intensity around 133.5 eV increases as DMMP decomposes and desorbs upon further heating. After heating to 400 K and 600 K, the P(2p) peaks shift to lower binding energy due to surface species that contribute intensity in the 133 eV region. However, the peak maximum shifts to back to higher binding energy after heating to 800 K and 900 K, and this shift may be due to a change in adsorption site, as was postulated for S on CeO$_x$.[97]

On reduced CeO$_x$

The interpretation of the XPS spectra recorded for DMMP adsorbed on CeO$_x$ is very similar to what was obtained on CeO$_2$. As a general rule, the binding energy for similar species adsorbed on a reduced ceria surface have a binding energy that is 0.5-1 eV greater than their counterparts on oxidized ceria.[85-87,91] Similar shifts are seen in the O(1s) (Figure 46) and P(2p) (Figure 47) spectra on reduced CeO$_x$. Compared to the positions on CeO$_2$, the C(1s) peaks associated with P-OCH$_3$ and P-CH$_3$ in DMMP at 100 K on CeO$_x$ (Figure 45) have shifted from 288.1 eV to 288.7 eV, and from 286.3 eV to 287.0 eV, respectively.

In the C(1s) spectrum of DMMP on CeO$_x$, there is a small shift to lower binding energy at 200 K as the multilayer desorbs, and the decrease in the relative intensity of the peak assigned to POCH$_3$ feature implies partial decomposition of these moieties. The intensities of the C(1s) peaks from P-OCH$_3$ and P-CH$_3$ remain nearly equal between 200 K and 400 K, indicating that roughly half of the P-OCH$_3$ groups have decomposed. The intensity around 288 eV between the

P-OCH$_3$ and P-CH$_3$ peaks can again be assigned to methoxy on ceria since methoxy on CeO$_x$ has a C(1s) binding energy of 288 eV.[85] After annealing at 600 K, the C(1s) spectra is quite broad, and the P-CH$_3$ peak shifts to lower binding energy as the remaining P-OCH$_3$ fragments fully decompose. The persistence of intensity around 288 eV suggests that methoxy remains on surface. In addition, a new feature near 285 eV begins to appear, and remnants of this peak are observed even after annealing to 900 K. A feature with a similar binding energy was assigned to a CH$_x$ species bound to Ce following acetone decomposition on CeO$_x$.[87]

In the O(1s) spectra of DMMP on reduced ceria (Figure 46), there is greater separation between the adsorbate related features and the lattice O peak since the adsorbate features are shift to higher binding energy compared to on CeO$_2$. After annealing to 300 K, the peak at ~532.8 eV is much more intense on CeO$_x$ (Figure 12) compared to the peak at 532.2 eV on CeO$_2$ (Figure 10). This is because the binding energies of PO$_x$ and the Ce-OCH$_3$ are nearly coincident on reduced ceria since methoxy on CeO$_x$ appears at 532.8 eV.[85] There is a small shift to lower binding energy as surface methoxy decomposes at higher temperature, suggesting that the PO$_x$ species has a slightly lower binding energy than Ce-OCH$_3$ on CeO$_x$.

The P(2p) spectra show clearer changes at various temperatures on reduced CeO$_x$ (Figure 47) compared to the spectra on CeO$_2$. At 300 K and 400 K, the spectra is dominated by a well-defined P(2p) doublet with a 2p$_{3/2}$ peak near 134.7 eV, and this feature is ascribed to phosphorus in MMP. After annealing to 600 K, the P(2p) peaks shifts to 134 eV as the second methoxy group is removed to form MP. There is only a small binding energy shift (<0.2 eV) between 600 K and 800 K, indicating that MP and PO$_x$ cannot be easily distinguished in the P(2p) spectra on reduced ceria, presumably because the phosphorus atom in MP is coordinated to lattice oxygen. In contrast to behavior on the CeO$_2$ surface, there is also only a small shift back to higher binding energies after annealing to 900 K on CeO$_x$.

Discussion:
Reaction Mechanism:
Based on a combination of TPD, IRAS and XPS data, a reaction mechanism for DMMP decomposition on ceria is proposed. At 200 K, DMMP is chemisorbed to the surface via the phosphoryl oxygen, and XPS data indicate that some decomposition occurs, most likely via P-OCH$_3$ bond scission. The P(2p) data also suggest that a bridging O-P-O species is formed at this temperature. After heating to 300 K, all of the phosphoryl groups are converted to the bridging O-P-O species, and continued P-OCH$_3$ bond scission occurs. Above 400 K, molecular DMMP desorbs as well as a small amount of methanol and formaldehdye. DMMP undergoes oxygen exchange with the ceria, which is consistent with a bridging O-P-O intermediate, whereas no lattice oxygen exchange is found in methanol or formaldehdye at this temperature. At 500 K, P-OCH$_3$ and O-P-O bonds are still observed, mostly likely from a bridging MMP species. There is also evidence that P-OCH$_3$ bond scission below 600 K produces surface methoxy. At 580 K, formaldehyde and methanol desorb from the surface, and exchange with lattice oxygen occurs in formaldehyde but not in methanol. After heating to 700 K, the P-CH$_3$ bonds remain intact in what is assumed to be a MP intermediate, and no intact P-OCH$_3$ or O-P-O bonds from bridging MMP are detected. Formaldehyde and water desorption occur in a broad peak centered around 800 K. The oxygen in formaldehyde is solely from the ceria lattice, and the same is true for water. A proposed mechanism for formaldehyde production is P-CH$_3$ bond breaking to produce a surface CH$_3$ species that binds to lattice oxygen on the ceria surface. Subsequent C-H bond scission produces formaldehyde and releases surface hydrogen, which combines with lattice

oxygen to desorb water. No carbon remains on the surface at 900 K, and the only surface species observed is PO_x.

On reduced CeO_x surfaces, the mechanism of DMMP reaction is the same as on CeO_2 although the product distribution is slightly different. For example, more C-H bond breaking on CeO_x gives rise to CO rather than CH_2O production at high temperatures. Moreover, hydrogen leaves as H_2 rather than H_2O on the reduced, oxygen-deficient surface. The activity for DMMP decomposition is initially higher on CeO_x, but activity shuts down more quickly after only a few cycles of adsorption and reaction.

Comparison with reaction mechanisms on other surfaces:

The mechanism for DMMP decomposition on the crystalline ceria films is similar to what has been observed on a number of other powdered metal oxide surfaces, where surface species such as MMP, MP, methoxy and PO_x have been proposed. On ceria,[98] titania[8,89] alumina,[73] MgO,[73,89] La_2O_3,[73] Fe_2O_3,[73] WO_3[89] and Y_2O_3[75] powders, vibrational spectroscopy has shown that DMMP binds to the surface via the phosphoryl oxygen. The frequency of the P=O stretch is red-shifted from the 1275 cm^{-1} gas phase value[71,72,75,77,99] and in some cases it is proposed that adsorption occurs on the metal cation via the lone pairs on the electron-rich phosphoryl oxygen.[72,73,77,99,100] Computational studies of DMMP on alumina confirm surface adsorption via Al-O=P bond formation [101] and predict the 60-85 cm^{-1} shift to lower energies observed in experiments.[69] Furthermore, on titania,[72,79] yttria,[75] and magnesia,[77,78] the P=O group is converted to a bridging O-P-O species upon heating, as is observed on the ceria films in this work. This is demonstrated by the loss of the P=O stretch at 1234-1214 cm^{-1} and the appearance of P-O modes for PO_x species at 1170-1090 cm^{-1}, such as ν_s(O-P-O) and ν_a(O-P-O) modes at 1085 and 1189 cm^{-1}, respectively.[71,72,75-79]

On most oxide surfaces studied, DMMP decomposition initially occurs via stepwise scission of the P-OCH$_3$ bonds, as illustrated by the loss of intensity in the ν(C-O) mode in DMMP and the appearance of ν(C-O) stretches associated with methoxy.[8,71,73-75,79] The more stable P-CH$_3$ bonds remain intact until higher temperatures ranging from 573 to 673 K.[71,73,74] The exception to these trends is the reducible Fe_2O_3 surface, on which P-CH$_3$ and P-OCH$_3$ bond scission are proposed to occur simultaneously via a Mars van Krevelen mechanism in the 373-473 K temperature range.[73,102] The Fe^{+2}/Fe^{+3} redox couple participates in oxidative P-CH$_3$ bond scission to form H_3CO^- on the surface, and gas phase oxygen is reduced by the surface to complete the redox cycle.[73] Although the highly reducible ceria surface would also be capable of forming a Ce^{+3}/Ce^{+4} redox couple for oxidative P-CH$_3$ bond scission, it is clear that on ceria, the P-OCH$_3$ bond is broken at lower temperature than P-CH$_3$.

The presence of surface hydroxyls is believed to play a key role in these reaction mechanisms. Specifically, the mechanism for P-OCH$_3$ bond scission involves surface hydroxyl groups, which typically adsorb on the metal oxides under ambient conditions.[8,71,73-75,79] Although the P-OCH$_3$ bond is thermodynamically stronger than P-CH$_3$, methoxy is a better leaving group than methyl in nucleophilic displacement reactions.[71] One of the first mechanistic studies of DMMP decomposition of metal oxides was the inelastic tunneling spectroscopy studies of DMMP on alumina from the Weinberg group.[71,103] It was proposed that the MMP intermediate is formed via attack on phosphorus by a nucleophilic surface oxygen. Further decomposition of MMP occurs via attack at the methoxy carbon by nucleophilic surface oxygen or hydroxyls to induce C-O bond scission rather than continued P-OCH$_3$ bond scission;[71] this mechanism was based on the appearance of the O-H stretch at 2440 cm^{-1} associated with

hydroxy methylphosphonate, which receives a proton from surface hydoxyl groups. The hydroxy methyl phosphonate then decomposes to methylphosphonate.[71,103] Work by the Mitchell group on powdered metal oxide surfaces such as Al_2O_3, MgO, and La_2O_3[73] also reports that surface hydroxyls act as nucleophiles, displacing the methoxy groups on the phosphorus atom in DMMP and resulting in methanol production from combination of methoxy and surface hydrogen.[73] Formation of P-O bonds with lattice oxygen make the phosphorus atoms more electrophilic and susceptible to attack by surface hydroxyls. On many metal oxide surfaces, DMMP is also weakly adsorbed on oxide surfaces via H-bonding between surface hydroxyls and the phosphoryl oxygen[8,71,74] although stronger chemisorption occurs via adsorption of P=O to the Lewis acid sites of the metal cation.[8,71]

On surfaces that have been intentionally kept free of most hydroxyls, by either heating or preparing the oxides in vacuum, surface chemistry is still believed to be dictated by residual hydroxyl groups. Titania surfaces that have been intentionally dehydroxylated by heating in vacuum[79] or in an oxygen environment[8] exhibit isolated hydroxyl groups remaining on the surface; these surface hydroxyls undergo hydrogen bonding to physisorb DMMP via the phosphoryl oxygen and also hydrolyze DMMP to form surface methoxy.[8,79] For ytrria powders grown in vacuum by laser-heated gas phase condensation, the O-H stretch of isolated surface hydroxyls at 3705 and 3676 cm^{-1} in the infrared spectrum signifies trace hydroxyls on remaining on the surface.[75] Hydrogen bonding interactions between DMMP and surface hydroxyls broadens the associated O-H peak and shifts it to 3200 cm^{-1}.[75] Furthermore, nucleophilic attack by hydroxyls on DMMP resulted in P-OCH_3 bond scission and formation of surface methoxy groups, which were identified by the ν(CO) at 1065 cm^{-1}.[75]

On the ceria films in our studies, there is no clear evidence of hydroxyls on the surface. The O(1s) region of freshly prepared ceria films did not exhibit signal at ~532 eV, which is the binding energy attributed to surface hydroxyls.[86] Moreover, the ν(O-H) at 3600 cm^{-1} was not observed in the infrared spectrum of the ceria films although this vibrational mode would have reduced intensity for O-H bonds parallel to the surface due to the surface dipole selection rule. Furthermore, surface hydroxyls would be expected to desorb as water upon heating he surface, but no water desorption was observed from the clean ceria films in TPD experiments. Thus, it is unlikely that the presence of surface hydroxyls is the driving force behind DMMP chemistry on the ceria films even though it is impossible to rule out the presence of a small fraction of isolated OH species. The mechanism for DMMP decomposition on the ceria thin films is also believed to be step-wise scission of the P-OCH_3 bonds followed by P-CH_3 bond breaking despite the lack of surface hydroxyls. The infrared spectroscopy experiments clearly show that the P-CH_3 bond remains on the surface until 700 K while the P-OCH_3 bonds are broken by 500 K.

On metal surfaces, the decomposition of DMMP is also consistent with a reaction mechanism of P-OCH_3 bond breaking to form surface methoxy. Thus, the chemistry of DMMP resembles that of methoxy on both metals and metal oxides surfaces. For example, on Ni(111),[104] Pt(111)[63], Ni[13] and Pt[105] clusters supported on TiO_2, and Pd(111),[104] DMMP reaction produces CO and H_2 as the main products, and these are also formed from methoxy decomposition on the respective single-crystal surfaces.[64,106-108] Likewise, formaldehyde is formed from DMMP reaction on TiO_2-supported Cu clusters when methoxy on Cu is known to produce formaldehyde. On Rh(100),[51] the H_2, H_2O, CO, CO_2, and CH_3OH production from DMMP decomposition is also similar to methanol reaction on Rh(100), which forms H_2, CO and CH_3OH as the main gaseous species.[109]

On many oxide surfaces, a PO$_x$ species remains on the surface after decomposition, and this species generally poisons the surface to further DMMP decomposition.[74,99,110,111] The stable phosphonate is believed to be responsible to passivating the surface to DMMP adsorption and reaction.[74] However, the ceria surface is able to sustain activity after seven cycles of DMMP adsorption and desorption, unlike on metal surfaces and metal clusters.[104,105,112] This suggests that ceria is more resistant than metal surfaces to poisoning by phosphorous-containing decomposition byproducts. Similar behavior has been observed for DMMP adsorption and reaction on TiO$_2$(110) surfaces, on which activity is not completely shut down after five TPD cycles.[105] Furthermore, the ceria surface most likely has greater activity than TiO$_2$, given that DMMP decomposition on TiO$_2$(110) is believed to largely occur at oxygen vacancy defects, producing methyl radical as the gaseous product.[13,44] However, after multiple cycles of DMMP adsorption and reaction, the ceria surface could not be reoxidized to regain activity for DMMP decomposition. After the ceria surface was oxidized at 600 and 900 K and in O$_2$ (30 L) following seven cycles DMMP adsorption-reaction cycles, the Ce^{+4} remained at ~40% , and DMMP TPD experiments on this surface showed no activity for DMMP decomposition beyond what was observed before oxidation. Studies of DMMP on powdered titania also demonstrated that although activity for DMMP physisorption is restored by heated titania in oxygen at 675 K and 20 Torr, the activity for decomposition is not recovered.[79]

Comparison with methanol reaction on ceria: common methoxy intermediate

The similarities in the chemistry of methanol and DMMP on ceria thin films provides evidence that DMMP decomposition occurs via a methoxy intermediate. Methoxy was identified by high resolution XPS studies as the only surface intermediate in methanol reaction on CeO$_2$ films grown on Ru(0001).[85] For both DMMP and methanol reaction on the ceria thin films, formaldehyde and methanol desorb at ~560-575 K as the major products, and methoxy was proposed to disproportionate to form methanol and formaldehyde. Moreover, multiple adsorption-reaction cycles for DMMP or methanol resulted in reduction of the ceria. For reaction on Ce^{18}O$_2$, both ^{18}O- and ^{16}O-formaldehyde were observed at 560-575 K.

In the case of methanol reaction, it is proposed that the methoxy intermediate can undergo methyl hopping so that only some of the formaldehyde contains lattice oxygen. This may also occur when methoxy is formed from DMMP reaction although it is possible that lattice oxygen incorporation occurs due to bidentate adsorption of methoxy to form a dioxymethylene intermediate via coordination with lattice oxygen. On crystalline ceria thin films grown in UHV on Cu(111), methanol reaction on the ceria film produced methoxy at 550 K, which was identified by infrared spectroscopy and X-ray photoelectron spectroscopy;[84] formaldehyde was produced from methanol reaction, but CO and H$_2$ were observed as the major products, unlike on the CeO$_2$ films on Ru(0001). However, since CO and H$_2$ are major products formed from methanol reaction on reduced ceria films,[85] the difference in chemistry may be related to the oxidation state of the ceria films on Cu(111).

The main difference between methanol and DMMP reaction is the presence of surface hydroxyls from O-H bond scission in methanol. These hydroxyls give rise to water desorption at 200 K from methanol reaction, whereas water desorption in DMMP reaction is not observed below 800 K because C-H bonds are not broken below this temperature. Furthermore, formaldehyde production from methanol reaction is *not* observed above 800 K ; this is in agreement with the high temperature formaldehyde originating from P-CH$_3$ bond scission during DMMP decomposition to form a methoxy intermediate with lattice oxygen.

Methanol[85] and DMMP reactions are also similar on the reduced ceria films. Both reactions produce CO and H_2, in addition to the formaldehyde and water observed on the stoichiometric surface. For methanol reaction, the H_2 yield increases while the H_2O yield decreases for more highly reduced surfaces, as expected due to deficiency of oxygen in the more reduced films. Furthermore, the temperature of formaldehyde and methanol desorption shifts from 560-575 K to ~640 K for both DMMP and methanol reaction on the reduced surface. It is proposed that the greater number of oxygen vacancies on the reduced surface stabilize both methoxy and OH since it becomes harder to remove lattice oxygen as water.[85]

An earlier study of DMMP decomposition on powdered ceria further supports methoxy as a surface intermediate although the product distribution is not identical to that on ceria thin films. Specifically, work from the Mitchell group involving DMMP decomposition on ceria supported on alumina reports that methanol and dimethyl ether are the primary products formed via a methoxy intermediate.[98] In these studies, it was established that most of the observed activity is from reaction on ceria rather than alumina. The dimethyl ether was proposed to be formed from combination of two surface methoxys and decreased in yield with increasing DMMP exposure. Interestingly, no dimethyl ether was formed in the reaction of methanol itself, which also decomposes on ceria via a methoxy intermediate. Diffuse reflectance infrared spectroscopy studies showed that DMMP decomposition at room temperature produced surface methoxy, and two different binding sites were identified based on the C-O stretch for methoxy: the on top site at 1098 cm^{-1} and 2-fold site at 1047 cm^{-1}.[98,113] However, it should be noted that these two modes overlap with the ν_s(O-P-O) stretch expected around 1058-1085 cm^{-1}.[71,72,75] The lower frequency for C-O stretch for the bridging species compared to the value on pure ceria was explained by methoxy at a bridge site between cerium and aluminum ions.[98]

References

(1)   Iddir, H.; Ögüt, S.; Browning, N. D.; Disko, M. M. *Phys. Rev. B* **2005**, *72*, 081407R.
(2)   Diebold, U. *Surf. Sci. Rep.* **2003**, *48*, 53.
(3)   Maeda, Y.; Fujitani, T.; Tsubota, S.; Haruta, M. *Surf. Sci.* **2004**, *562*, 1.
(4)   Spiridis, N.; Haber, J.; Korecki, J. *Vacuum* **2001**, *63*, 99.
(5)   Mitchell, C. E. J.; Howard, A.; Carney, M.; Egdell, R. G. *Surf. Sci.* **2001**, *490*, 196.
(6)   Santra, A. K.; Yang, F.; Goodman, D. W. *Surf. Sci.* **2004**, *548*, 324.
(7)   Valden, M.; Lai, X.; Goodman, D. W. *Science* **1998**, *281*, 1647.
(8)   Gan, S.; Liang, Y.; Baer, D. R.; Grant, A. W. *Surf. Sci.* **2001**, *475*, 159.
(9)   Ozturk, O.; Ma, S.; Park, J. B.; Ratliff, J. S.; Zhou, J.; Mullins, D. R.; Chen, D. A. *Surf. Sci.* **2007**, *601*, 3099.
(10)   Campbell, C. T. *Surf. Sci. Rep.* **1997**, *27*, 1.
(11)   Zhou, J.; Kang, Y. C.; Chen, D. A. *Surf. Sci.* **2003**, *537*, L429.
(12)   Park, J. B.; Ratliff, J. S.; Ma, S.; Chen, D. A. *Surf. Sci.* **2006**, *600*, 2913.
(13)   Zhou, J.; Ma, S.; Kang, Y. C.; Chen, D. A. *J. Phys. Chem. B* **2004**, *108*, 11633.
(14)   Meusel, I.; Hoffmann, J.; Hartmann, J.; Heemeier, M.; Baumer, M.; Libuda, J.; Freund, H. J. *Catal. Lett.* **2001**, *71*, 5.
(15)   Kobayashi, T.; Ueda, A.; Yamada, Y.; Shioyama, H. *Appl. Surf. Sci.* **2004**, *223*, 102.
(16)   Jiang, Q.; Lu, H. M.; Zhao, M. *J. Phys. Condens. Matter* **2004**, *16*, 521.
(17)   Tsong, T. T.; Ng, Y. S.; McLane, S. B. *J. Chem. Phys.* **1980**, *73*, 1464.
(18)   Bouwman, R.; Sachtler, W. M. H. *J. Catal.* **1970**, *19*, 127.
(19)   Bus, E.; van Bokhoven, J. A. *J. Phys. Chem. C* **2007**, *111*, 9761.
(20)   Park, J. B.; Chen, D. A., in preparation.
(21)   Lang, H. G.; Maldonado, S.; Stevenson, K. J.; Chandler, B. D. *J. Am. Chem. Soc.* **2004**, *126*, 12949.
(22)   Hernandez-Fernandez, P.; Rojas, S.; Ocon, P.; de la Fuente, J. L. G.; Fabian, J. S.; Sanza, J.; Pena, M. A.; Garcia-Garcia, F. J.; Terreros, P.; Fierro, J. L. G. *J. Phys. Chem. C* **2007**, *111*, 2913.
(23)   Luo, J.; Maye, M. M.; Petkov, V.; Kariuki, N. N.; Wang, L. Y.; Njoki, P.; Mott, D.; Lln, Y.; Zhong, C. J. *Chem. Mat.* **2005**, *17*, 3086.
(24)   Wu, H. T.; Tsong, T. T. *Surf. Sci.* **1994**, *318*, 358.
(25)   He, Y. L.; Zuo, J. K.; Wang, G. C.; Low, J. J. *Surf. Sci.* **1991**, *255*, 269.
(26)   Huang, S. P.; Mainardi, D. S.; Balbuena, P. B. *Surf. Sci.* **2003**, *545*, 163.
(27)   Lewis, L. J.; Jensen, P.; Barrat, J. L. *Phys. Rev. B* **1997**, *56*, 2248.
(28)   Ercolessi, F.; Andreoni, W.; Tosatti, E. *Phys. Rev. Lett.* **1991**, *66*, 911.
(29)   Marks, L. D. *Rep. Prog. Phys.* **1994**, *57*, 603.
(30)   Buffat, P.; Borel, J. P. *Phys. Rev. A* **1976**, *13*, 2287.
(31)   Kofman, R.; Cheyssac, P.; Garrigos, R. *Phase Transit.* **1990**, *24-6*, 283.
(32)   Castro, T.; Reifenberger, R.; Choi, E.; Andres, R. P. *Phys. Rev. B* **1990**, *42*, 8548.
(33)   Wang, Z. L.; Petroski, J. M.; Green, T. C.; El-Sayed, M. A. *J. Phys. Chem. B* **1998**, *102*, 6145.
(34)   Cleveland, C. L.; Luedtke, W. D.; Landman, U. *Phys. Rev. Lett.* **1998**, *81*, 2036.

(35)   Qi, Y.; Cagin, T.; Johnson, W. L.; Goddard, W. A. *J. Chem. Phys.* **2001**, *115*, 385.

(36)   *Note 1*.

(37)   Bates, S. P.; Kresse, G.; Gillan, M. J. *Surf. Sci.* **1997**, *385*, 386.

(38)   Overbury, S. H.; Betrand, P. A.; Somorjai, G. A. *Chem. Rev.* **1975**, *75*, 547.

(39)   Zhang, L.; Persaud, R.; Madey, T. E. *Phys. Rev. B* **1997**, *56*, 10549.

(40)   Jennison, D. R.; Dulub, O.; Hebenstreit, W.; Diebold, U. *Surf. Sci.* **2001**, *492*, L677.

(41)   Dulub, O.; Hebenstreit, W.; Diebold, U. *Phys. Rev. Lett.* **2000**, *84*, 3646.

(42)   Pesty, F.; Steinrück, H.-P.; Madey, T. E. *Surf. Sci.* **1995**, *339*, 83.

(43)   Mayer, J. T.; Diebold, U.; Madey, T. E.; Garfunkel, E. *J. Electron. Spectrosc.* **1995**, *73*, 1.

(44)   Ma, S.; Zhou, J.; Kang, Y. C.; Reddic, J. E.; Chen, D. A. *Langmuir* **2004**, *20*, 9686.

(45)   Park, J. B.; Conner, S. F.; Chen, D. A. *J. Phys. Chem. C* **2008**, *112*, 5490.

(46)   Chen, D. A.; Bartelt, M. C.; McCarty, K. F.; Hwang, R. Q. *Surf. Sci.* **2000**, *450*, 78.

(47)   Zhou, J.; Chen, D. A. *Surf. Sci.* **2003**, *527*, 183.

(48)   Ozturk, O.; Park, J. B.; Black, T. J.; Rodriguez, J. A.; Hrbek, J.; Chen, D. A. *Surf. Sci.* **2008**, *602*, 3077.

(49)   Zhou, J.; Varazo, K.; Reddic, J. E.; Myrick, M. L.; Chen, D. A. *Anal. Chim. Acta* **2003**, *496*, 289.

(50)   Greenlief, C. M.; Hegde, R. I.; White, J. M. *J. Phys. Chem.* **1985**, *89*, 5681.

(51)   Hegde, R. I.; Greenlief, C. M.; White, J. M. *J. Phys. Chem.* **1985**, *89*, 2886.

(52)   Lai, Y. H.; Yeh, C. T.; Lin, H. J.; Chen, C. T.; Hung, W. H. *J. Phys. Chem. B* **2002**, *106*, 1722.

(53)   Idriss, H.; Kim, K. S.; Barteau, M. A. *Surf. Sci.* **1992**, *262*, 113.

(54)   Rufael, T. S.; Koestner, R. J.; Kollin, E. B.; Salmeron, M.; Gland, J. L. *Surf. Sci.* **1993**, *297*, 272.

(55)   Zhou, J.; Ma, S.; Kang, Y. C.; Chen, D. A. *Surf. Sci.* **2004**, *562*, 113.

(56)   Bennett, R. A.; Stone, P.; Bowker, M. *Faraday Discuss.* **2000**, *114*, 267.

(57)   Bennett, R. A.; Stone, P.; Bowker, M. *Catal. Lett.* **1999**, *59*, 99.

(58)   Mitchell, G. E.; Henderson, M. A.; White, J. M. *J. Phys. Chem.* **1987**, *91*, 3808.

(59)   Mitchell, G. E.; Henderson, M. A.; White, J. M. *Surf. Sci.* **1987**, *191*, 425.

(60)   Anderson, J. B. F.; Burch, R.; Cairns, J. A. *Appl. Catal.* **1986**, *25*, 173.

(61)   Hilaire, S.; Wang, X.; Luo, T.; Gorte, R. J.; Wagner, J. *Appl. Catal. A* **2001**, *215*, 271.

(62)   Mullins, D. R.; Zhang, K. Z. *Surf. Sci.* **2002**, *513*, 163.

(63)   Henderson, M. A.; White, J. M. *J. Am. Chem. Soc.* **1988**, *110*, 6939.

(64)   Sexton, B. A. *Surf. Sci.* **1981**, *102*, 271.

(65)   Rufael, T. S.; Huntley, D. R.; Mullins, D. R.; Gland, J. L. *J. Phys. Chem.* **1995**, *99*, 11472.

(66)   Huntley, D. R. *J. Phys. Chem.* **1989**, *93*, 6156.

(67)   Chen, D. A.; Friend, C. M.; Xu, H. *Langmuir* **1996**, *12*, 1528.

(68)   Mullins, D. R.; Overbury, S. H.; Huntley, D. R. *Surf. Sci.* **1998**, *409*, 307.

(69)   Lamotte, J.; Moravek, V.; Bensitel, M.; Lavalley, J. C. *React. Kinet. Catal. Lett.* **1988**, *36*, 113.

(70)   Bertilsson, L.; Engquist, I.; Liedberg, B. *J. Phys. Chem. B* **1997**, *101*, 6021.

(71)   Templeton, M. K.; Weinberg, W. H. *J. Am. Chem. Soc.* **1985**, *107*, 97.

(72)   Rusu, C. N.; Yates, J. T. *J. Phys. Chem. B* **2000**, *104*, 12292.

(73)   Mitchell, M. B.; Sheinker, V. N.; Mitnz, E. A. *J. Phys. Chem. B* **1997**, *101*, 11192.

(74)   Kim, C. S.; Lad, R. J.; Tripp, C. P. *Sensors and Actuators* **2001**, *76*, 442.

(75)   Gordon, W. O.; Tissue, B. M.; Morris, J. R. *J. Phys. Chem. C* **2007**, *111*, 3233.

(76)   Kuiper, A. E. T.; Vanbokhoven, J.; Medema, J. *J. Catal.* **1976**, *43*, 154.

(77)   Li, Y. X.; Schlup, J. R.; Klabunde, K. J. *Langmuir* **1991**, *7*, 1394.

(78)   Li, Y. X.; Klabunde, K. J. *Langmuir* **1991**, *7*, 1388.

(79)   Panayotov, D. A.; Morris, J. R. *Langmuir* **2009**, *25*, 3652.

(80)   Masui, T.; Hirai, H.; Imanaka, N.; Adachi, G. *Phys. Status Solidi A-Appl. Res.* **2003**, *198*, 364.

(81)   Bellamy, L. J. *The Infrared Spectra of Complex Molecules*; Chapman and Hall: Thetford, UK, 1975.

(82)   Xu, L.; Guo, G.; Uy, D.; O'Neill, A. E.; Weber, W. H.; Rokosz, M. J.; McCabe, R. W. *Appl. Catal. B-Environ.* **2004**, *50*, 113.

(83)   Freni, S.; Cavallaro, S.; Mondello, N.; Spadaro, L.; Frusteri, F. *Catal. Commun.* **2003**, *4*, 259.

(84)   Siokou, A.; Nix, R. M. *J. Phys. Chem. B* **1999**, *103*, 6984.

(85)   Mullins, D. R.; Robbins, M. D.; Zhou, J. *Surf. Sci.* **2006**, *600*, 1547.

(86)   Zhou, J.; Mullins, D. R. *Surf. Sci.* **2006**, *600*, 1540.

(87)   Senanayake, S. D.; Gordon, W. O.; Overbury, S. H.; Mullins, D. R. *Journal of Physical Chemistry C* **2009**, *113*, 6208.

(88)   Li, Y. X.; Koper, O.; Atteya, M.; Klabunde, K. J. *Chem. Mat.* **1992**, *4*, 323.

(89)   Aurian-Blajeni, B.; Boucher, M. M. *Langmuir* **1989**, *5*, 170.

(90)   Kanan, S. M.; Lu, Z.; Tripp, C. P. *J. Phys. Chem. B* **2002**, *106*, 9576.

(91)   Senanayake, S. D.; Mullins, D. R. *Journal of Physical Chemistry C* **2008**, *112*, 9744.

(92)   Glorieux, B.; Berjoan, R.; Matecki, M.; Kammouni, A.; Perarnau, D. *Appl. Surf. Sci.* **2007**, *253*, 3349.

(93)   Granados, M. L.; Galisteo, F. C.; Lambrou, P. S.; Manscal, R.; Sanz, J.; Sobrados, I.; Fierro, J. L. G.; Efstathiou, A. M. *J. Catal.* **2006**, *239*, 410.

(94)   Larese, C.; Granados, M. L.; Mariscal, R.; Fierro, J. L. G.; Lambrou, P. S.; Efstathiou, A. M. *Appl. Catal. B-Environ.* **2005**, *59*, 13.

(95)   Larese, C.; Galisteo, F. C.; Granados, M. L.; Mariscal, R.; Fierro, J. L. G.; Lambrou, P. S.; Efstathiou, A. M. *J. Catal.* **2004**, *226*, 443.

(96)   Larese, C.; Galisteo, F. C.; Granados, M. L.; Mariscal, R.; Fierro, J. L. G.; Furio, M.; Ruiz, R. F. *Appl. Catal. B-Environ.* **2003**, *40*, 305.

(97)   Mullins, D. R.; McDonald, T. S. *Surf. Sci.* **2007**, *601*, 4931.

(98)   Mitchell, M. B.; Sheinker, V. N.; Cox, W. W.; Gatimu, E. N.; Tesfamichael, A. B. *J. Phys. Chem. B* **2004**, *108*, 1634.

(99)   Segal, S. R.; Cao, L. X.; Suib, S. L.; Tang, X.; Satyapal, S. *J. Catal.* **2001**, *198*, 66.

(100)   Segal, S. R.; Suib, S. L.; Tang, X.; Satyapal, S. *Chem. Mat.* **1999**, *11*, 1687.
(101)   Bermudez, V. M. *Journal of Physical Chemistry C* **2007**, *111*, 3719.
(102)   Tesfai, T. M.; Sheinker, V. N.; Mitchell, M. B. *J. Phys. Chem. B* **1998**, *102*, 7299.
(103)   Templeton, M. K.; Weinberg, W. H. *J. Am. Chem. Soc.* **1985**, *107*, 7745.
(104)   Guo, X.; Yoshinobu, J.; Yates, J. T. *J. Phys. Chem.* **1990**, *94*, 6839.
(105)   Ratliff, J. S.; Tenney, S. A.; Hu, X.; Conner, S. F.; Ma, S.; Chen, D. A. *Langmuir* **2009**, *25*, 216.
(106)   Chen, J. J.; Jiang, Z. C.; Zhou, Y.; Chakraborty, B. R.; Winograd, N. *Surf. Sci.* **1995**, *328*, 248.
(107)   Gates, S. M.; Russell, J. N.; Yates, J. T. *Surf. Sci.* **1984**, *146*, 199.
(108)   Gates, S. M.; Russell, J. N. J.; Yates, J. T. J. *J. Catal.* **1985**, *95*, 23.
(109)   Parmeter, J. E.; Jiang, X.; Goodman, D. W. *J. Vac. Sci. Technol. A-Vac. Surf. Films* **1991**, *9*, 1810.
(110)   Henderson, M. A.; Jin, T.; White, J. M. *J. Phys. Chem.* **1986**, *90*, 4607.
(111)   Cao, L.; Segal, S. R.; Suib, S. L.; Tang, X.; Satyapal, S. *J. Catal.* **2000**, *194*, 61.
(112)   Smentkowski, V. S.; Hagans, P.; Yates, J. T. *J. Phys. Chem.* **1988**, *92*, 6351.
(113)   Badri, A.; Binet, C.; Lavalley, J. C. *J. Chem. Soc.-Faraday Trans.* **1997**, *93*, 1159.
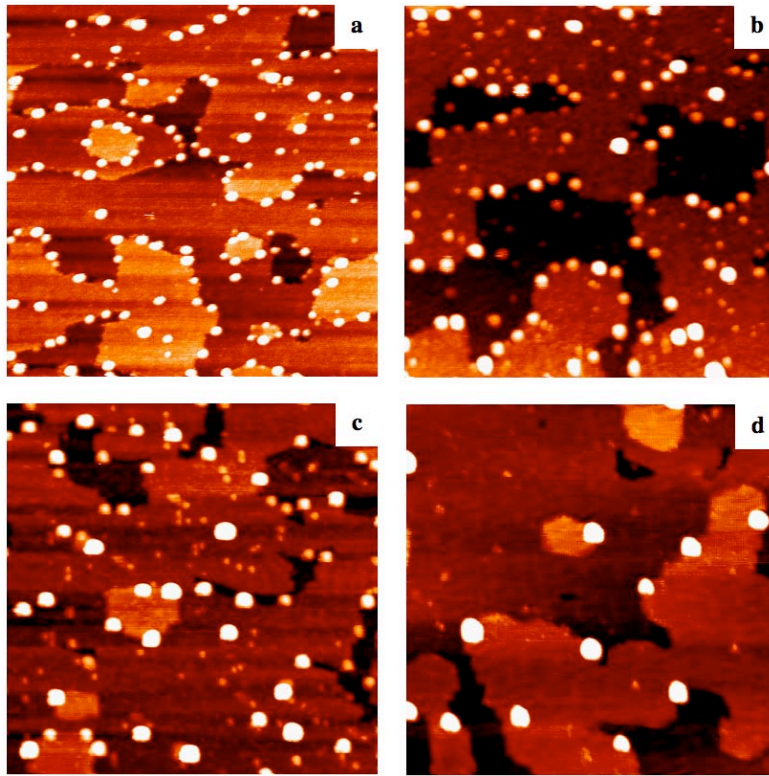
Figure 1: Scanning tunneling microscopy images of 0.10 ML of Au deposited at room temperature after: a) no annealing; and after annealing for one minute at the following temperatures: b) 600 K; c) 800 K; d) 1000 K. All images are 1000 Å×1000 Å.
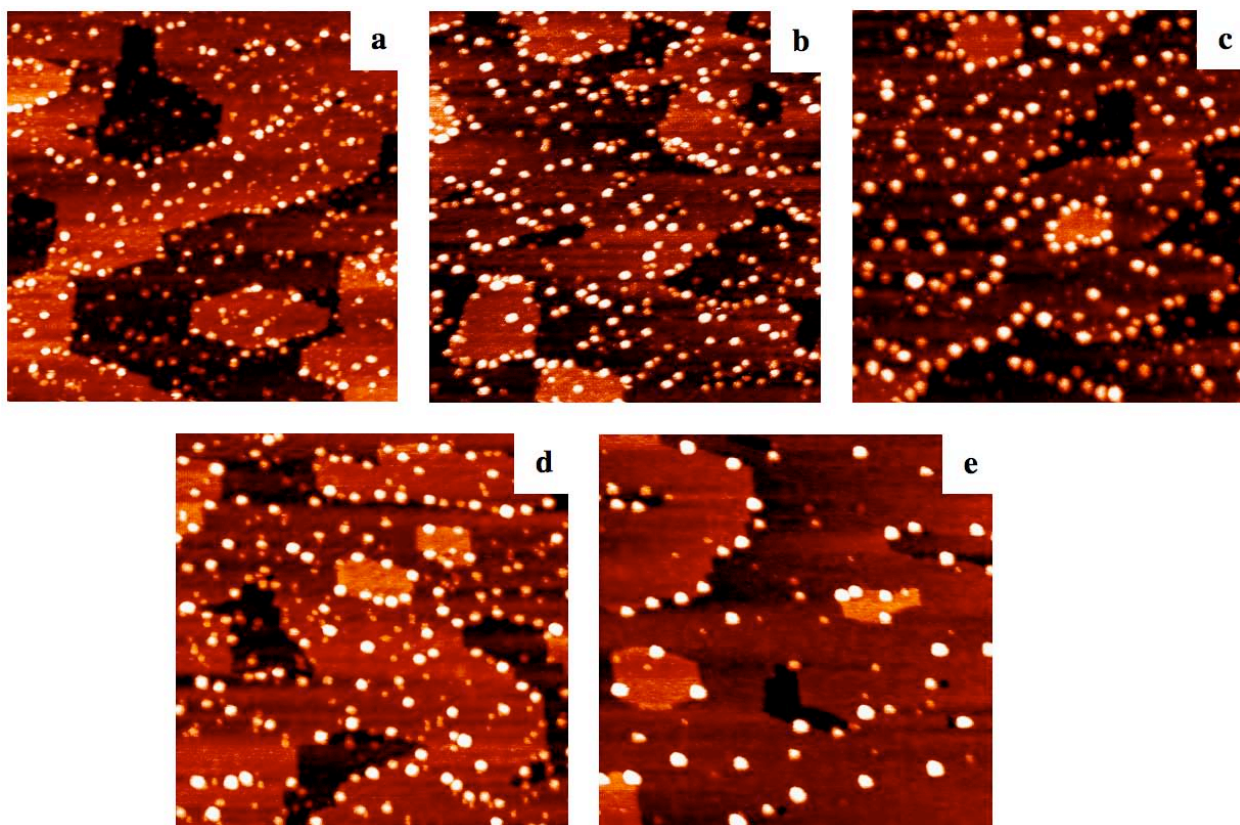
Figure 2: Scanning tunneling microscopy images of: a) 0.024 ML of Pt deposited at room temperature, followed by b) 0.072 ML of Au deposited at room temperature (Pt25%+Au) and annealed at the following temperatures for one minute: c) 600 K; d) 800 K and e) 1000 K. All images are 1000 Å×1000 Å.
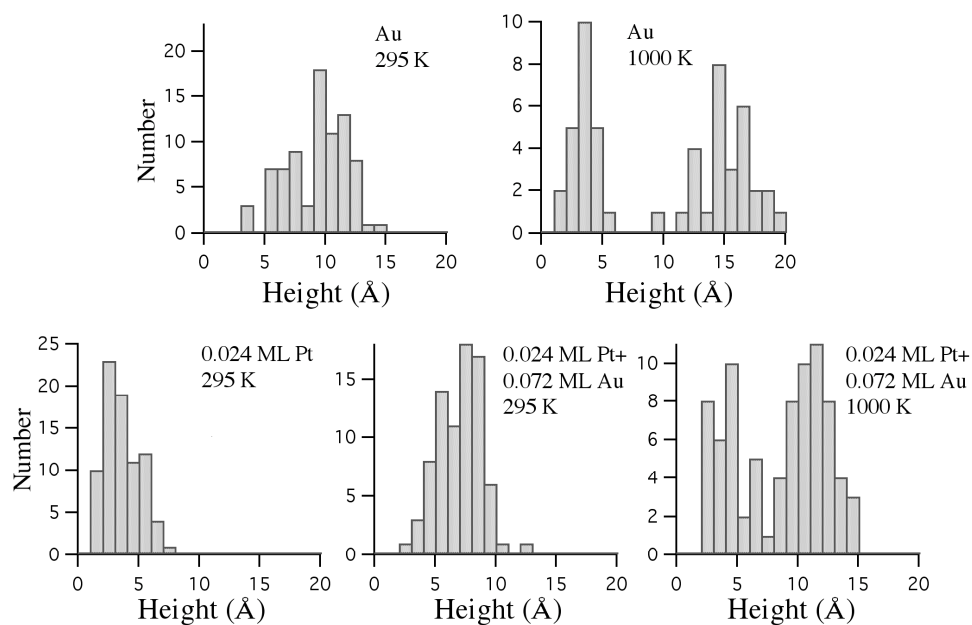
Figure 3: Histograms showing the cluster heights distributions for 0.10 ML of Au and 0.024 ML of Pt +0.072 ML Au (Pt25%+Au) after deposition at room temperature and subsequent annealing at 1000 K for one minute.
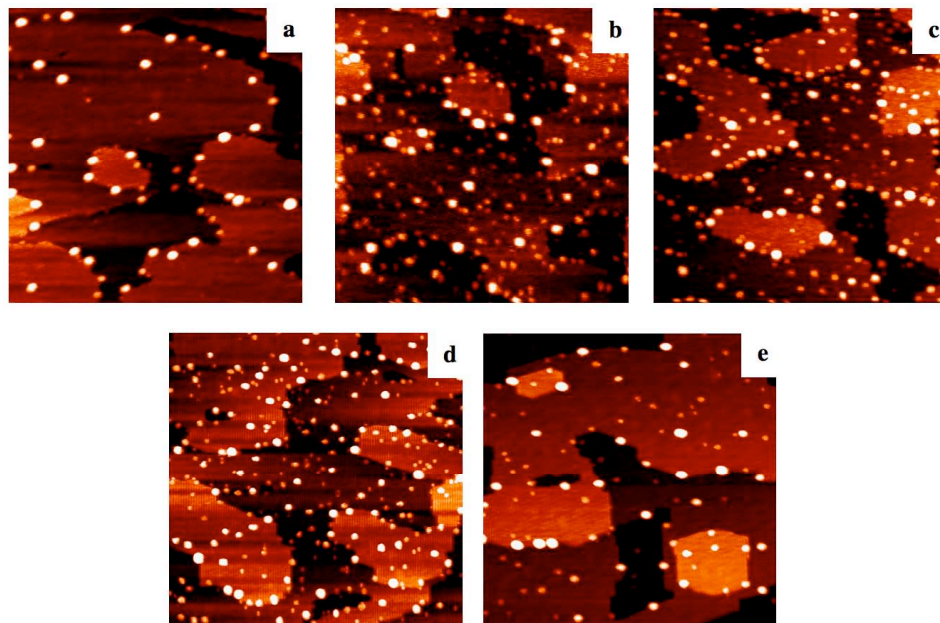
Figure 4: Scanning tunneling microscopy images of: a) 0.072 ML of Au deposited at room temperature, followed by b) 0.024 ML of Pt deposited at room temperature (Au+Pt25%) and annealed at the following temperatures for one minute: c) 600 K; d) 800 K and e) 1000 K. All images are 1000 Å×1000 Å.
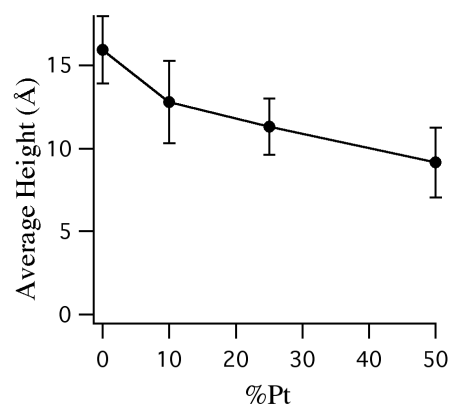
Figure 5: A plot of average cluster height after annealing to 1000 K for one minute as a function of Pt composition for Au-Pt clusters with a total coverage of 0.10 ML deposited by nucleating Au at existing Pt clusters. Average values are based on measurements for a minimum of 15 clusters, and error bars were obtained from the standard deviations.
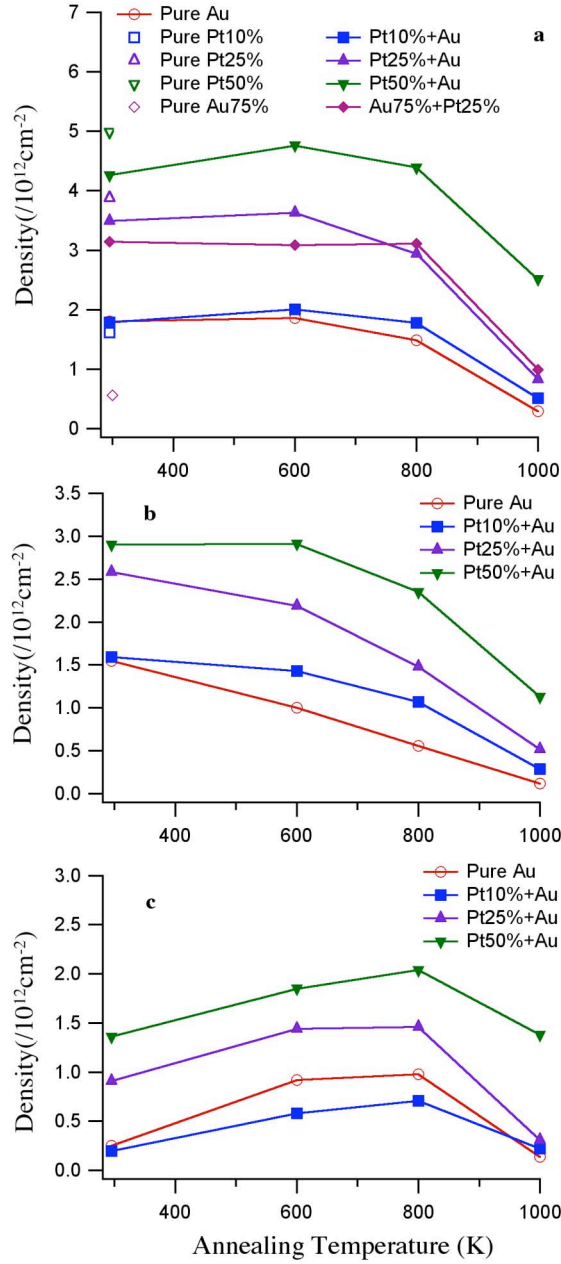
Figure 6: Cluster densities as a function of annealing temperature for: a) all clusters; b) clusters with heights greater than 5 Å; c) clusters with heights less than 5 Å. For all cluster surfaces, the total metal coverage was 0.10 ML. The filled symbols represent the densities for bimetallic clusters while the unfilled symbols represent surfaces before deposition of the second metal.
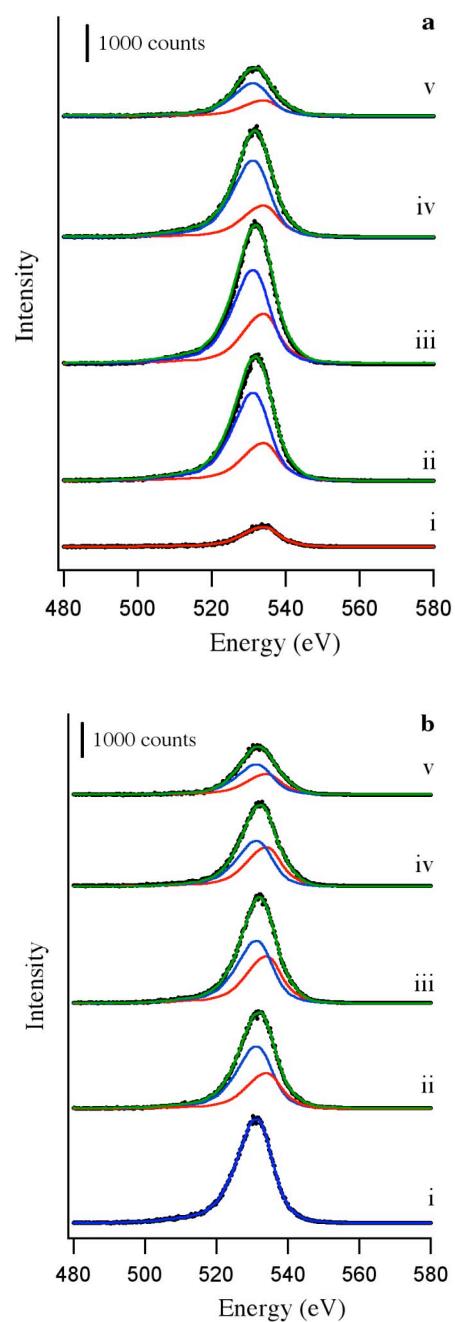
Figure 7: Low energy ion scattering data for the room temperature deposition of: a) 0.024 ML of Pt followed by 0.072 ML of Au (Pt25%+Au); and b) 0.072 ML of Au followed by 0.024 ML Pt (Au+Pt25%). Spectra are acquired: i) after the deposition of the first metal; ii) after deposition of the second metal; and after annealing to various temperatures for one minute: iii) 600 K; iv) 800 K and v) 1000 K.
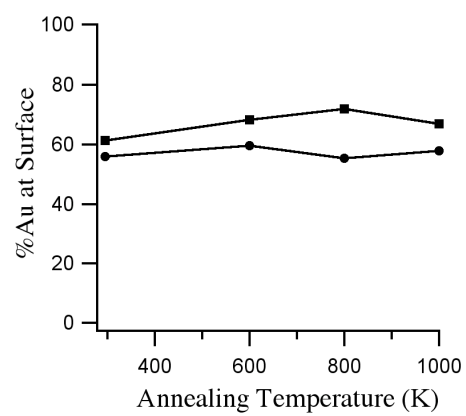
Figure 8: The surface composition Au as a function of annealing temperature in Au-Pt clusters formed from the deposition of 0.024 ML of Pt followed by 0.072 ML of Au (Pt25%+Au, squares), and 0.072 ML of Au followed by 0.024 ML of Pt (Au+Pt25%, circles).
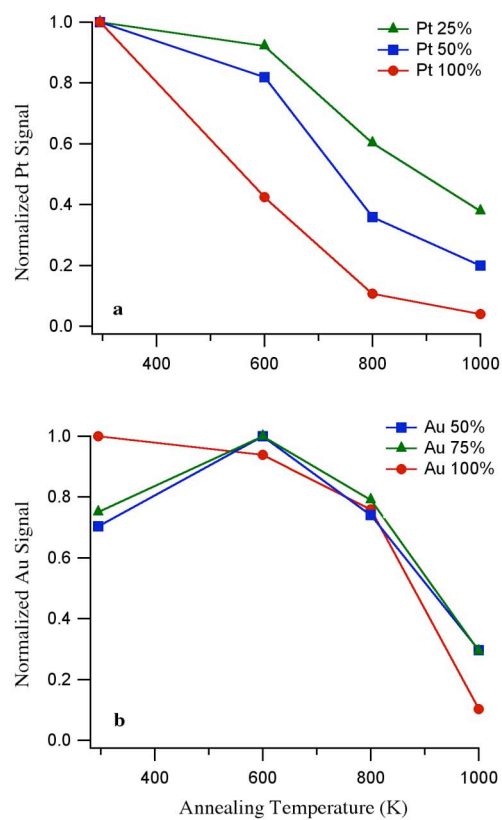
Figure 9: Low energy ion scattering signals as a function of annealing temperature for pure clusters, Pt25%+Au and Pt50%+Au: a) Pt signal contribution; and b) Au signal contribution.
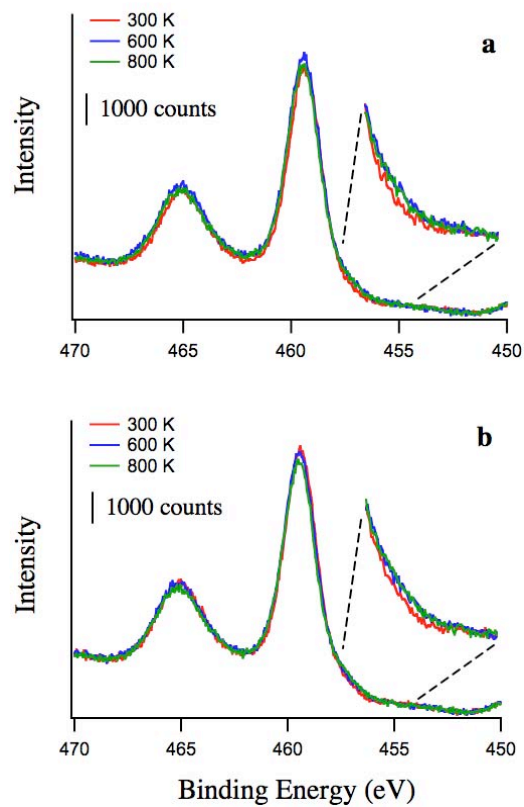
Figure 10: Grazing angle XPS data of the Ti(2p) region for: a) 0.024 ML of Pt followed by 0.072 ML of Au (Pt25%+Au); and b) 0.024 ML of Pt; deposited at room temperature and annealed at 600 K and 800 K for one minute each.
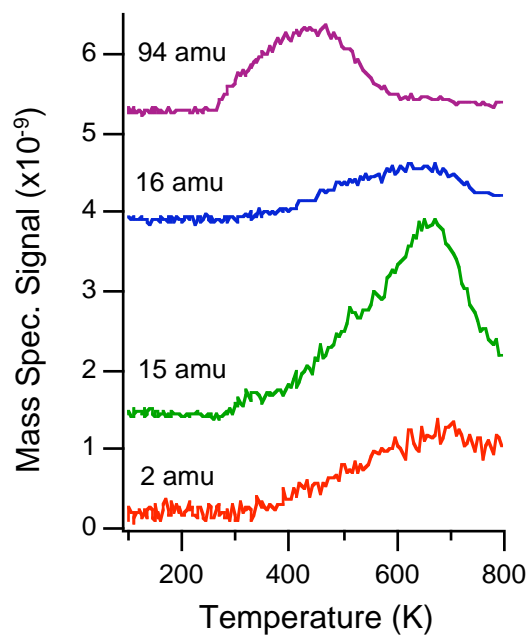
Figure 11: Temperature programmed desorption data for DMMP on TiO$_2$(110) adsorbed at room temperature and heated at 2 K/s for the following masses: a) hydrogen (2 amu); b) methyl (15 amu); c) methane (16 amu) and d) DMMP (94 amu). The 15 amu signal for methyl was corrected for the cracking contributions from methane and DMMP.
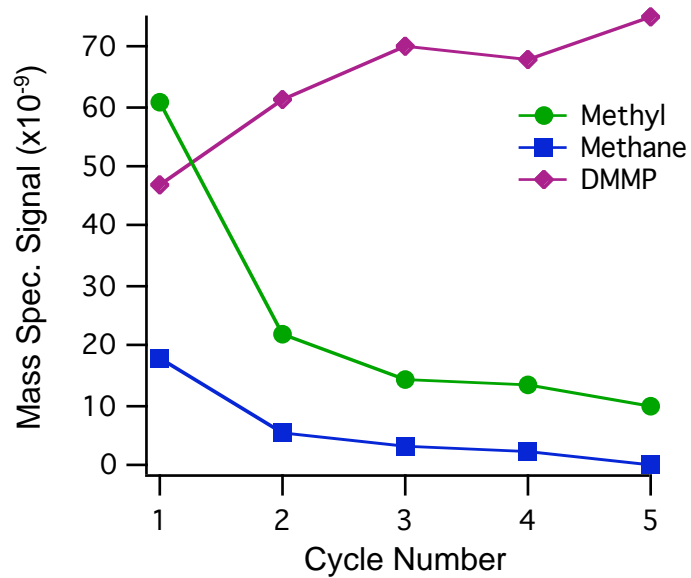
Figure 12: A plot of integrated mass spectrometer signals for methyl (15 amu), methane (16 amu) and DMMP (94 amu) for successive temperature programmed desorption experiments on TiO$_2$(110). For each cycle, DMMP was adsorbed at room temperature and heated to 800 K at 2 K/s. The TiO$_2$ surface was cleaned by ion sputtering only before the first cycle. The 15 amu signal for methyl was corrected for the cracking contributions from DMMP and methane.
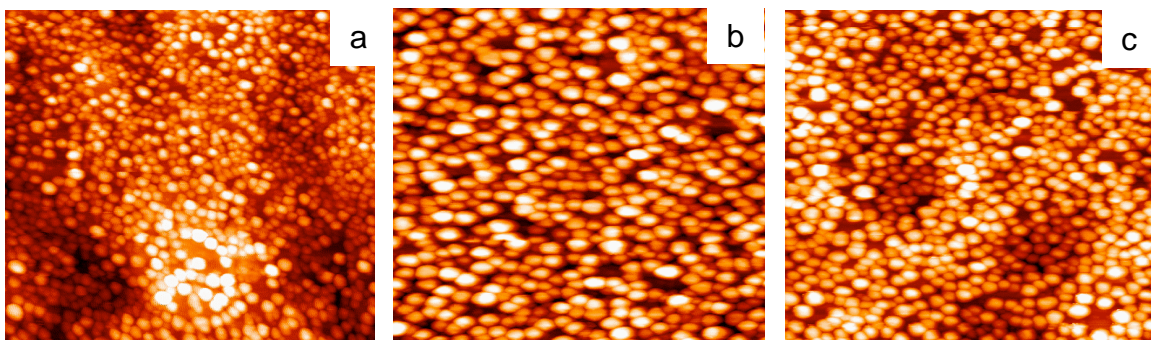
Figure 13: Scanning tunneling microscopy images for the following metals deposited at room temperature on TiO$_2$(110): a) 0.5 ML of Pt; b) 0.5 ML of Au; and c) 0.25 ML Pt followed by 0.25 ML of Au (Pt+Au). All images are 1000 Å ×1000 Å.
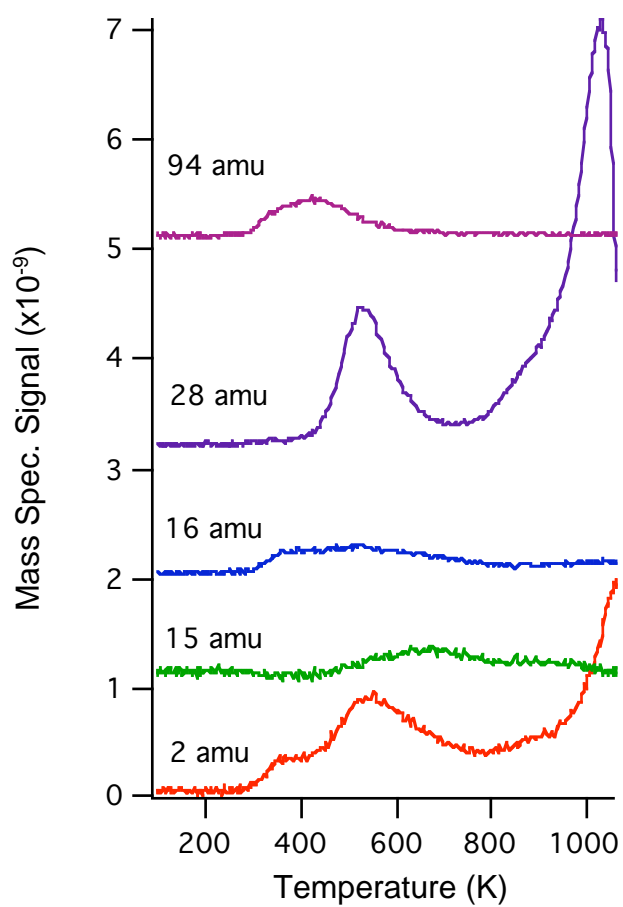
Figure 14: Temperature programmed desorption data for DMMP adsorbed on 0.5 ML of Pt and heated at 2 K/s for the following masses: a) hydrogen (2 amu); b) methyl (15 amu); methane (16 amu); CO (28 amu); and DMMP (94 amu). The 15 amu signal for methyl was corrected for the cracking contributions from DMMP and methane.
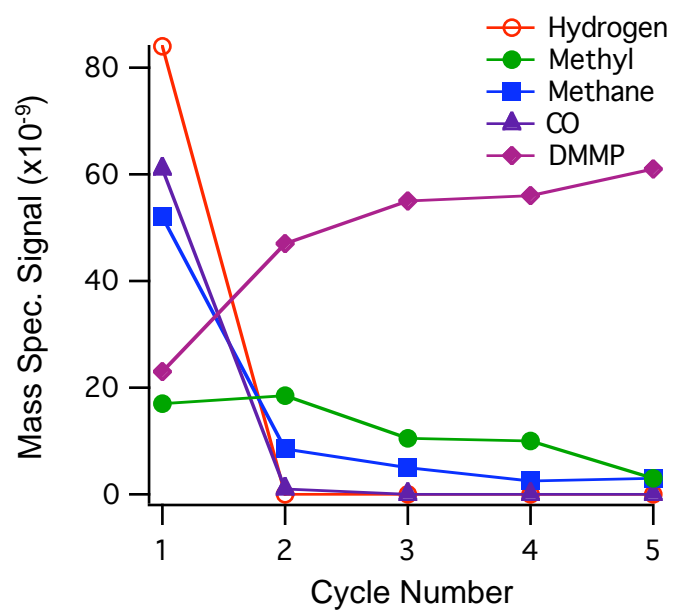
Figure 15: A plot of the integrated mass spectrometer signals for successive temperature programmed desorption experiments of DMMP on 0.5 ML of Pt. For each cycle, DMMP was adsorbed at room temperature and heated to 800 K at 2 K/s. The surface was not cleaned between adsorption-reaction experiments.
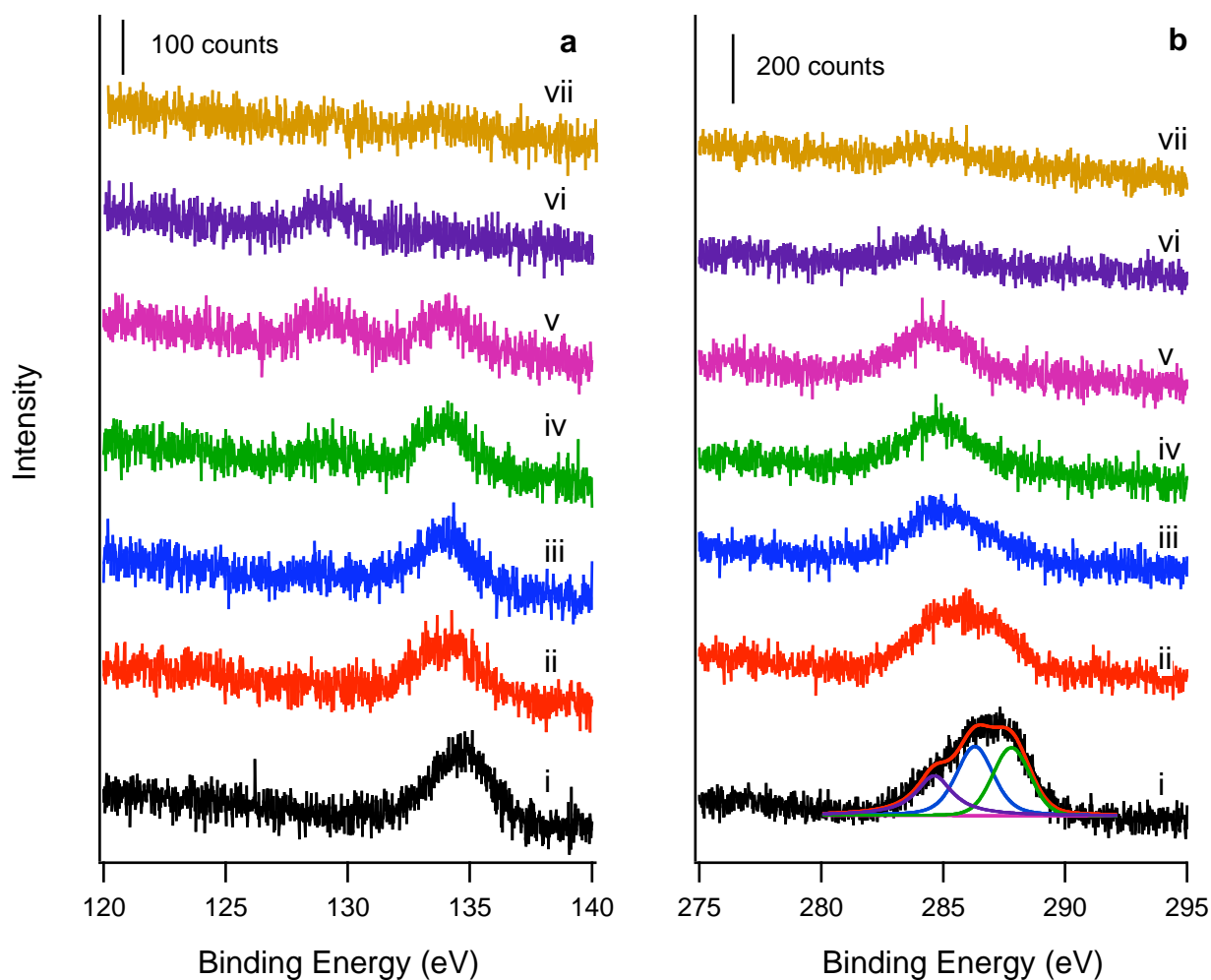
Figure 16: X-ray photoelectron spectroscopy data for the a) P(2p) and b) C(1s) regions for DMMP adsorbed on 0.5 ML of Pt at room temperature and heated to the following temperatures at 2 K/s: i) no heating; ii) 400 K; iii) 500 K; iv) 600 K; v) 800 K; vi) 1000 K; and vii) after exposure to 1×10^{-7} Torr O_2 at 600 K for 5 minutes.
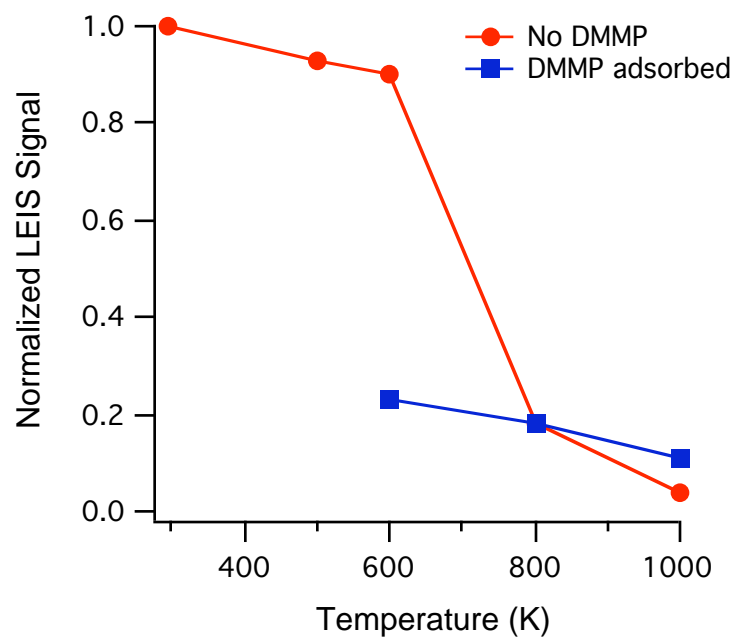
Figure 18: Integrated Pt low energy ion scattering signals as a function of temperature for pure 0.5 ML of Pt clusters (circles) and a saturation dose of DMMP on 0.5 ML Pt clusters (squares). Heating ramps were 2 K/s.
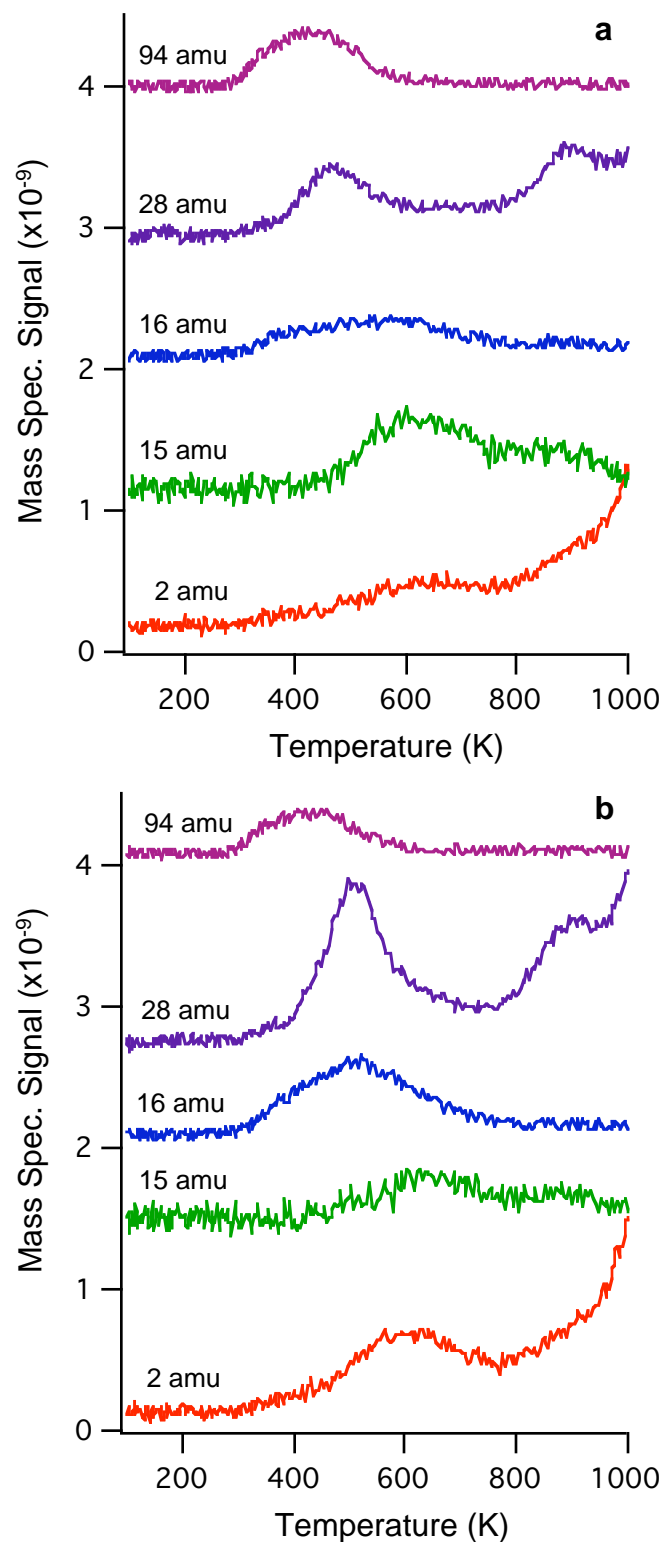
Figure 17: Temperature programmed desorption data for DMMP adsorbed at room temperature on a) 0.5 ML of Au; and b) 0.25 ML of Pt+0.25 ML of Au (Pt+Au) for the following masses: i) hydrogen (2 amu); ii) methyl (25 amu); iii) methane (16 amu); CO (28 amu); and DMMP (94 amu). The methyl signals at 15 amu were corrected for cracking contributions of methane and DMMP, and heating ramps were 2 K/s.
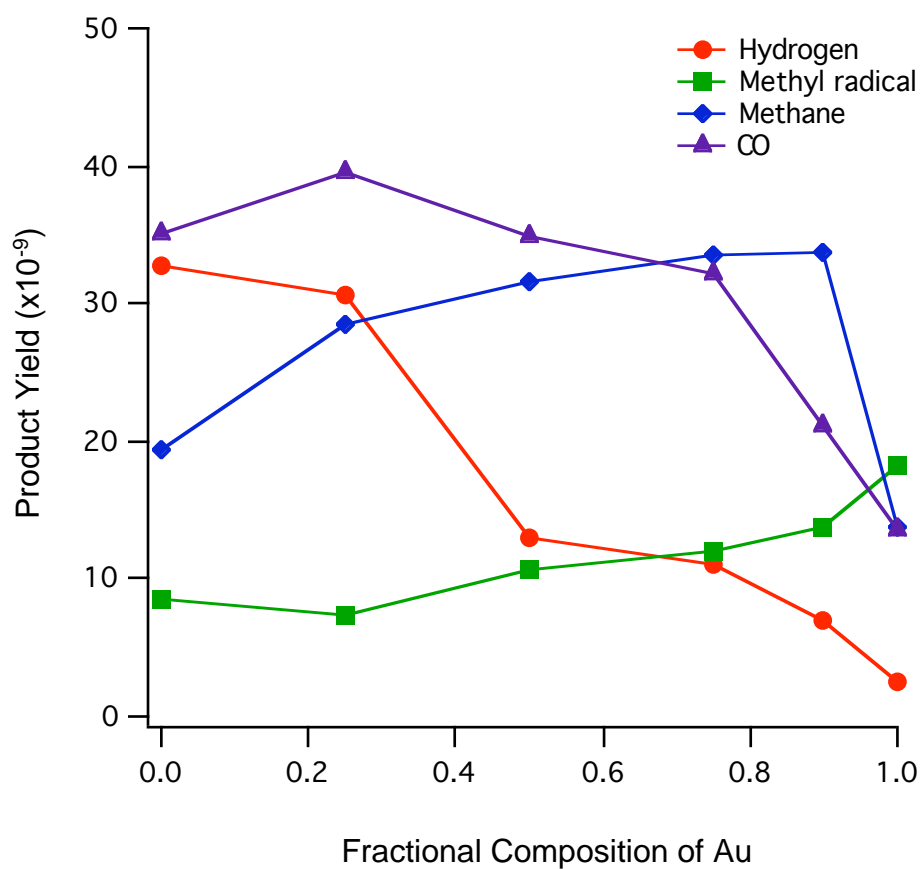
Figure 19: Product yields from TPD experiments for DMMP adsorbed on pure and bimetallic clusters as a function of changing composition. In all cases, the total metal coverage was 0.5 ML and Pt deposition was followed by Au deposition. DMMP was adsorbed at 100 K, and the surface was heated to 200 K before the TPD experiments.
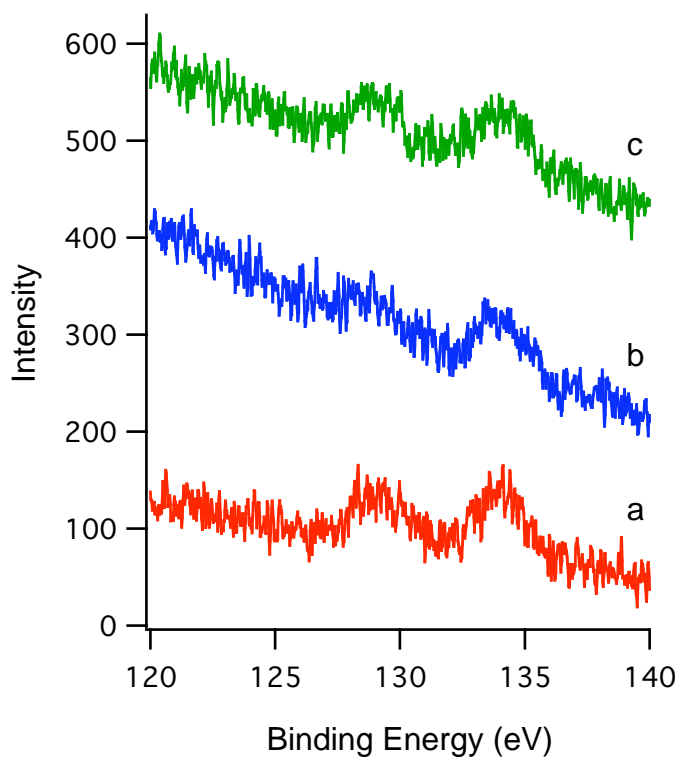
Figure 20: The P(2p) region in X-ray photoelectron spectroscopy data for DMMP adsorbed at room temperature and heated to 800 K at 2 K/s on: a) 0.5 ML of Pt; b) 0.5 ML of Au; and c) 0.25 ML of Pt+0.25 ML of Au (Pt+Au).
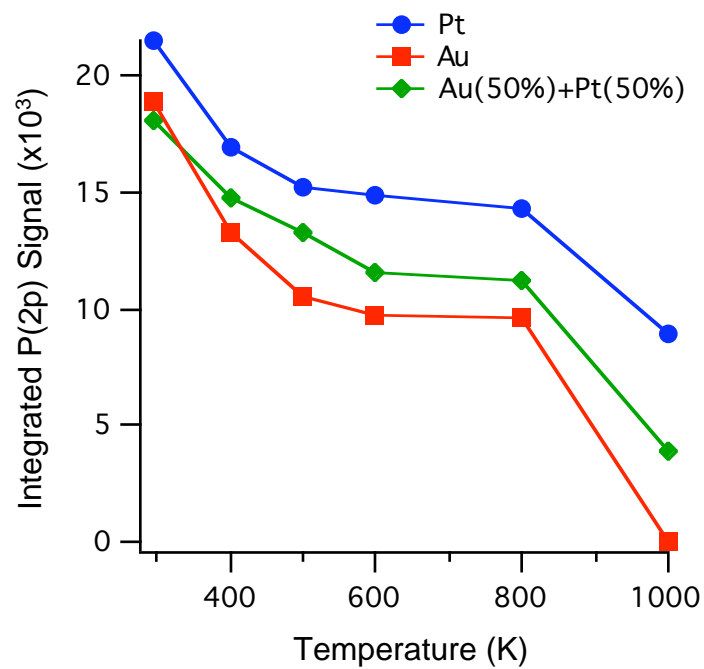
Figure 21: A plot of the integrated P(2p) signal for DMMP adsorbed at room temperature and heated to various temperatures on 0.5 ML Pt clusters; 0.5 ML Au clusters; and 0.25 ML Pt+0.25 ML Au (Pt+Au) clusters.
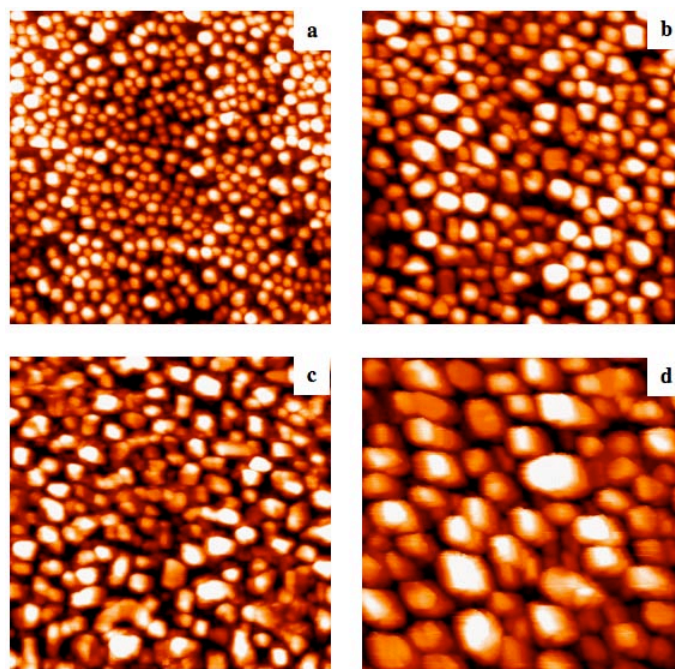
Figure 22: Scanning tunneling microscopy images for the following coverage of Ni deposited on TiO2(110) at room temperature: a) 1 ML; b) 2.5 ML; c) 5 ML and d) 5 ML annealed to 850 K.

.
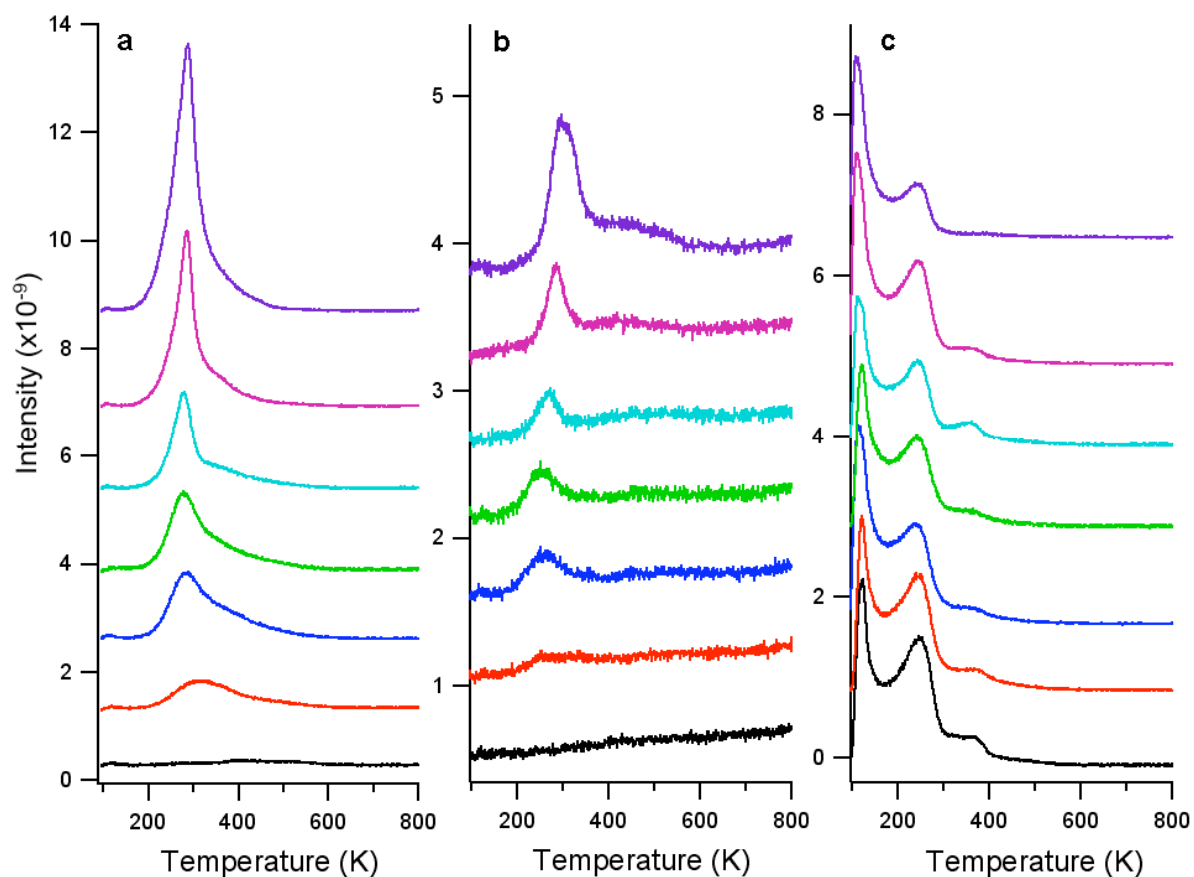
Figure 23: Temperature programmed desorption data for the: a) methane (16 amu); b) hydrogen (2 amu) and c) methanethiol (47 amu) signals; from a saturation exposure of methanethiol dosed at 100 K on the following surfaces: i) oxidized TiO_2(110); ii) 0.1 ML Ni; iii) 0.25 ML Ni; iv) 0.5 ML Ni; v) 1 ML Ni; vi) 2.5 ML Ni; and vii) 5 ML Ni on oxidized TiO_2(110). Temperature ramps were 2 K/s
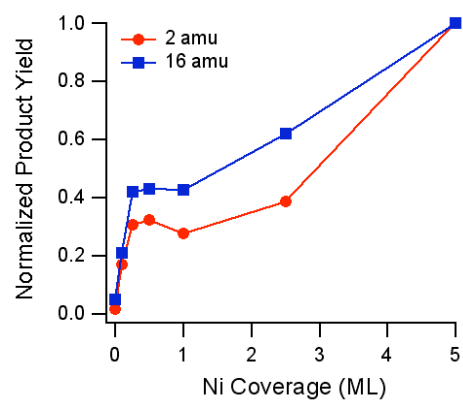
Figure 24: Normalized product yields for hydrogen and methane as a function of Ni coverage.
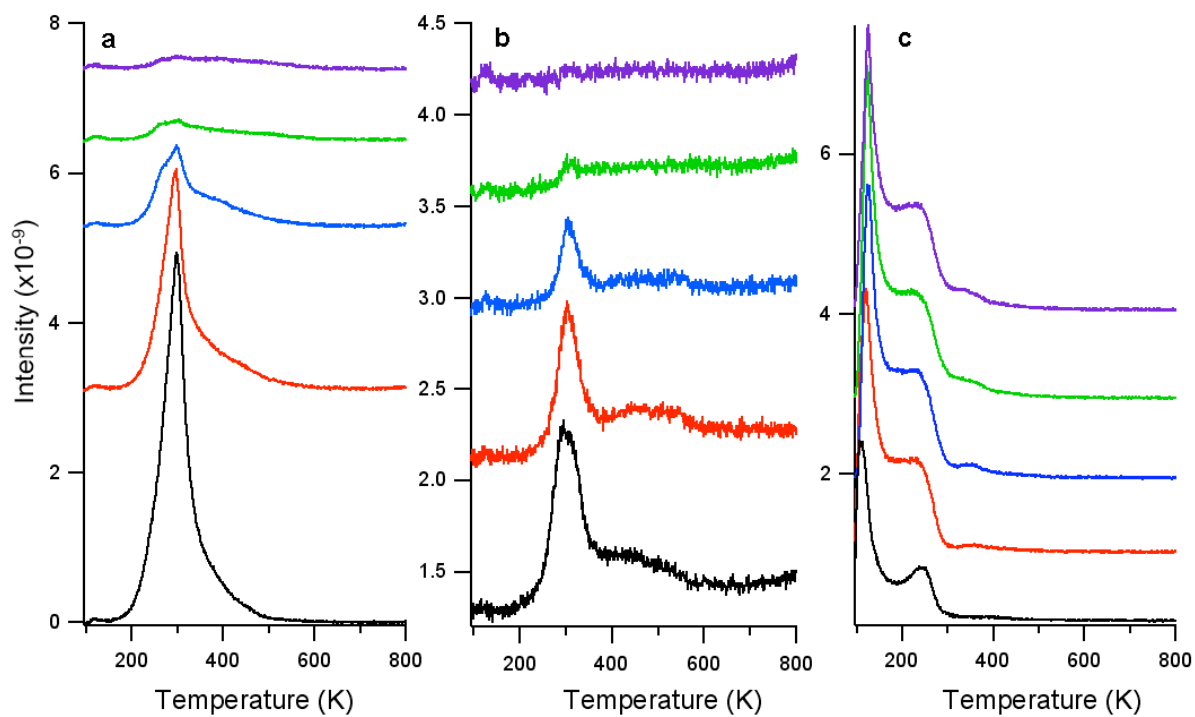
Figure 25: Temperature programmed desorption data for the: a) methane (16 amu); b) hydrogen (2 amu) and c) methanethiol (47 amu) signals; from a saturation exposure of methanethiol dosed at 100 K on the 5 ML Ni clusters on oxidized $TiO_2(110)$ heated to the following temperatures: i) 700 K; ii) 750 K; iii) 800 K; and iv) 850 K. Temperature ramps were 2 K/s.
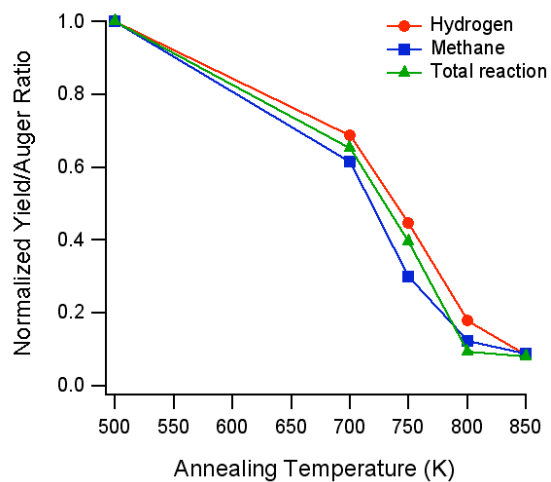
Figure 26: Normalized product yields of methane and hydrogen and total reaction for a saturation dose of methanethiol on the 5 ML Ni clusters on $TiO_2(110)$ as a function of annealing the clusters to various temperatures before exposure to methanethiol. The total reaction was determined from the S:Ti Auger ratio after TPD to 930 K.
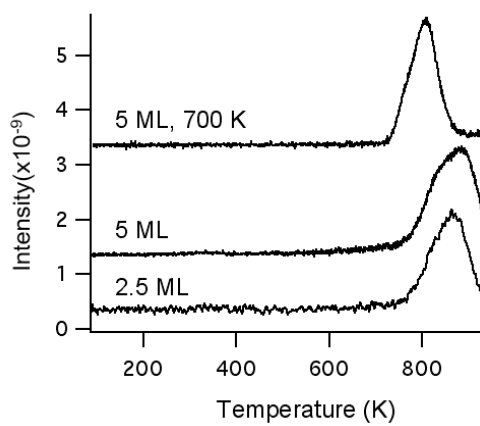
Figure 27: Temperature programmed desorption data for $C^{18}O$ desorption (30 amu) from a saturation exposure of methanethiol dosed at 100 K on the following surfaces (bottom to top): 2.5 ML of Ni; 5 ML of Ni; and 5 ML of Ni heated to 750 K; on oxidized $TiO_2(110)$. Temperature ramps were 2 K/s.
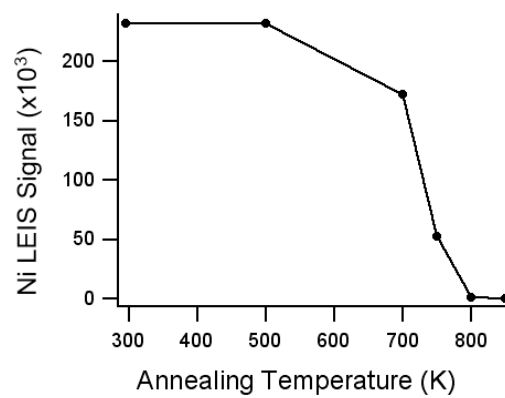
Figure 28: The Ni low energy ion scattering signal for 5 ML Ni clusters on $TiO_2(110)$ as a function on annealing temperature.
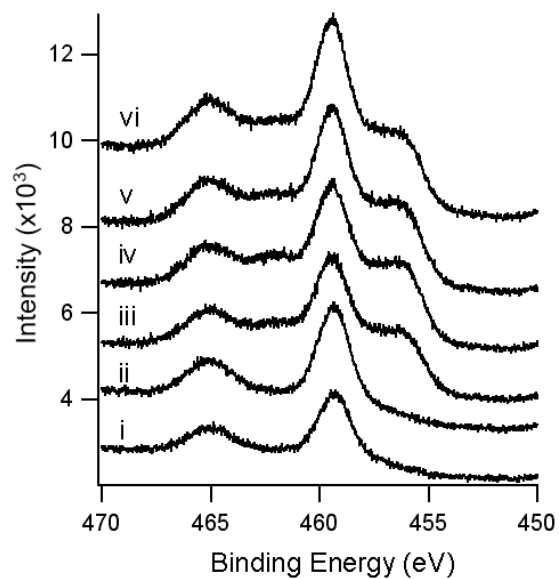
Figure 29: Grazing angle X-ray photoelectron spectroscopy data of the Ti(2p) region for 5 ML Ni clusters on TiO_2(110) at: i) room temperature; and after annealing to: ii) 500 K; iii) 700 K; iv) 750 K; v) 800 K; and vi) 850 K.
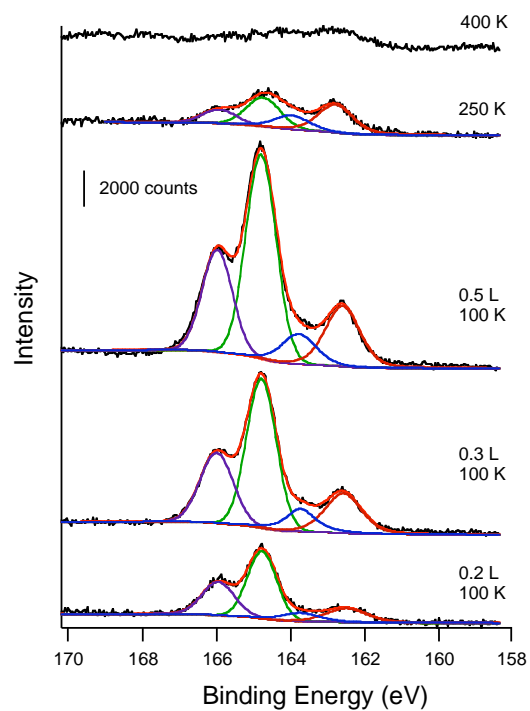
Figure 30: High resolution X-ray photoelectron spectroscopy data for the S(2p) region for methanethiol adsorbed at 100 K on oxidized $TiO_2(110)$ at various exposures, and for a 0.5 L exposure heated to 250 K and 400 K.
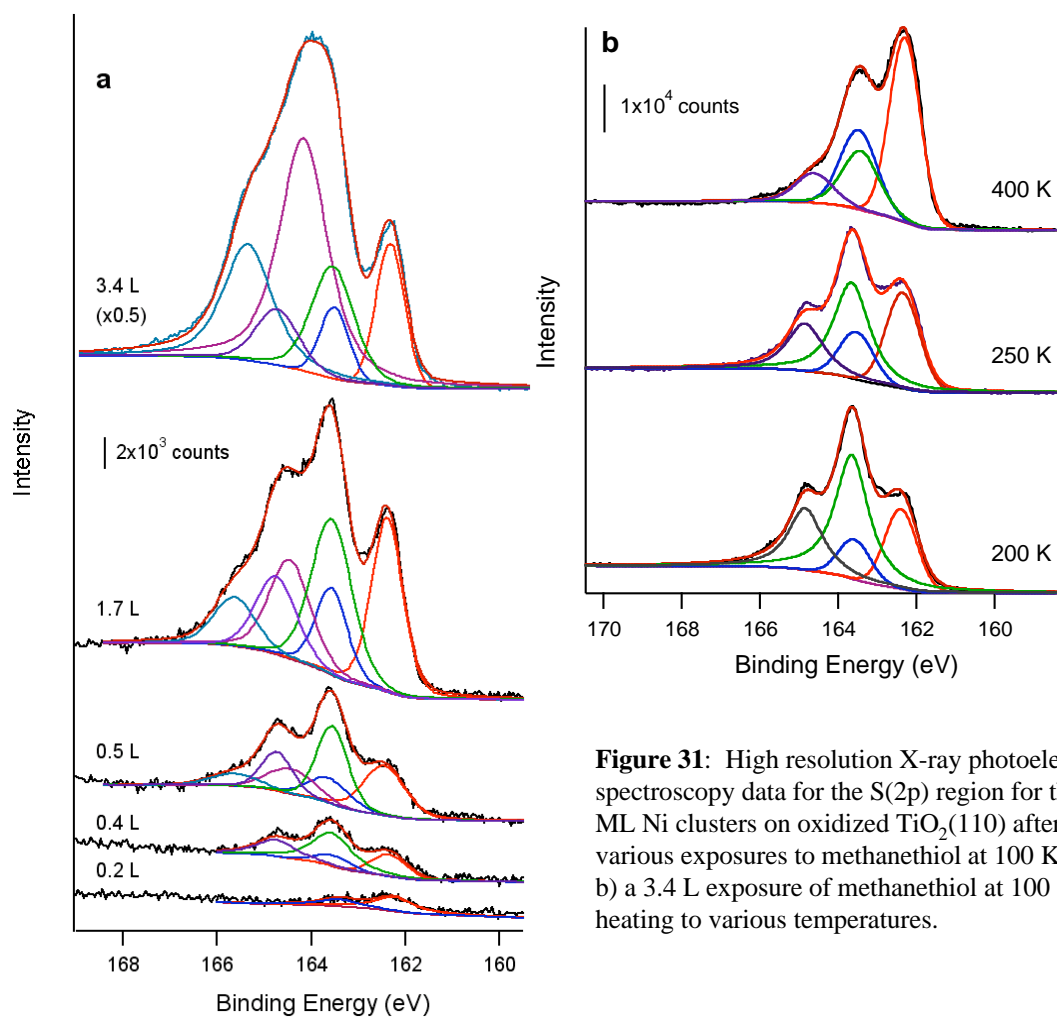
Figure 31: High resolution X-ray photoelectron spectroscopy data for the S(2p) region for the 5 ML Ni clusters on oxidized $TiO_2(110)$ after: a) various exposures to methanethiol at 100 K; and b) a 3.4 L exposure of methanethiol at 100 K after heating to various temperatures.
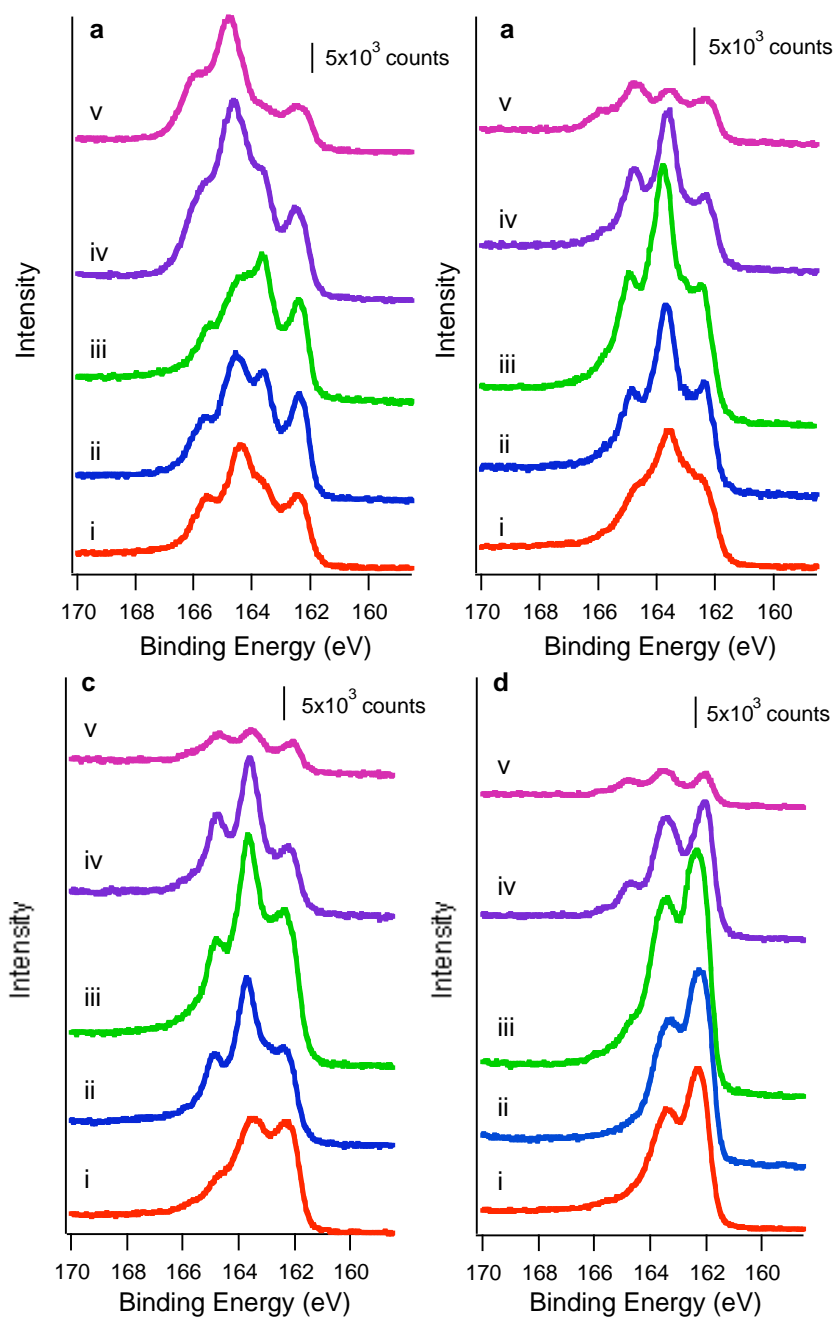
Figure 32: High resolution X-ray photoelectron spectroscopy data for the S(2p) region for a saturation exposure of methanethiol dosed on Ni clusters and annealed Ni clusters at: a) 100 K; b) 200 K; c) 250 K; and d) 400 K for the following surfaces: i) 1 ML of Ni; ii) 2.5 ML of Ni; iii) 5 ML of Ni; iv) 5 ML of Ni heated to 750 K; v) 5 ML of Ni heated to 800 K; on $TiO_2(110)$.
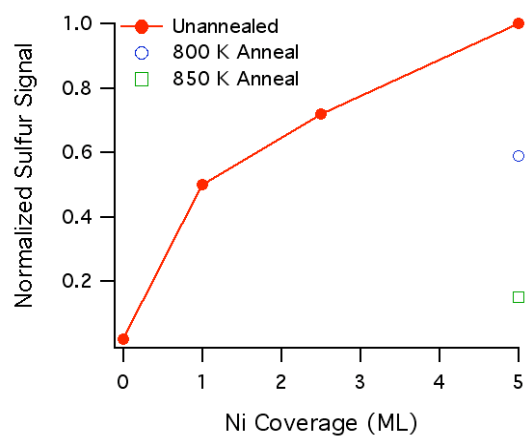
Figure 33: Normalized total reaction for methanethiol on the Ni clusters as a function of increasing Ni coverage (solid circles). Data points are also shown for the 5 ML Ni clusters annealed to 800 K and 850 K before exposure to methanethiol. The total reaction was determined from the integrated S(2p) signal after methanethiol exposure at 100 K and heating to 600 K.
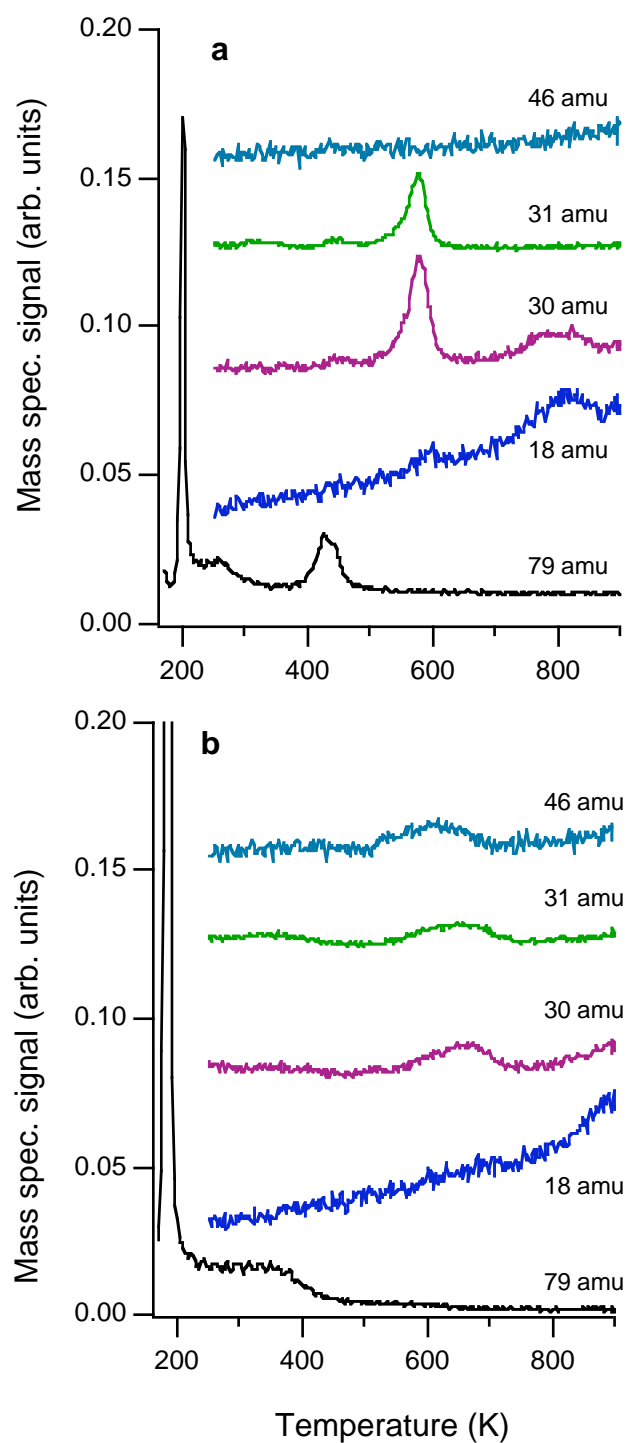
Figure 34: Temperature programmed desorption data for a saturation dose of DMMP on stoichiometric ceria during: a) the first adsorption-reaction cycle; and b) the fourth adsorption-reaction cycle. The heating rate of 2 K/s.
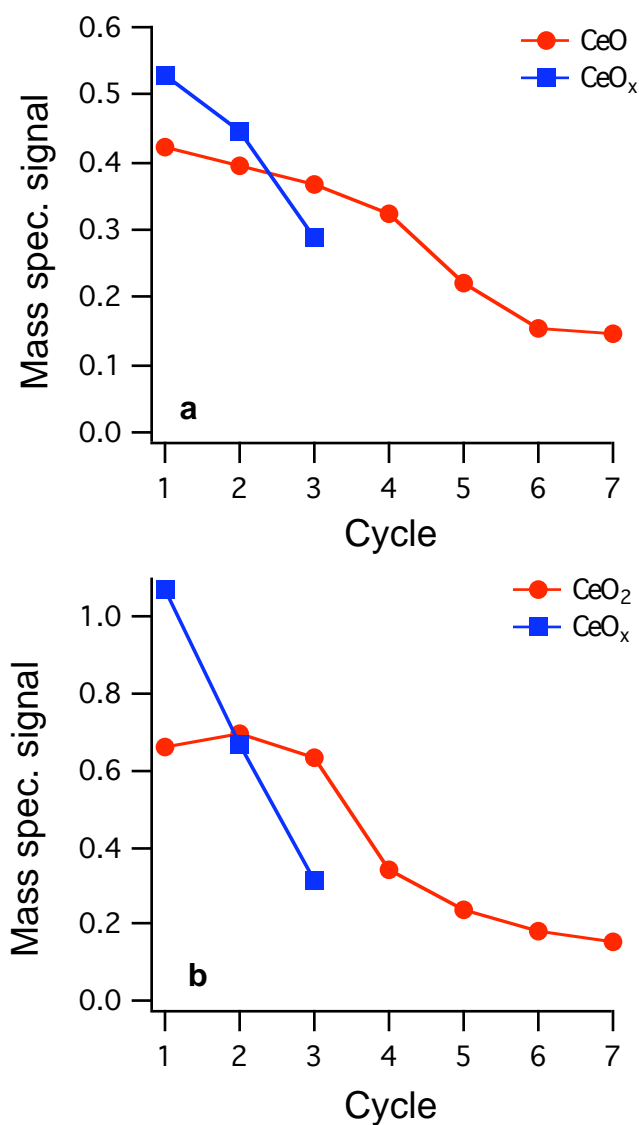
Figure 35: Product yields for formaldehyde (30 amu), methanol (31 amu) formation at 575 K, based on integrated areas in the TPD spectrum, as a function of adsorption-reaction cycle. Data for the stoichiometric and reduced surfaces are shown as circle and squares, respectively. The 30 amu signals were not corrected for the cracking contribution of methanol, which accounts for ~10% of the total 30 amu signal on all surfaces.
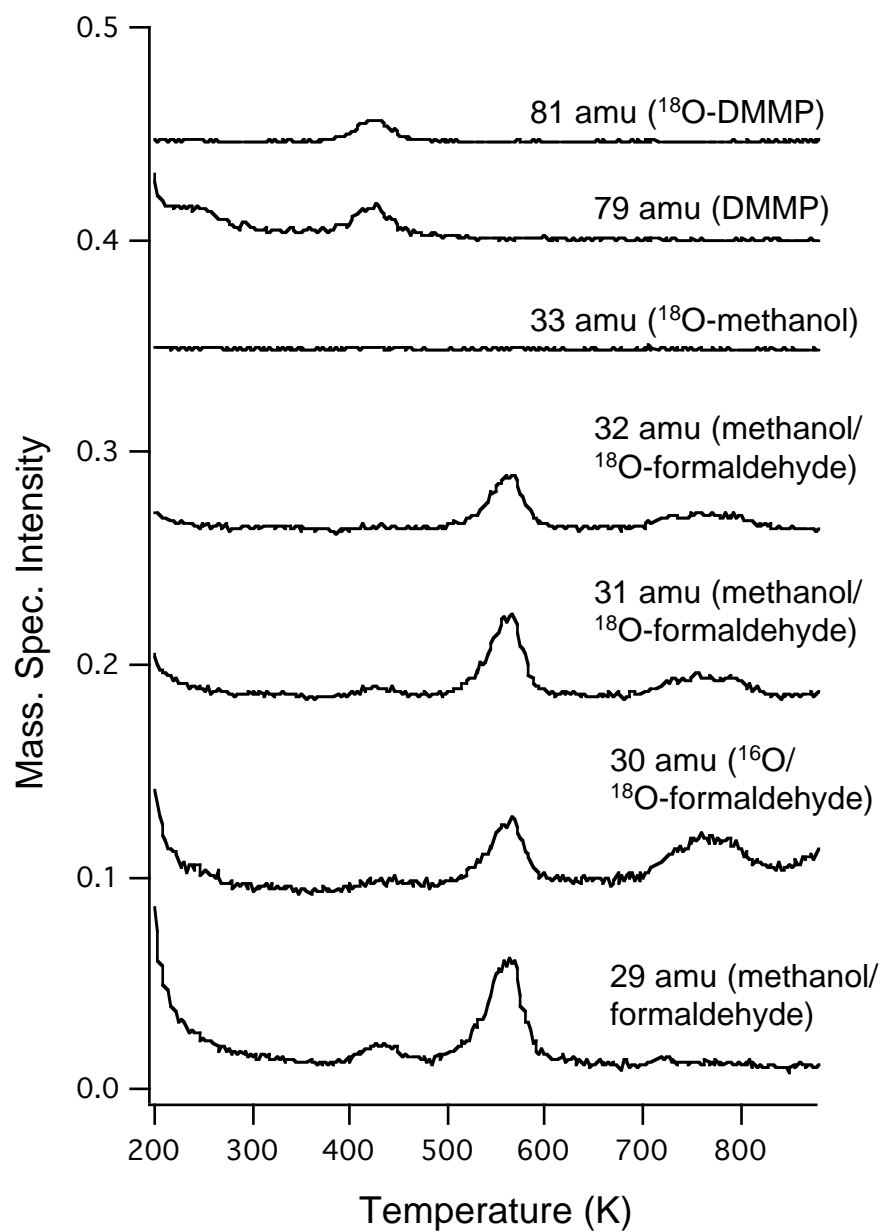
Figure 36: Temperature programmed desorption data for a saturation exposure of DMMP on $Ce^{18}O_2$. The heating rate was 2 K/s.
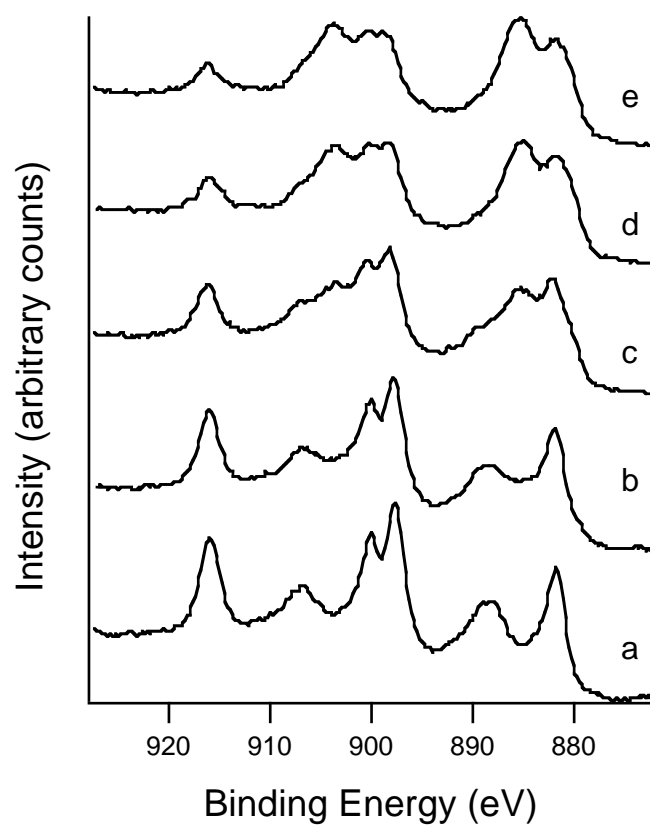
Figure 37: X-ray photoelectron spectroscopy data for the Ce(3d) region for: a) the stoichiometric ceria film before DMMP reaction; b) after one adsorption-reaction cycle; c) after two adsorption-reaction cycles; d) after three adsorption-reaction cycles; and e) after four adsorption-reaction cycles with DMMP.
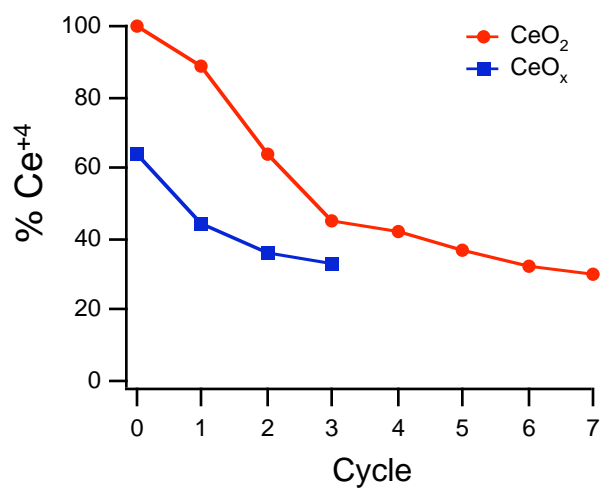
Figure 38: Ce^{+4} content as a function of DMMP adsorption-reaction cycle as determined by XPS. The red circles are for the initially stoichiometric CeO_2 film and the blue squares are for the intially reduced CeO_x film.
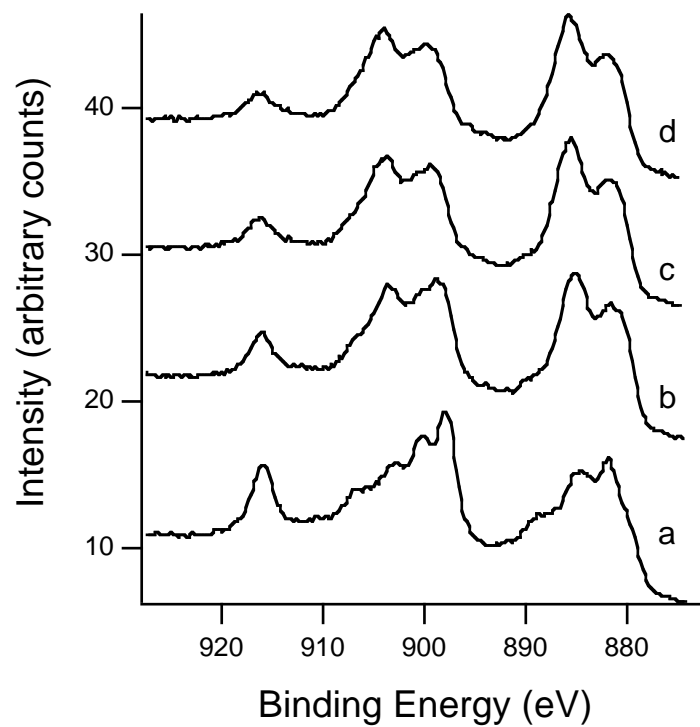
Figure 39: X-ray photoelectron spectroscopy data for the Ce(3d) region for: a) the reduced ceria surface before DMMP reaction; b) after one adsorption-reaction cycle; c) after two adsorption-reaction cycles; and d) after three adsorption-reaction cycles with DMMP.
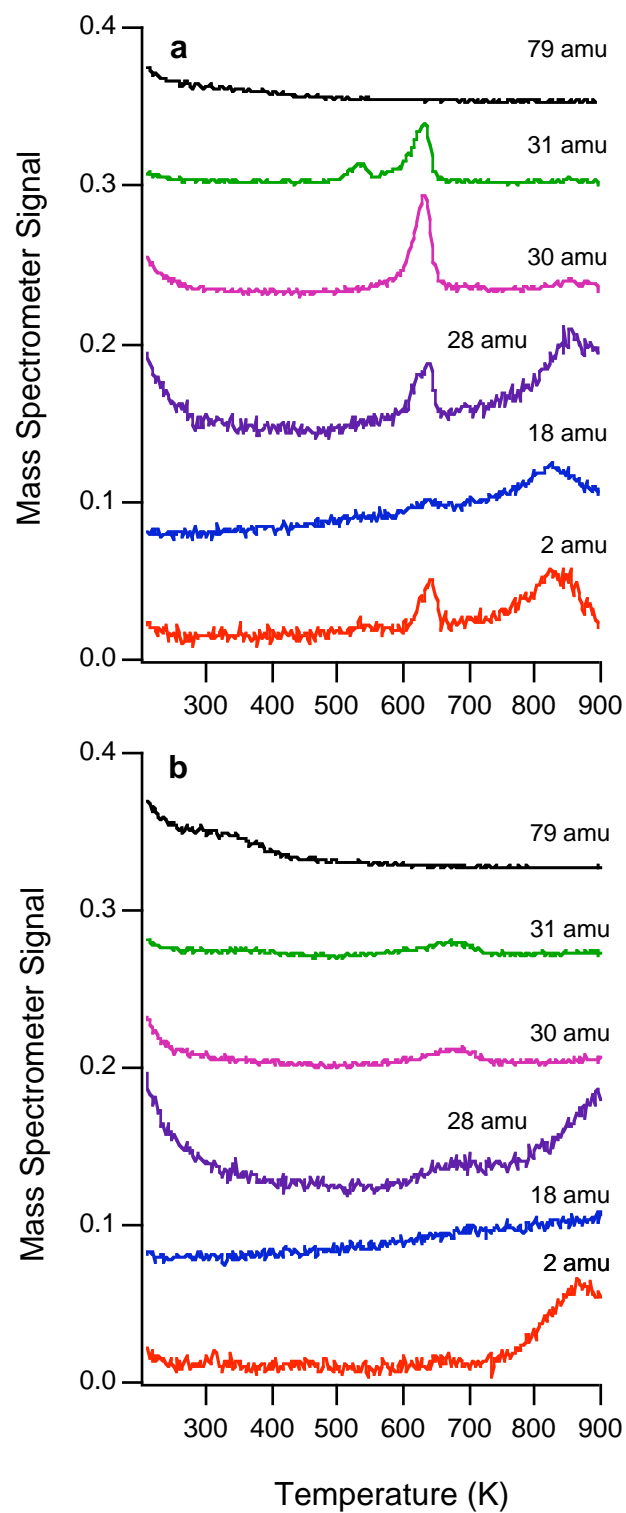
Figure 40: Temperature programmed desorption data for a saturation dose of DMMP on reduced ceria for: a) the first adsorption-reaction cycle; and b) the second adsorption-reaction cycle. The heating rate was 2 K/s.
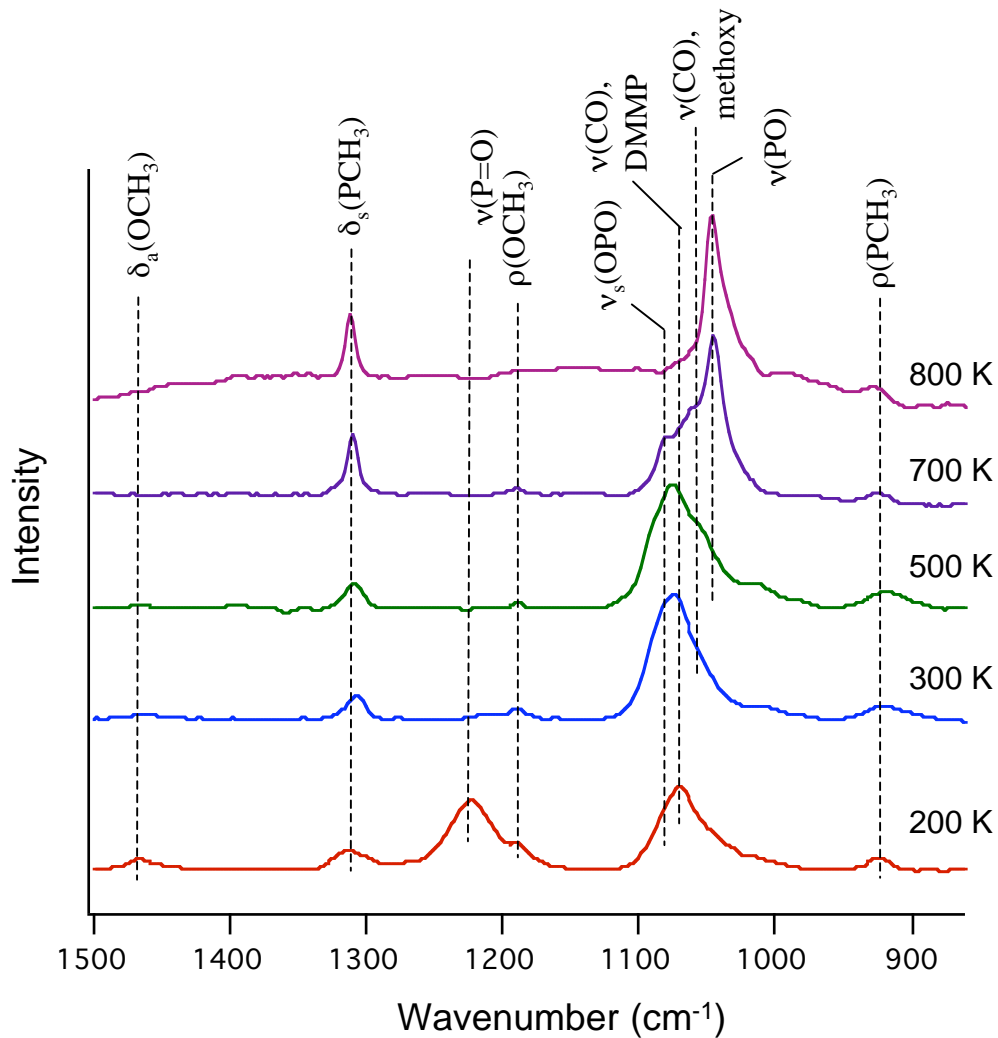
Figure 41a: Infrared reflection-absorption spectroscopy data for a saturation dose of DMMP adsorbed at 100 K and heated to various temperatures on stoichiometric ceria (CeO_2) at: i) 200 K; ii) 300 K; iii) 400 K; iv) 500 K; and v) 700 K. Heating rates were approximately 1 K/s.
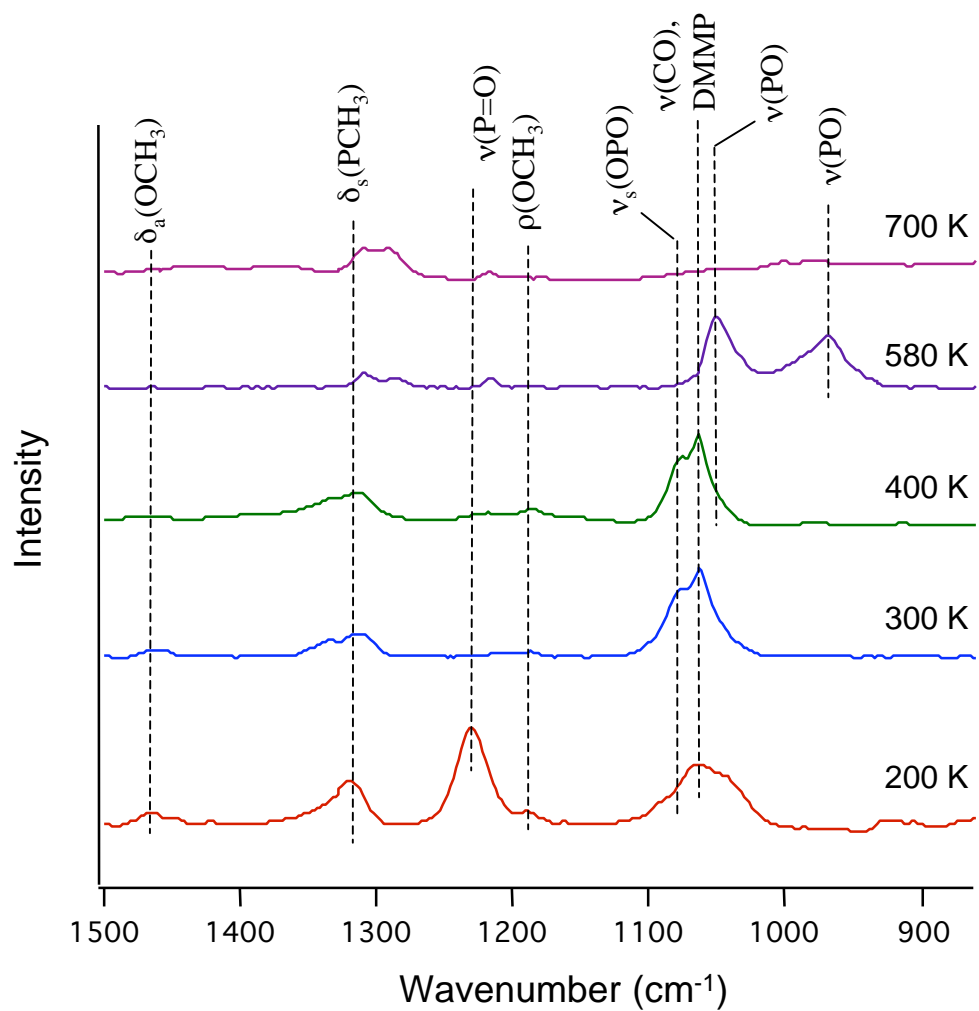
Figure 41b: Infrared reflection-absorption spectroscopy data for a saturation dose of DMMP adsorbed at 100 K and heated to various temperatures on reduced ceria (CeO$_x$) at: i) 200 K; ii) 300 K; iii) 400 K; iv) 580 K; and v) 700 K. Heating rates were approximately 1 K/s.
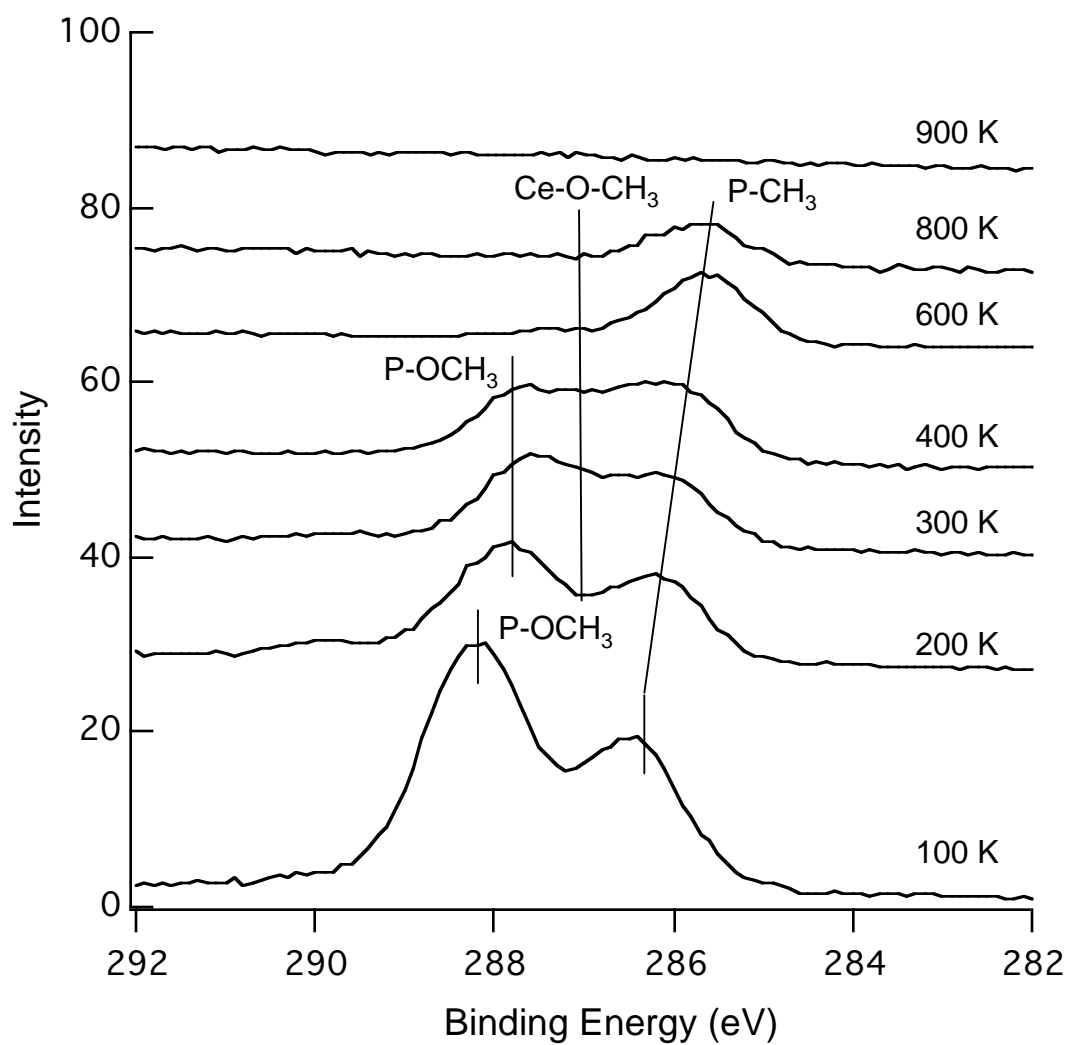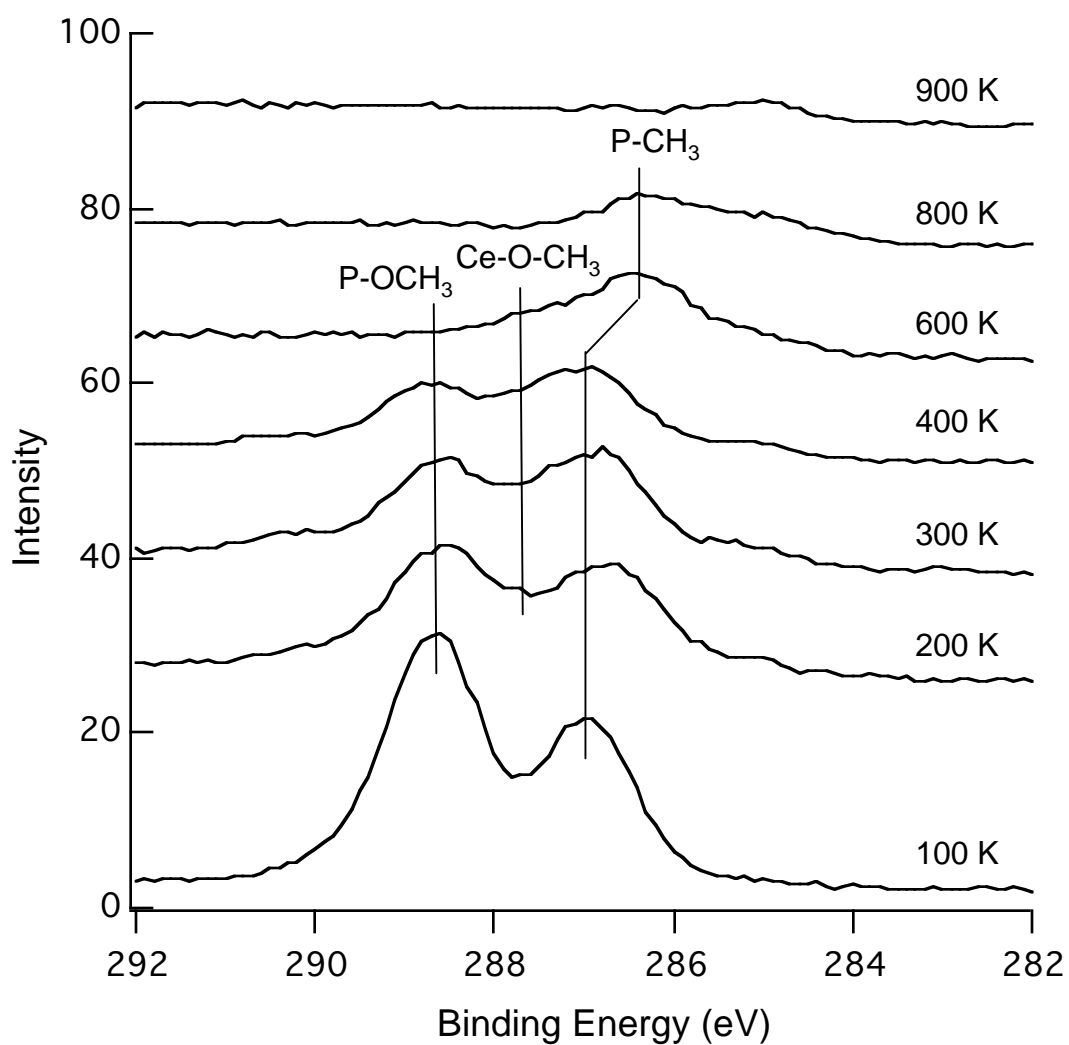
Figure 42: Soft X-ray photoelectron spectroscopy data for the C(1s) region for 10 L of DMMP on stoichiometric ceria at 100 K and then annealed as indicated. Spectra were collected with a 400 eV beam energy.
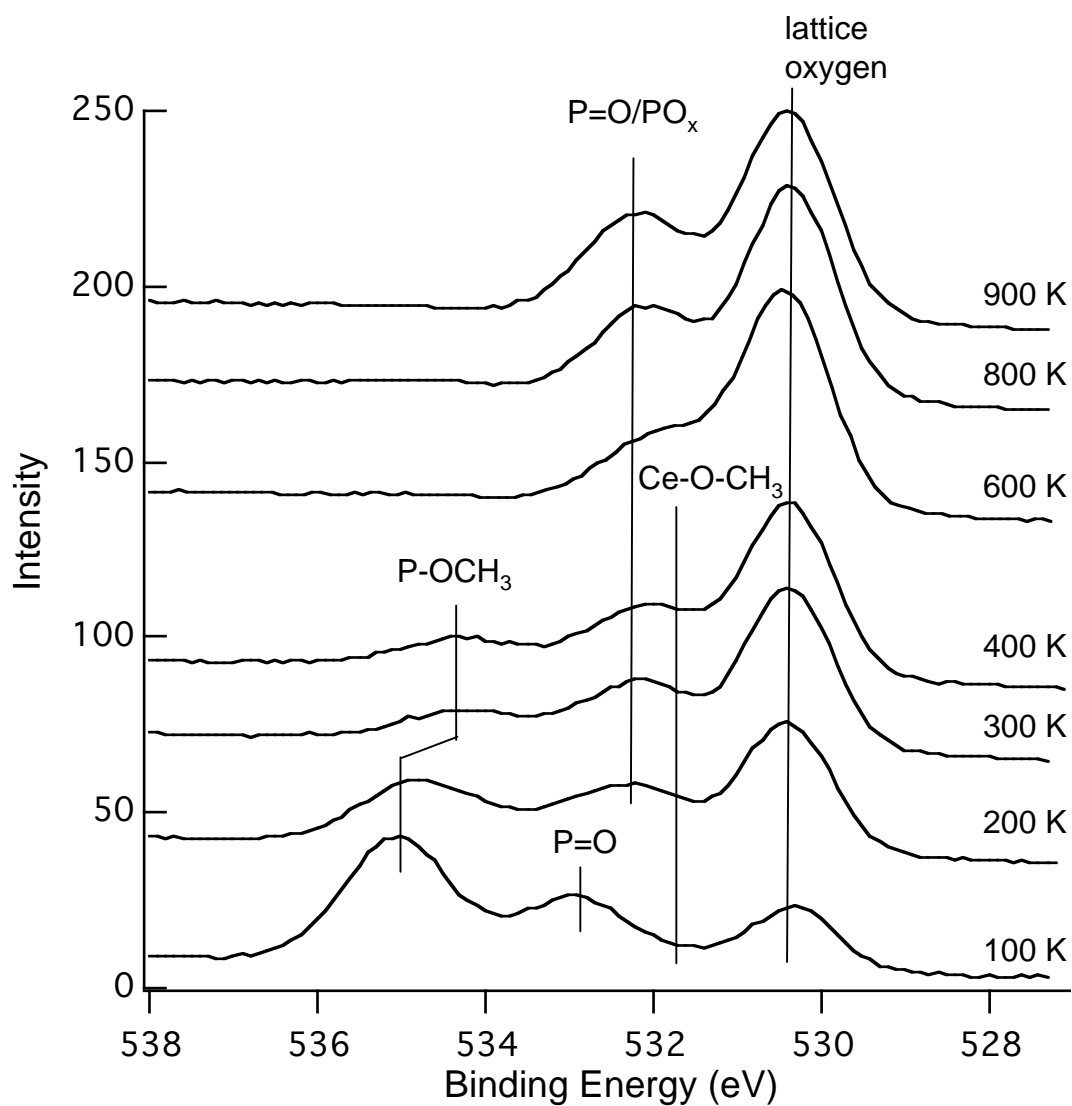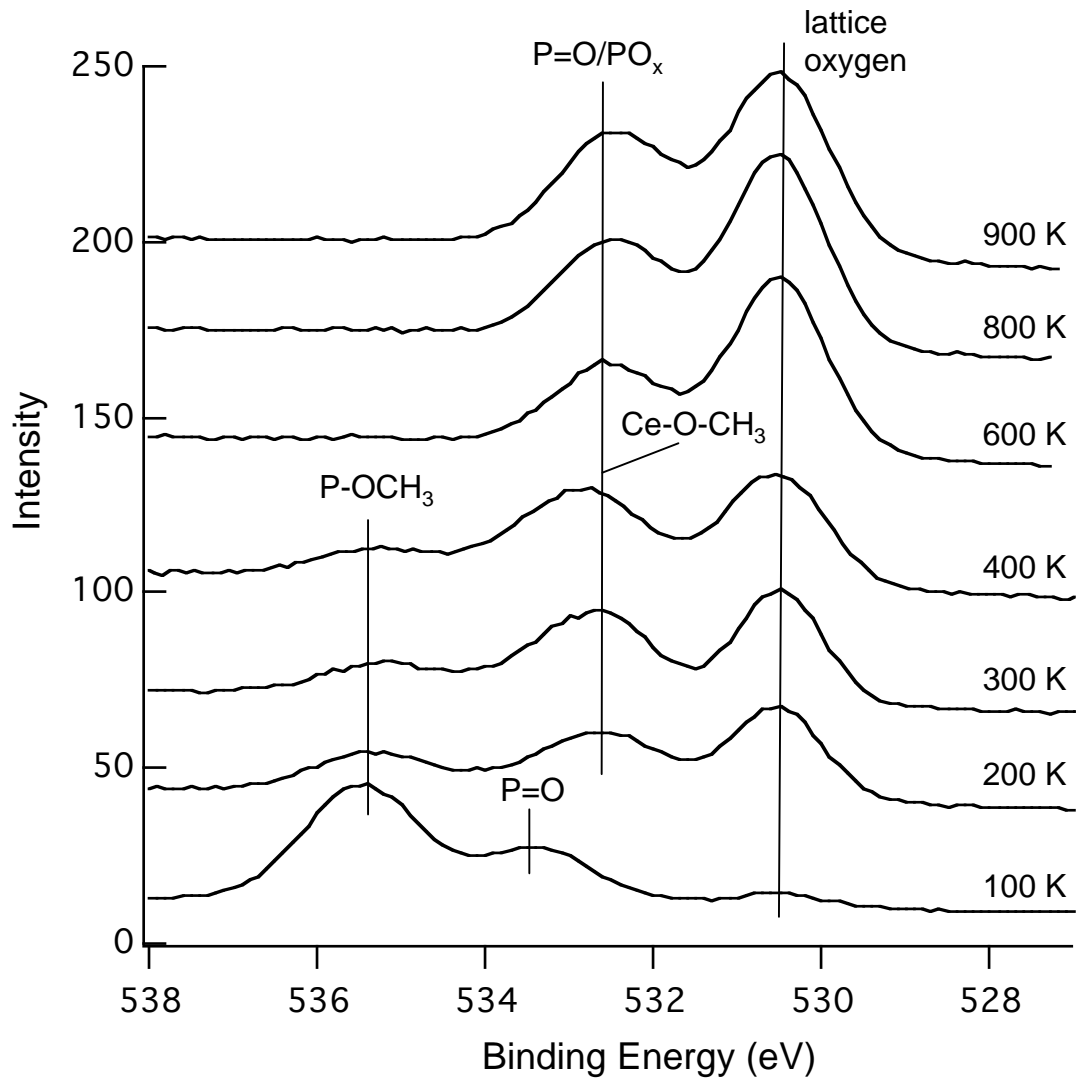
Figure 43: Soft X-ray photoelectron spectroscopy data for the O(1s) region for a 10 L of DMMP on stoichiometric ceria at 100 K and then annealed as indicated. Spectra were collected with a 600 eV beam energy.
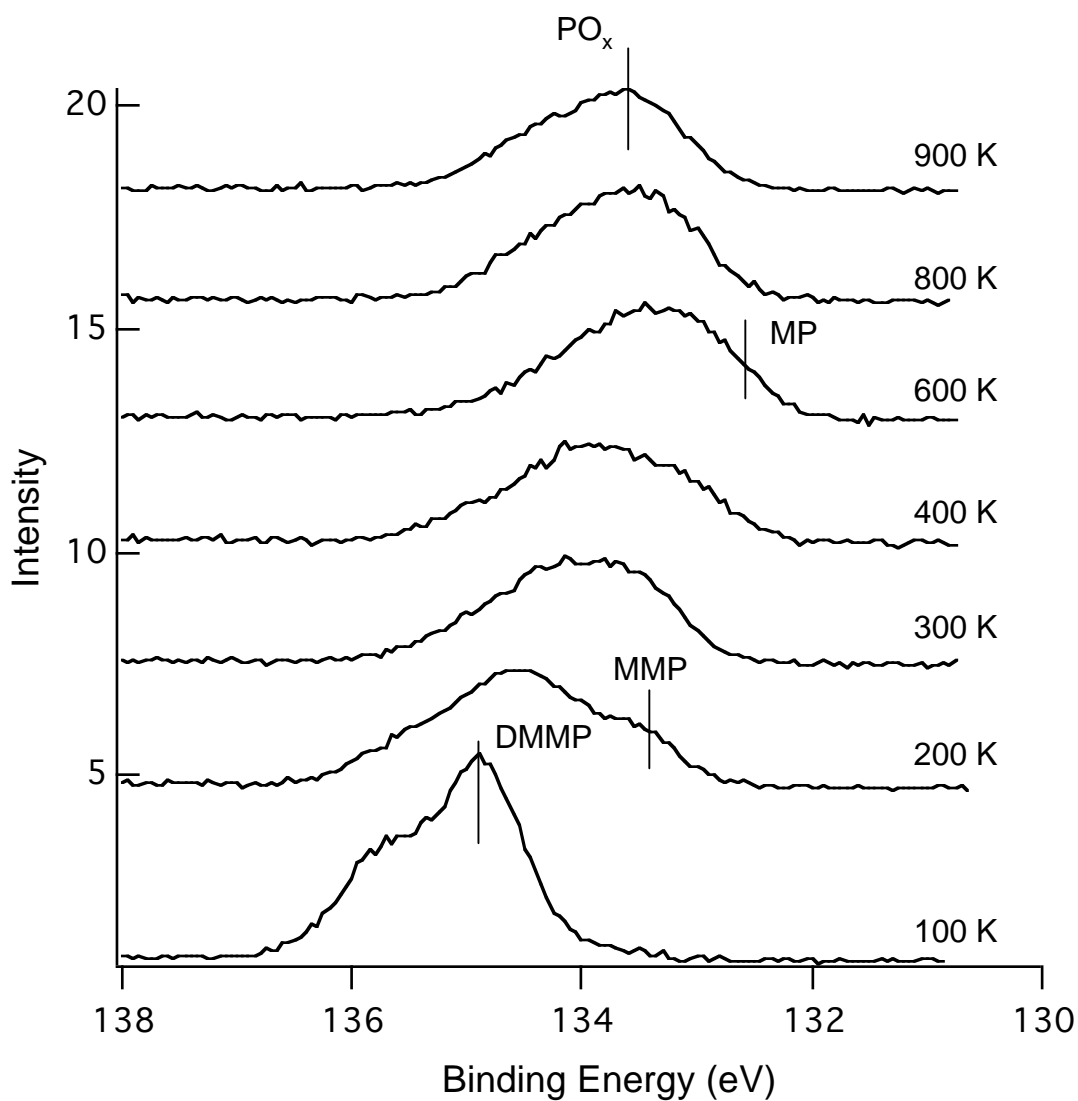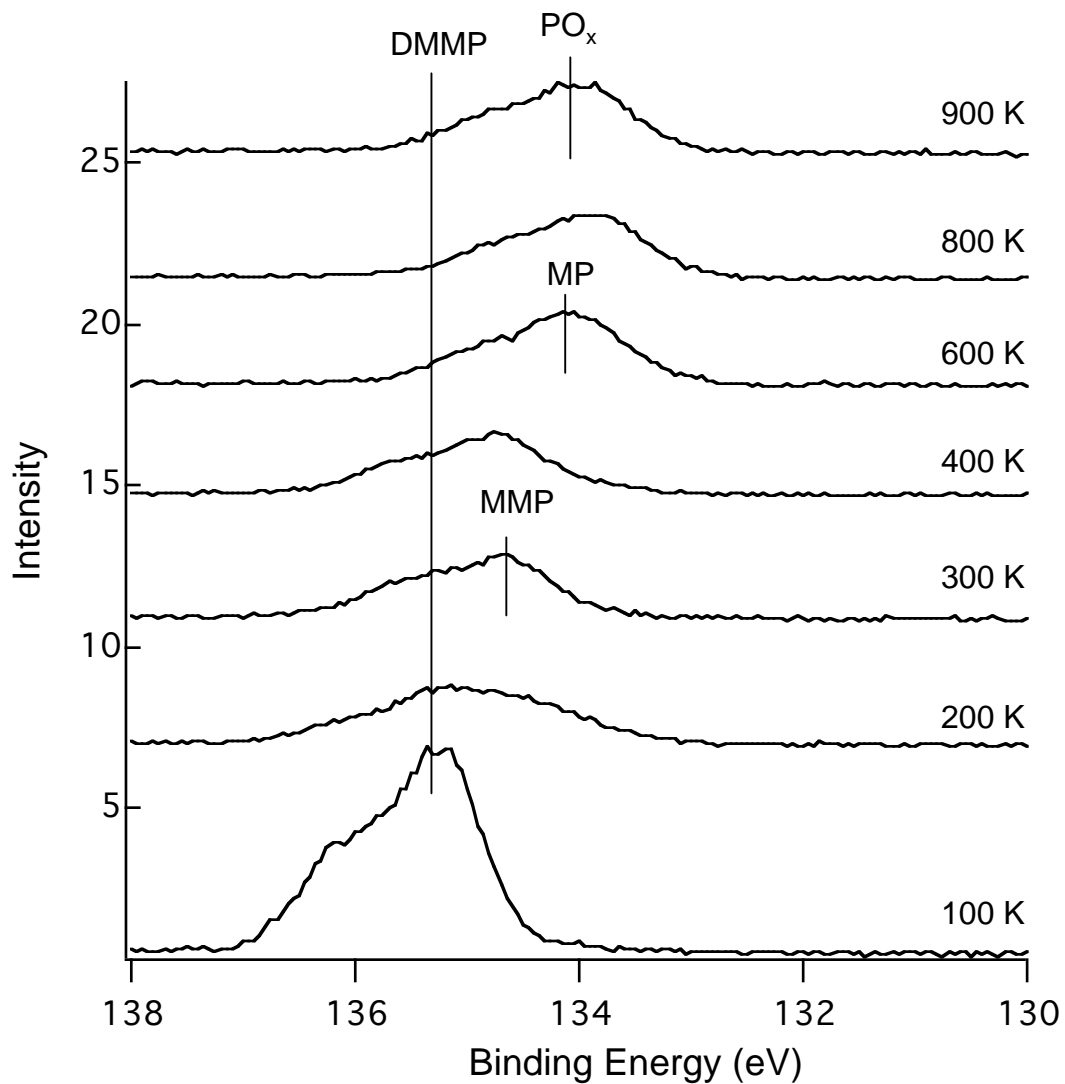
Figure 44: Soft X-ray photoelectron spectroscopy data for the P(2p) region for 10 L of DMMP on stoichiometric ceria at 100 K and then annealed as indicated. Spectra were collected with a 340 eV beam energy.

Figure 45: Soft X-ray photoelectron spectroscopy data for the C(1s) region for 10 L of DMMP on reduced ceria at 100 K and then annealed as indicated. Spectra were collected with a 400 eV beam energy.

Figure 46: Soft X-ray photoelectron spectroscopy data for the O(1s) region for a 10 L of DMMP on reduced ceria at 100 K and then annealed as indicated. Spectra were collected with a 600 eV beam energy.

Figure 47: Soft X-ray photoelectron spectroscopy data for the P(2p) region for 10 L of DMMP on reduced ceria at 100 K and then annealed as indicated. Spectra were collected with a 340 eV beam energy.